STUDY OF CRYOGENIC VAPORIZATION SOURCE-TERM DUE TO HEAT TRANSFER FROM THE SOLID SUBSTRATE

A Dissertation

by

MONIR AHAMMAD

Submitted to the Office of Graduate and Professional Studies of
Texas A&M University
in partial fulfillment of the requirements for the degree of

DOCTOR OF PHILOSOPHY

Chair of Committee,	M. Sam Mannan
Co-chair of Committee,	Luc Véchot
Committee Members,	James Holste
	Eric Petersen
Head of Department,	Nazmul Karim

May 2017

Major Subject: Chemical Engineering

ABSTRACT

U.S. regulation requires LNG facilities to demonstrate a safe exclusion zone for public safety. European safety case also requires that the facility will demonstrate their risk level within a tolerable limit. Thus, cryogenic liquids (*i.e.*, LNG) release scenarios needs to be modeled to determine consequence severity and perceived risk level. The existing models and tools are very sensitive to the inputs, also known as source-terms. Inaccurate inputs might result in an amplified or subdued consequence severity and may change the estimated risk level and/or safety exclusion zone. Accurate prediction of the source-terms is complex due to the presence of boiling regimes and requires validated models of boiling regimes.

A CFD-based approach is taken to model film boiling using Rayleigh-Taylor instability and volume of fluid (VOF) methods. Film boiling simulations for LN_2, LO_2, and LNG are conducted with a various degree of wall superheat. The simulated results were compared with Berenson and Klimenko correlations to demonstrate that CFD model overcomes the limitations of these correlations. To extend the applicability of these simulations, a first principle model is proposed to enable a faster calculation of heat transfer to cryogenic pool boiling.

Medium-scale cryogenic spill experiments have been conducted on an instrumented concrete substrate where LN_2, LO_2, and liquid air are used. The vaporization rate, temperature, and heat flux profiles are recorded during the

experiments. It is found that the effect of the mixture on the LN_2 vaporization rate is not significant and the heat conduction inside the concrete substrate is unidirectional.

The proposed CFD-based film boiling models for LN_2 and LO_2 are validated using medium-scale experimental data and are in agreement for higher wall superheats but slightly deviates for the lower wall superheats. The deviation in experimental data can be attributed to the surface roughness and change in boiling regime from film to nucleate. The model for LNG is validated against the experimental data reported in the literature. It is found that the model can capture the vaporization rate reported from the Maplin Sands experiments and other laboratory tests on film boiling.

DEDICATION

This work is dedicated to my sister Hasina Akhter Kochi. Without her vision, her sacrifice, her trust, her love and affection, I would never have been able to have come this far.

ACKNOWLEDGEMENTS

I would like to express my sincere gratitude to my advisor Dr. Sam Mannan. I have never thought that simple farewell words of him will make a huge impact in my life. During our first meeting at Dhaka, Bangladesh he bade farewell by saying “see you in Texas”. That turned into my PhD study at Mary Kay O’Connor Process Safety Center. I could never thank him enough by writing acknowledgements on how much I have learnt during my stay here, how better person I am than I used to be, how much advanced I am compared to my classmates. It would never happen if he did not give me this amazing opportunity. He has believed in me more than I believed in myself. His “leading by example” way of inspiring has greatly influenced me. I always wanted to have a little more chat with him so that I can listen to more amazing anecdotes that he uses to explain difficult concepts. He has been my guardian, my teacher, my educator and my idol for last five years and will remain so in the upcoming many more years.

I would like to acknowledge Dr. Luc Véchot, my co-advisor and Dr. Tomasz Olewski, my team leader from Texas A&M University at Qatar. They have played a very instrumental role during this period to motivate me, shedding lights at the end of the tunnel, participating in interesting conversation and pushing me towards the goal. Without their constant support and follow up, this research may not mature as it is now. I am truly grateful to them. I would also like to thank my team leaders Dr. Samina Rahmani, Dr. Delphine Laboureur, and Dr. Yi Liu for their help and guidance during the early stage of my research.

I would like to acknowledge Dr. Naz Karim for his personal interest in my research and engaging in lobby conversations despite his busy schedule. I have learnt a lot about US cultures, history, food and places from his vast experiences.

I would like to thank my committee members, Dr. James Holste, and Dr. Eric Petersen, for their guidance and support throughout the course of this research.

Sincere thanks to my friends and colleagues especially Dr. Alim Dewan, Dr. Easir Arafat Khan, Dr. Faruque Hasan, Shubharthi Barua, Syed Al Imran Quraishy and faculty and staff at the Mary Kay O'Connor Process Safety Center especially Valerie Green, Alanna Scheinerman, Dr. Noor Al Quddus, Dr. Hans Pasman, Dr. Simon Waldram, Dr. Maria Papadaki, Dr. Ray Mentzer, Donna Startz, Tricia Hasan and Dr. Ha Nguyen for making my time at Texas A&M University a great experience.

I would like to thank Qatar National Priority Research Fund (NPRP 6-425-2-172) from the Qatar National Research Fund (a member of the Qatar Foundation), which provided the financial support to perform this study. This research would not be possible without this support. Also thanks to Qatar Petroleum (QP) for allowing access to their facility to conduct experiments.

Finally, thanks to family, my sisters, my brothers, my nephews, nieces, my parents, and my wife for their patience and love.

CONTRIBUTORS AND FUNDING SOURCES

Contributors

Part 1, faculty committee recognition

This work was supervised by a dissertation committee consisting of (1) Professor M. Sam Mannan (advisor), Regents Professor and T. Michael O'Connor Chair I, Director of Mary Kay O'Connor Process Safety Center, of Artie McFerrin Department of Chemical Engineering, Texas A&M University; (2) Dr. Luc Véchot (co-advisor) of the Department of Chemical Engineering, Texas A&M University at Qatar; (3) Professor James Holste of Artie McFerrin Department of Chemical Engineering, Texas A&M University and (4) Professor Eric Petersen of the Department of Mechanical Engineering, Texas A&M University.

Part 2, student/collaborator contributions

The experiments performed as depicted in Section 4.1 and 4.2 were conducted in Texas A&M University at Qatar under the collaboration with Dr. Luc Véchot (Principle Investigator), Dr. Tomasz Olewski (Research Scientist at Texas A&M at Qatar) and Syed Quraishy (a MS student of Dr. Luc Véchot). The student participated in the experimental phase and analyzed the raw data (section 4.2.4). Qatar Petroleum's (QP) facility was used to conduct the experiments.

All other work conducted for the dissertation was completed by the student independently.

Funding Sources

This work was made possible in part by Qatar National Priority Research Fund under Grant Number NPRP 6-425-2-172. Its contents are solely the responsibility of the authors and do not necessarily represent the official views of the Qatar National Research Fund (a member of the Qatar Foundation).

NOMENCLATURE

ABS	American Bureau of Shipping
AIChE	American Institute of Chemical Engineers
ALOHA	Areal Locations of Hazardous Atmosphere
BLEVE	Boiling Liquid Expanding Vapor Explosion
CCOHS	Canadian Center for Occupational Health and Safety
CERC	Cambridge Environmental Research Consultant
CFD	Computational Fluid Dynamics
CFL	Courant – Frederic- Levy number
CICSAM	Compressive Interface Capturing Scheme for Arbitrary Meshes
CLSVOF	Coupled Level Set and Volume Of Fluid
CSF	Continuum Surface Force
DNV	Det-Norske Veritas
EPA	U.S. Environmental Protection Agency
FERC	Federal Energy Regulatory Commission
FLACS	Flame Acceleration Simulator by GexCon
GASP	Gas Accumulation Over Spreading Pool model
GRI	Gas Research Institute
LFL	Lower Flammability Limit
LN_2	Liquid Nitrogen
LNG	Liquefied Natural Gas

LO_2	Liquid Oxygen
LOPC	Loss Of Primary Containment
LSMS	Liquid Spill Modeling System
MIT	Massachusetts Institute of Technology
MMS	Minerals Management Service
NASA	National Aeronautics and Space Administration
NBP	Normal Boiling Point
NFPA	National Fire Protection Agency (USA)
NIST	National Institute of Standards and Technology
NOAA	U.S. National Oceanic and Atmospheric Administration
NPRP	National Priority Research Project (Qatar)
PHAST	Process Hazard Analysis Software Tool
PISO	Pressure Implicit with Splitting of Operator
PLIC	Piecewise Linear Interface Calculation
PRESTO	PREssure Staggering Option
QP	Qatar Petroleum
QRA	Quantitative Risk Assessment
QUICK	Quadratic Upstream Interpolation for Convective Kinematics
RPT	Rapid Phase Transition
R-T	Rayleigh - Taylor
SLIC	Simple Line Interface Calculation
TWA	Time Weighted Average

TWA	Time Weighted Average
U.S./USA	United States of America
UFL	Upper Flammability Limit
US DOI	United States Department of Interior
VCE	Vapor Cloud Explosion
VOF	Volume Of Fluid

SYMBOLS

σ	Surface tension, N/m
ρ	Density, kg/m^3
g	Acceleration of gravity, 9.81 m/s^2
λ	Wavelength, m
h_{fg}	Heat of vaporization, J/kg
k	Thermal conductivity, W/m.K
μ	Dynamic viscosity, Pa.S
P, p	Pressure, Pa
C_p	Heat capacity, J/kg.K
T	Temperature, K
ΔT	Wall superheat, K
t	Time, s
Δt	Time step, s
L_c	Characteristic length, m

α	Volume fraction; vapor volume fraction
$\bar{h}$	Average local heat transfer co-efficient, W/m^2.K
$\vec{v}$	Fluid velocity vector, m/s
S_{α_q}	Mass source term for qth phase, kg/m^3
$\dot{m}_{qp}$	Mass transfer rate from the qth phase to the pth phase, kg/s
δ	Thickness of the initial vapor film, m
n	Index; number of variables; iteration number; total number of phases
V	Volume of a cell, m^3
$\vec{F}$	Body force, N/m^3
F_{vol}	Surface tension equivalent body force, N/m^3
E	Total enthalpy, J/m^3

DIMENSIONLESS NUMBERS

f_1, f_2, β	Dimensionless number
Nu	Nusselt number
Ar	Archimedes number
Pr	Prandtl number
Re	Reynolds number

SUBSCRIPTS

$_{l}$ or $_{,l}$	liquid phase
$_{v}$ or $_{,v}$	vapor phase
$_{c}$	critical
$_{D;\ d2}$	most dangerous; two dimensional most dangerous
$_{D3}$	three dimensional most dangerous
$_{sat}$	saturated condition
$_{p,\ q}$	p^{th} and q^{th} phase
$_{wall}$	at wall condition
$_{x,\ y}$	in x and y direction
$_{b}$	at boiling point
$_{f}$ or $_{,f}$	dimension index, 1 or 2

SUPERSCRIPTS

^{n} or $^{n+1}$	value at n^{th} or $(n+1)^{th}$ iteration

TABLE OF CONTENTS

Page

ABSTRACT ii

DEDICATION iv

ACKNOWLEDGEMENTS v

CONTRIBUTORS AND FUNDING SOURCES vii

NOMENCLATURE ix

TABLE OF CONTENTS xiv

LIST OF FIGURES xvii

LIST OF TABLES xx

1. INTRODUCTION 1

1.1 Definition of cryogenic liquids and introduction to LNG 1
1.2 Types and overview of cryogenic hazards 2
1.3 Major incidents related to LNG 6
1.4 Release modeling and source-term 9
1.5 Risk and consequence analysis 10
1.6 Is overestimation of source-term a conservative approach? 12
1.7 Conclusions 14

2. VAPORIZATION SOURCE-TERM MODELING: STATE-OF-THE-ART REVIEW 15

2.1 Boiling regimes and vaporization heat flux 16
2.2 Vaporization source-term models 18
2.2.1 Reid and Wang models, 1970 18
2.2.2 Briscoe and Shaw model, 1980 22
2.3 Combined source-term models 23
2.3.1 Raj and Kalelkar, 1974 23
2.3.2 Opschoor, 1977 24
2.3.3 SOURCE5, 1993 24
2.3.4 SPILL 25

2.3.5 GASP 25
2.3.6 SUPERCHEMS 25
2.3.7 SAFESITE3G 26
2.3.8 CANARY 26
2.3.9 PHAST 26
2.3.10 Fay, 2003 27
2.3.11 ALOHA 27
2.3.12 LSM90/LPOOL 27
2.3.13 LSMS 28
2.3.14 ABS Consulting model, 2004 28
2.3.15 LNGMAP 29
2.3.16 SANDIA 29
2.3.17 FLACS 29
2.3.18 Brambilla and Manca, 2009 30
2.3.19 Drivas, 1982 30
2.3.20 Leonnelli et al, 1994 31
2.3.21 CHEMMAP 31
2.4 Heat transfer correlations 31
2.4.1 Zuber heat transfer correlations 32
2.4.2 Berenson heat transfer correlation 33
2.4.3 Klimenko heat transfer correlation 34
2.5 Limitations of the existing heat transfer correlations 35
2.6 Conclusions 36

3. NUMERICAL STUDY OF CRYOGENIC FILM BOILING 37

3.1 Rayleigh-Taylor (R-T) instability approach and perturbation analysis 38
3.2 CFD simulations of film boiling: state-of-the-art review 42
3.3 Film boiling of cryogenic liquids using CFD 43
3.3.1 Mathematical formulations 43
3.3.1.1 Interface tracking using VOF method and calculation of curvature 44
3.3.1.2 Material properties 46
3.3.1.3 Governing equations 47
3.3.1.4 Continuum surface force model 47
3.3.1.5 Discretization 48
3.3.1.6 Discretization of VOF equation 48
3.3.2 Simulation setup 49
3.3.2.1 Grid sensitivity analysis 51
3.3.2.2 Time step sensitivity analysis 53
3.4 Results and discussions 54
3.4.1 LN_2 film boiling 55
3.4.2 LNG film boiling 59
3.4.3 Non – alternating bubble generation 62
3.4.4 LO_2 film boiling 64

3.4.5 Behavior of wall heat flux 66
3.4.6 Effect of wall superheats on bubble generation frequency and bubble diameter 69
3.5 Proposed model to predict film boiling heat transfer 72
3.6 Conclusions 75

4. EXPERIMENTAL VALIDATION OF THE CFD BASED FILM BOILING STUDY 78

4.1 Introduction to the spill experiments: A literature review 79
4.2 Experimental study of vaporization source-term on concrete substrate 80
4.2.1 Schematic diagram of the experimental setup 82
4.2.2 Thermo-physical properties of the concrete substrate 85
4.2.3 Experimental procedure 88
4.2.4 Results and discussions 88
4.2.4.1 Liquid mass vaporization 88
4.2.4.2 Temperature and heat flux profiles inside concrete substrate during LN_2 vaporization 92
4.2.4.3 Temperature and heat flux profiles inside concrete substrate during LO_2 vaporization 95
4.2.4.4 Temperature and heat flux profiles inside concrete substrate during mixture vaporization 98
4.2.4.5 Effect of mixture properties on the vaporization of cryogenic liquids 101
4.2.5 Concluding remarks on the medium-scale experiments 102
4.3 Validation of CFD-based LN_2 film boiling model 104
4.4 Validation of CFD-based LNG film boiling model 108
4.5 Validation of CFD-based LO_2 film boiling model 109
4.6 Conclusions 110

5 CONCLUSIONS AND FUTURE RESEARCH 112

5.1 Conclusions 112
5.2 Future research 114

REFERENCES 116

LIST OF FIGURES

Page

Figure 1: Different aspects of release modeling during a loss of primary containment (LOPC) 10

Figure 2: Generic hazard scenario sequence in a LNG facility 11

Figure 3: Is overestimation of source-term always a safer approach? 13

Figure 4: Cryogenic spill phenomena and associated boiling regimes. 17

Figure 5: Rayleigh-Taylor (R-T) instability for liquid phase overlaying on vapor phase. Adapted from [69] 39

Figure 6: (a) Actual vapor-liquid-interface (b) Interface reconstructed using PLIC (c) Interface using donor-acceptor scheme. 46

Figure 7: R-T instability approach for film boiling simulation using CFD 50

Figure 8: Setup of 2D film boiling simulations 50

Figure 9: Grid sensitivity with respect to bubble growth during film boiling of LNG 52

Figure 10: Time convergence study showing the bubble interface at 0.67 second using 64x192 meshes for different time steps. 53

Figure 11: Time step sensitivity of the wall heat flux for liquid oxygen film boiling 54

Figure 12: Evolution of bubbles during LN_2 film boiling at wall superheat of 32 K 56

Figure 13: Simulated wall heat flux for film boiling of LN_2 at $\Delta T = 32\ K$ 57

Figure 14: Velocity vectors for LN_2 a wall superheat of 73 K. (a) Before bubble release (b) After bubble release 57

Figure 15: Temperature distribution during the film boiling for LN_2 at 73K wall superheat and solution time at 0.25 second. 59

Figure 16: Streamlines showing the vortex formations for LNG at a wall superheat of $\Delta T = 43K$. 60

Figure 17: Surface heat flux for the film boiling of LNG at $\Delta T = 43$ K. 62

Figure 18: Effect of wall superheat on bubble generation frequency during LN_2 film boiling 64

Figure 19: Wall heat flux for liquid oxygen at $\Delta T = 32K$ 65

Figure 20: Simulated wall heat fluxes of liquid oxygen film boiling 66

Figure 21: Trend of wall heat flux for LN_2 film boiling at $\Delta T = 103K$. 68

Figure 22: Surface heat flux for the film boiling of LNG at $\Delta T = 83$ K. 68

Figure 23: FFT of heat flux variation for LNG at a wall superheat of $\Delta T = 43$ K. 70

Figure 24: Bubble generation frequency of simulated film boiling cases at various wall superheats 71

Figure 25: Bubble diameters of the simulated film boiling cases at various wall superheats 72

Figure 26: CFD-based model to predict heat flux of (a) LN_2 and (b) LNG (c) LO_2 film boiling 75

Figure 27: Schematic diagram of the experimental setup. Black dots represent the location of thermocouples inside concrete substrates and heat flux sensors location was indicated by the red dots. 83

Figure 28: Experimental set-up. (a) Cryogenic liquid tank (b) Vapor – liquid separator (c) Heat flux sensor (d) insulated set-up (e) insulation thickness and level measuring thermocouples bar 85

Figure 29: Thermal conductivity of the concrete as function of mean temperature 86

Figure 30: Specific heat capacity of powdered concrete samples using DSC 87

Figure 31: Mass of the liquid pool 90

Figure 32: Mass vaporization rate of cryogenic liquids after a spill on a concrete surface 90

Figure 33: Temperature profile inside the concrete slab during the spill of liquid nitrogen 93

Figure 34: Heat flux to the liquid nitrogen pool 95

Figure 35: Temperature profile inside concrete slab during the spill of liquid oxygen. 96

Figure 36: Conductive heat flux provided to liquid oxygen pool 97

Figure 37: Temperature profile inside concrete slab during the spill of liquid nitrogen (80%) and liquid oxygen (20%) mixture. 99

Figure 38: Heat flux inside the concrete at the depth of 28.5 mm and 96.5 mm. 100

Figure 39: Effect of mixture on the temperature profiles in layer 1 and layer 2.....101

Figure 40: Effect of mixture on the heat flux profiles in layer 1 during the early and the later stage of the spill 102

Figure 41: Simulated wall heat flux compared with the thermocouple at 24 mm depth (TC-111). 105

Figure 42: Validation of heat flux using estimated wall superheat for LN_2 film boiling106

Figure 43: Comparison of temperature profiles predictions 107

Figure 44: Validation of CFD based LNG film boiling model 109

Figure 45: Simulated wall heat flux compared against the estimated wall superheat....110

LIST OF TABLES

Page

Table 1: LNG marine transport incidents [10] 7

Table 2: Incidents in LNG facilities[10] 8

Table 3: LNG spill experiments and its key aspects 81

Table 4: Coordinates of the thermocouple and heat flux sensors' locations inside the concrete substrate 84

1. INTRODUCTION

Due to the technological break-through of shale gas exploration, liquefied natural gas (LNG) industries in the USA and other countries with natural gas reserves are booming [1]. Once an importing country, USA is turning to be an LNG exporting nation. As a result, LNG manufacturing activities related to liquefaction, storage, transportation and re-gasification have increased. Experts [2] and government agencies [3] emphasized the need for better risk assessment procedures associated with these operations. Standards such as NFPA 59A [4], therefore, recommends accurate estimation of LNG spill consequence. The objective of this study is to identify and fill the gaps that exist in the current practice and literatures while addressing an accurate risk assessment of LNG related activities. LNG being a cryogenic liquid, application of this study is broadened by considering other cryogens, *e.g.,* liquid nitrogen and liquid oxygen.

1.1 Definition of cryogenic liquids and introduction to LNG

The definition of a cryogenic liquid or cryogen is not well defined in the literature or in practice. Different institutions have adopted different temperature scale to distinguish a cryogenic liquid. Air Products, a cryogenic liquid manufacturer defines as "a liquid with a normal boiling point (NBP) below -90ºC" [5]. NASA scientists assumed that a cryogenic liquid has NBP below -150ºC [6]. The U.S. National Institute of Standards and Technology (NIST) generally choose a temperature approximately below -150ºC to define cryogenics [7]. Regulatory organizations such as Canadian Center for

Occupational Health and Safety (CCOHS) adopts the definition of NIST of temperature scale [8]. Despite different definitions of cryogenic liquid, flexibility exists while addressing the properties and hazards of these materials. For example, carbon-di-oxide and nitrous-oxide which has a slightly higher NBP than -150ºC, often considered as a cryogenic liquid.

A general definition of cryogenics is that it is a gas at normal temperature and pressures; however, very low temperatures are required to bring them to their liquid state. In their liquid state its volume shrinks significantly (order of 500 - 2000) providing advantage of transporting huge amount in a small shipment.

1.2 Types and overview of cryogenic hazards

Each cryogen has its own specific properties however it can be grouped into the following three broad categories:

- Inert Gases: An inert gas does not chemically react or help in combustion process. However it can asphyxiate by reducing the concentration of oxygen when disperse. Examples are nitrogen, helium, argon, krypton etc.
- Flammable Gases: A cryogenic liquid which burns in the presence of oxygen at their gaseous state are hydrogen, methane, ethane, liquefied natural gas (LNG) etc.
- Oxygen: It is the essential component for many combustion or oxidation reactions. A lot of materials are considered non-combustible; however,

burns in the presence of liquid oxygen. For example, organic materials react violently in presence of liquid oxygen.

In this study representative material from each category, *i.e.*, liquid nitrogen (LN_2), LNG and liquid oxygen (LO_2) are primarily studied to understand the effect of different types of cryogenic material on the vaporization source-term estimations. The motivation and background of this study will be further extended in the next sections.

Cryogenic liquids can pose many hazards to the personnel, property loss and environmental damage during many stages of operations such as liquefaction processing, storage, transportation, re-gasification. An accidental release of cryogens may pose health and fire/explosion hazards. Among the studied cryogens LNG poses the most significant amount of hazards. An overview of the associated hazards are as follows:

- Extreme cold hazard/Freeze burn: Due to the extreme cold temperatures of cryogenic liquids and their associated vapors it can cause frostbite to the contacted skin. Unprotected skin in contact with metal cooled by cryogenic liquids can stick to the metal surface and can tear when pulled away. Even non-metallic surface is dangerous when cooled by cryogenic liquids. Breathing of extremely cold air may cause damage to the lungs. Such incident of freeze burn happened in 1977, in Arzew, Algeria during a ship-loading operation of LNG resulting from a valve rupture [9].
- Asphyxiation hazard: Cryogenic vapors are usually heavier than air. Therefore during a loss of primary containment (LOPC) event, this cold, heavy gas accumulates near the ground and can reduce the oxygen

concentration lower than normal. Oxygen deficiency is very serious in an enclosed or confined space as small quantity can expand to large volume due to evaporation. For a short duration exposure of a concentration of oxygen below 15% impairs normal behavior, below 10% causes nausea and vomiting, and 6% oxygen causes death [10].

- Toxic hazards: Toxic hazards are specific to the components that are presents in the cryogenic liquid. A high concentration of oxygen has a toxic health effect whereas in the LNG processing plant, there are streams which may have significant amount toxic component such as H_2S and toxic refrigerants.
- Fire hazards: The major threats of LNG facilities are fire. The major types of fire that may occur are pool fire, flash fire and jet fire.

  Flash fire: A dispersing vapor cloud from a LNG pool, if reaches an ignition source, a flash fire would result. A flash fire is a transient short fire, which runs towards the source of fuel. It burns the premixed vapor cloud between lower flammability limit (LFL) and upper flammability limit (UFL) at a faster rate. Therefore, it runs along the edge of the cloud at a faster rate and ends at the pool causing a pool fire. A flash fire can be fatal to people when engulfed in the fire however its radiation level is lower than the pool fire and jet fire.

  Pool fire: After a flash fire run back to the pool of LNG and results in Pool fire. A pool fire can also result from direct ignition of

vapor formed over the pool. LNG pool fires are very bright as its flame is sootless. Large-scale pool fires may form soot because of the oxygen deficiency in the center.

Jet Fire: An LNG jet fire is possible in the processing area only where it is at pressurized processing conditions. LNG storage tanks use refrigeration system at atmospheric condition therefore a conventional jet fire is not possible but jet fire may occur due to hydrostatic pressure difference in the tank.

- Vapor cloud explosions (VCE): A VCE results due to ignition of dispersed cloud in a congested zone. Its occurrence depends on the material reactivity, congestion level. Since the main constituent of LNG is methane which has low material reactivity, many researchers does not believe that LNG may cause an outdoor vapor cloud explosions. It is particularly said that a detonation explosion is not possible but a deflagration explosion is a low probability event. However, experiments confirmed that under partial confinement or (/and) congested regions a VCE can occur [10]. In the LNG processing area, a congested region is common due to the high density of obstacles such as piping, pumps, vessels etc. An LNG VCE in an enclosed environment can occur during the indoor spills, *e.g.*, in a building from gas lines.
- Rapid Phase Transitions (RPT): A RPT is a physical explosion due to sudden boiling of cryogenic liquids when spilled into water causing a

pressure wave [11]. The overpressures resulting from RPT are not high enough to cause personnel injury however equipment has been damaged in the past due to RPT.

- Rollover: LNG is a multicomponent mixture which continuously vaporizes by absorbing heat from the surface of the insulated tank. Therefore, in LNG tanks, there can be stratified density layers at different depths. Preferential boiling at the top, a heavier layer forms, and the lighter layer from the bottom rises up due to hydrostatic pressure difference and flashes immediately. This small amount of flash may cause expansion of 600 times and can pressurize the storage tanks. This can also cause flammable material to vent and may result in fire.

Natural gas is one of the fastest growing sources of energy which is considered as a clean burning fuel. Its production has been increasing in many countries such as USA, Qatar, Russia, Austria, Malaysia etc. Purified and refrigerated natural gas, by using liquefaction technology, is compressed to 620 times of its vapor volume, to a liquid phase and is known as LNG.

1.3 Major incidents related to LNG

LNG industry has a better safety record if compared to refineries and petrochemical plants. However, in a report by Oil and Gas Producers (OGP), of the top worldwide onshore incidents causing most damage from 1970-2005, two LNG incidents Staten Island and Skikda have made its way to the list [12]. Table 1 and Table 2 list

notable LNG marine transport and onshore incidents. Planas-Cuchi *et al.* [13] also described a boiling liquid expanding vapor explosion (BLEVE) of a LNG truck carrier in Catalonia, Spain on June 22, 2002. This incident resulted in fire and explosion, which caused 2 fatalities and the tank fragments were found 200m away from the incident site. Currently there are 23 liquefactions, 58 regasifications and 224 LNG ships exists worldwide which carries more than 168 million metric tons of LNG across the ocean [14]. Therefore, the potential to cause similar incidents is significant but it should also be noted that the LNG technologies has improved significantly as well. In order to prevent and/or mitigate the consequences of similar catastrophic events, it is very important to understand or to be able to model the processes leading to such incidents. LNG source-term model is the main input parameter that is needed to model events such as dispersion, fires, and VCE.

Table 1: LNG marine transport incidents [10]

Year	Description
1974	A 3 ft gash in the outer hull of Methane Princess carrier at Canvey Island Terminal
1983	The cargo transfer arm sheared of 87,600 m^3 Norman Lady carrier and spilled LNG
1989	Sheared cargo transfer arm from the 40,000 m^3 Tellier at Skikda, Algeria caused LNG spill
1997	Damage in the hull of Capricorn LNG carrier when it struck a mooring dolphin near Japan
1999	Damage of the Methane Polar carrier due to engine failure leading to a collision with the pier at Trinidad and Tobago
2002	The Norman Lady collided with US nuclear submarine the USS Oklahoma City, and suffered from leakage of seawater into the dry tanks

Table 2: Incidents in LNG facilities[10]

Year	Description
1944	In Cleveland, Ohio, USA, a newly built tank failed catastrophically due to thermal embrittlement and spilled LNG into the municipal sewer system. The LNG vaporized and found ignition source resulting in fire and explosion which killed more than 124 people and injured more than 200.
1973	In Staten Island, New York, USA, during a tank repair, a non-explosion proof irons and vacuums were used in sealing the liner. During the time of repair, gas was trapped behind the membrane which exploded. Enough pressure were raised inside the tank which caused a 6 in thick concrete roof dome to fall on 37 workers and killed them instantly. Though this accident is not directly related to LNG, it has made it to biggest 28 losses as mentioned before.
1979	At the Cove Point import terminal, LNG leaked through the pump seal and caused a vapor cloud inside the building. When a worker switched on a circuit breaker, it ignited the vapor causing an explosion and killed the worker. It also resulted in $3million economic losses [9].
1985	At a peak shaving facility in Pinson, AL, USA, a welded patch plate failed causing LNG release from the liquefaction train. Six people were injured.
1987	During the Falcon series test # 5, in Mercury, NV, USA, after a sequence of strong RPT, a VCE occurred which lasted for 30 seconds.
1989	LNG entered into the pump through open drain valves causing a high pressure jet. The vapor cloud ignited after 30 seconds causing a flash fire which eventually became a jet fire and burned face and hands of two operators.
2004	A refrigerant line leaked and vapors entered into the high pressure steam boiling in Skikda, Algeria, at the Sonatrach LNG liquefaction plant. The boiler exploded resulting in damages to other facility which also resulted in additional fire and explosion. As a result 27 workers were died, 80 injured and LNG train was completely destroyed.

Table 1 and Table 2 show that the number of LNG spill is significant. Therefore, LNG release modeling is a crucial step in risk/consequence analysis of LNG related activity.

1.4 Release modeling and source-term

Following an accidental release as shown in Figure 1, cryogenic liquids undergo many stages of physical processes before it forms a vapor cloud mixed with air to cause fire, explosion etc. For example, LNG is stored at 111K at atmospheric pressure. During loss of primary containment event, LNG will flow onto the ground and form a liquid pool. A small proportion of the cryogenic liquids will vaporize immediately by absorbing heat from the surrounding hot air before the large portion touches the ground. However, the most significant amount of the vapor will result due to the heat transfer from the substrate, *i.e.*, ground or water (if spilled on water). While absorbing heat from the substrate the pool will also spread due to the hydrodynamic potential difference. The LNG vapor is usually heavier than air and stays closer to the ground at the beginning. However as it is heated, it becomes lighter and disperses faster. Time and location of ignition source will determine the consequence of this accidental spill scenario, *e.g.*, fire, explosion etc. But without the understanding of how much vapor is going to be dispersed, it is impossible to determine the consequence of this incident. This important parameter (vaporization rate) is crucial and considered as an input to model further physical processes such as the dispersion cloud volume, oxygen concentration of the dispersed area, pool fire, jet fire, VCE consequences *etc*. As this parameter is critical to consequence estimation and used as an input to those models, it is often referred to as "source-term". Without an accurate estimation of this key parameter, the consequence analysis of a potential incident scenario would be inaccurate.

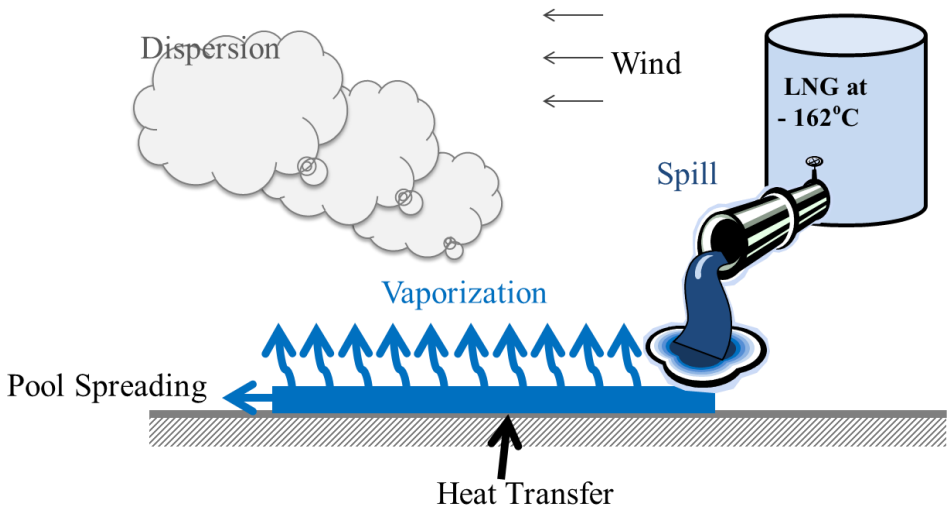

Figure 1: Different aspects of release modeling during a loss of primary containment (LOPC)

1.5 Risk and consequence analysis

$$\text{Risk} = \text{Frequency} \times \text{Consequence}$$

In a LNG facility, risk needs to be managed lower than predetermined acceptable criteria which usually resemble the societal tolerability. Risk of an LNG facility is defined as the consequences that may occur and frequency of its occurrence. Thus modeling of release scenario is an integral part of the risk assessment.

Figure 2 depicts the hazards of a LNG facility. Upon the release of LNG, the consequence can take different paths depending on the presence or not of ignition source. If there is no immediate ignition source, it might be limited to, cryogenic asphyxiation and toxic hazards. Example cases of cryogenic hazards could be a spray of cryogenic liquid to an operator due to breakage of transfer line, full bore pipeline

rupture, or, touching of surfaces which contains cryogenic liquid. Raw material of LNG is natural gas, which may contain toxic substances such as H_2S, and the process may need toxic refrigerant to liquefy natural gas. Accidental release of those streams may have a toxic hazard in the processing plant.

In case of an immediate ignition, a fire scenario would occur. Leakage from pressurized process conditions may lead to a jet fire whereas leakage from atmospheric condition would result in a pool fire. Both kinds of fire may further lead to a secondary boiling liquid expanding vapor explosion (BLEVE) scenario resulting from the direct or radiative heating of a nearby storage tank.

In absence of immediate ignition sources, as shown in Figure 2, low consequence scenario such as flash fire can occur and more severe scenarios such as VCE occurs due to delayed ignition of the vapor cloud.

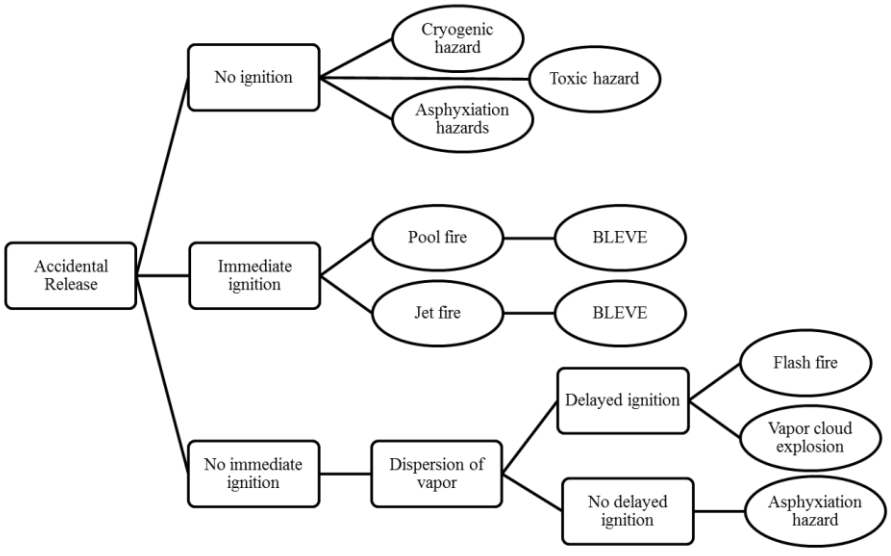

Figure 2: Generic hazard scenario sequence in a LNG facility

Based on the above discussion, regardless of the consequences of the release scenario, without accurate estimation of vaporization rate, it is impossible to accurately predict the consequences of a fire, explosion, or vapor cloud dispersions. In other words, the accuracy of risk assessment depends on the accurate estimation of vaporization source-term. Thus, this study addresses an important key factor, *i.e.*, an accurate estimation of vaporization source-term, to enable a more reliable risk assessment of cryogenic facilities.

1.6 Is overestimation of source-term a conservative approach?

In process safety context, a conservative approach means a "worst-case" scenario of the loss of primary containment event. A common mistake of analyzing a "conservative" safety case is done by over estimating the vaporization source-term. However, this may not lead to a true representation of a conservative approach. Figure 3 elucidates this concept by considering different scenarios. In Figure 3(a), a release source, for example, a breakage of pipeline carrying flammable liquid is shown as the red star. The location of potential ignition source is shown by the red thunder symbol. At a lower vaporization rate, the cloud disperses in the congested areas of the facility. Figure 3(b) depicts a scenario where the explosive cloud mixture, *i.e.*, mixture within the concentration between LFL and UFL, predominantly stays within the congested area. On the other hand, at a higher vaporization rate, the cloud within the congestion area is too rich in fuel concentration and therefore too rich to form a VCE as shown in Figure 3(c).

One may argue that the concentration will come down to an explosive mixture eventually; however, it may give enough time to evacuate. Therefore, for this particular case, the consequence of a low vaporization rate is more conservative than a higher estimation. However, it may not be always correct. Source-term overestimation may lead to another problem *i.e.*, underestimation of pool area as the liquid will vaporize faster before reaching the actual distance. As a result the overall vaporization might be an underestimation. Thus, in order to make an informed decision making for planning, risk assessment, it is crucial that the source-term estimation is accurate. Trying to avoid an accurate estimation by delving into over or under estimation may lead to a wrong prediction of the risk.

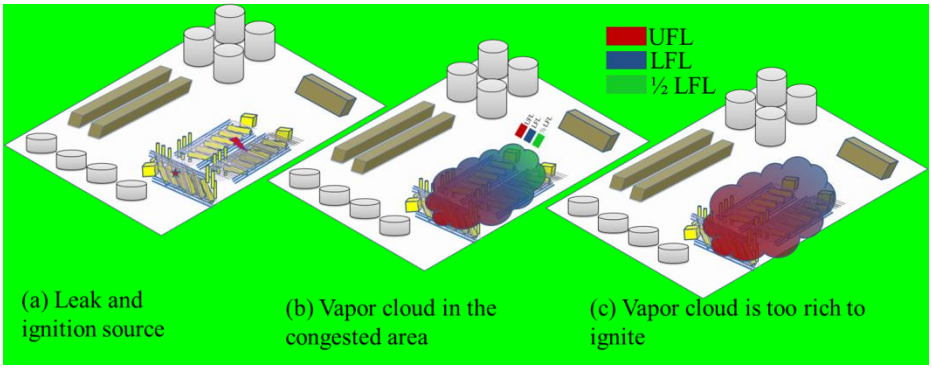

Figure 3: Is overestimation of source-term always a safer approach?

1.7 Conclusions

Due to the economic advantage of LNG transportation, LNG-related activity has increased an order of magnitude in this decade. An accurate risk assessment of LNG facility, storage tank, shipping *etc.*, has become necessary in order to ensure the safety of people, prevent the economic losses and preserve the environment. Vaporization source-term is the key parameter to accurately predict consequence severity of a LOPC event. Over and under estimation of cryogenic vaporization rate is not a conservative approach and may lead to inaccurate estimation of safety exclusion distance.

2. VAPORIZATION SOURCE-TERM MODELING: STATE-OF-THE-ART REVIEW

Vapor cloud dispersion study is highly sensitive and dependent on the vapor generation rate calculated from the source-term models [15]. Therefore, results of the source-term models will significantly influence important safety measures such as safe exclusion zones, consequence severity and risk level.

In a report (March, 2007) by U.S. Government Accountability Office (GAO), a panel of 19 experts in the field of LNG safety has identified the lack of source-term modeling and the resulting uncertainties incurred in the consequence analysis. [16]. The report emphasized the priority of making progress in the source-term modeling, such as pool spreading, boil-off due to heat transfer, as a transient process.

Another recent report by UK HSE also underlined the need for developing critical models to study LNG spills. It states "*there has been far less research carried out in developing and testing models for the source of LNG spills"*[17].

Unfortunately, accurate estimation of vapor formation rate is complex due to the occurrence of many phenomena such as jet flow, flashing, mist formation, pool formation and spreading, boiling and evaporation. Vaporization due to pool boiling is in the core of these models. Thus, this study is focused on a detailed analysis of vapor formation rate.

2.1 Boiling regimes and vaporization heat flux

The sources of heat onto a land cryogenic pool are conductive heat from the ground, convective heat from the atmosphere and solar radiation or radiative heat from the fire. Among the different heat sources, conductive heat contributes the most to vapor formation during the early stage of the spill [18]. TNO yellow book also states that in the initial stage of spill on ground, heat conduction from the subsoil is the prevailing heat source of vapor formation [19], however may not be the case for later conditions [18].

Owing to the conductive heat, cryogenic liquid undergoes three different boiling regimes; film boiling at the beginning, nucleate boiling towards the end of the spill and transition between these two. A pictorial depiction of boiling phenomena, owing to the conductive heat transfer from the substrate, is presented in Figure 4. A large temperature gradient during the early stage of the spill (189 K for LNG assuming ground at 300 K), result in a persistent vapor film between the substrate and the boiling liquid, and is known as film boiling. As shown in the schematic under curve AB, generated bubbles completely cover the substrate surface forming a continuous film between the liquid and solid, which restrict the heat flux. With time, the surface temperature falls, reaching a lowest heat transfer rate (Leidenfrost point) as shown by point B in Figure 4. Further decrease in temperature gradient cannot sustain a continuous film, the film breaks off, and boiling liquid comes in contact with the heated substrate, which is known as transition boiling regime. The behavior of heat flux as a function of wall superheat and schematic diagram of transition boiling are presented by the curve BC and corresponding area below, as shown in Figure 4. With the contraction of intermittent

vapor film, more and more liquid participates in convective heat transfer from the heated surface, causing an increase in heat flux as a function of decreasing wall superheat. The duration of boiling in this regime is very short compared to film boiling and nucleate boiling (CD). As a result, the cumulative amount of vapor generation in transition boiling regime is quite small compared to other boiling regimes. With the further decrease of wall superheats, in the nucleate boiling regime, bubbles become isolated from each other and detach from the nucleation sites of the substrate. Geometric properties of the substrate, such as surface roughness play a major role in estimating vapor generation due to nucleate boiling. Point D in Figure 4 represents the onset of nucleate boiling (ONB), below which the heat transferred to the pool contributes in free convection.

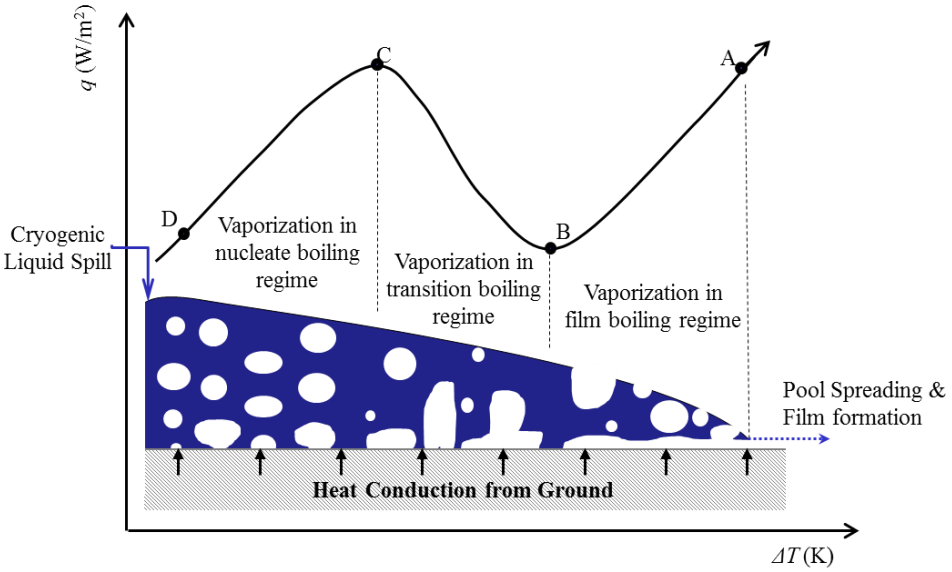

Figure 4: Cryogenic spill phenomena and associated boiling regimes.

2.2 Vaporization source-term models

All existing source-term models are one-dimensional and assumes that the width of substrate is large enough to consider that heat is conducting vertically to the liquid pool as shown in Figure 4. It also assumes that the depth of the substrate is large enough to consider a constant temperature inside the substrate after certain depth. In general, these assumptions hold valid for spill on ground. However, it may not be accurate for spill on water and thin substrate.

2.2.1 Reid and Wang models, 1970

Understanding the importance of vaporization "source-term" in determining the severity of loss of primary containment, Reid and Wang [21] have studied this parameter both experimentally and theoretically for LNG on insulated dike floors.

An ideal heat conduction model of a semi-infinite flat plate is given by

$$\alpha \frac{\partial T}{\partial x^2} = \frac{\partial T}{\partial t} \tag{1}$$

where T is the substrate temperature at any time t, x is distance below the surface into the substrate material and α is the thermal diffusivity given by $\alpha = \frac{k}{\rho C}$.

Four different mathematical solutions of this model are presented by Reid and Wang [21] based on the assumed boundary conditions. However, as only two of the four models are mostly practiced because it is shown with the experimental results that these two models can capture sufficient accuracy. All four models are described below.

Model 1: Based on the assumption that the solid substrate has an infinite depth and the value of boiling heat transfer co-efficient is infinite, *i.e.*, the temperature of solid at the liquid-solid contact is equal to the boiling point, the solution of Equation (1) is shown below:

$$\frac{T - T_b}{T_i - T_b} = \text{erf}\, X \tag{2}$$

where $X = \frac{x}{2}\sqrt{\alpha t}$, T_b is the boiling point, and corresponding heat flux at the surface is given by Equation (3)-

$$q = \sqrt{\frac{k\,\rho C}{\pi}}(T_i - T_b) \cdot t^{-1/2} \tag{3}$$

Since $q = \left(\frac{\dot{m}}{A}\right)\Delta H_v$, substituting in Equation (3) gives,

$$\frac{\dot{m}}{A} = (k\rho C/\pi)^{1/2} \cdot \left(\frac{T_i - T_b}{\Delta H_v}\right) \cdot t^{-\frac{1}{2}} \tag{4}$$

Again considering, $F = (k\rho C/\pi)^{1/2} \cdot \left(\frac{T_i - T_b}{\Delta H_v}\right)$ results in Equation (5). Similar formulations has also shown by TNO yellow book [22].

$$\frac{\dot{m}}{A} = \text{F} \cdot t^{-\frac{1}{2}} \tag{5}$$

Equation (5) is the general 1-D heat transfer model that is widely used to estimate the cryogenic vaporization source. Commonly, the value of F is determined experimentally. For example, based on experimental investigation, for insulated concretes, Reid and Wang predicted the value of F as 0.047 $kgm^{-2}s^{-1/2}$ (Dycon K-23), and 0.065 $kgm^{-2}s^{-1/2}$ (Dycon K-35). They also provided the constant for soil, polyurethanes, and corrugated aluminum [21].

It is obvious from the above formulations that this model does not consider the heat transfer resistance in the liquid phase. Therefore, it does not take into account the phase change and its effect in the vaporization source-term estimations. Thus, the predicted source-term is an overestimation of the actual vapor formation rate.

Model 2: Based on the assumption of an infinitely deep substrate conducting heat to the cryogenic pool of liquid and a finite boiling co-efficient in the solid-liquid interface, Equation (1) can be solved as shown in Equation (6).

$$\frac{T - T_b}{T_i - T_b} = \text{erf}\, X + \frac{e^{-X^2}}{Z\sqrt{\pi}}\, E(Z) \tag{6}$$

Where

$$E(Z) = \sqrt{\pi} Z\, e^{Z^2} erfc\, Z$$

$$Z = X + Y; \qquad Y = h\sqrt{(\alpha t/k)}$$

and heat flux at the surface is given by Equation (7),

$$q = \frac{k(T_i - T_b)}{\sqrt{\pi \alpha t}} E(Y) \tag{7}$$

Model 2 can also be expressed in the general form of Equation (5); however, it has overcome the major limitation of not considering heat transfer resistance at the liquid-solid interface. However, this model is subject to the heat transfer correlation this would be used to estimate the heat transfer coefficient h.

Model 3: Based on the assumption that the substrate has a finite depth and the temperature of the solid-liquid interface is the boiling point of the liquid, *i.e.*, infinite boiling heat transfer co-efficient, model 3 is developed.

Let's assume, the thickness of the substrate, $x = \delta$

At $x = \delta$, the heat flux $q = 0$ meaning $x = \delta$ is an adiabatic plane.

The solution of Equation (1) is

$$\frac{T - T_b}{T_i - T_b} = \frac{4}{\pi}\sum_{n=1,3,5,\ldots}^{\infty} \frac{1}{n} \cdot \sin\left(\frac{n\pi}{2} \times \frac{x}{\delta}\right) \cdot \exp\left(-\left(\frac{n\pi}{2}\right)^2 \cdot \Theta\right) \tag{8}$$

and the surface heat flux

$$q = \frac{2k}{\delta}\,(T_i - T_b) \sum_{n=1,3,4,\ldots}^{\infty} \exp\left(-\left(\frac{n\pi}{2}\right)^2 \cdot \Theta\right) \tag{9}$$

with

$$\Theta = \frac{\alpha t}{\delta^2}$$

Model 4: It assumes that the depth of the substrate has a finite depth and the boiling heat transfer co-efficient is also finite. Applying these conditions to the solutions of Equation (1), yields model 4 which can be expressed as below.

$$\frac{T - T_b}{T_i - T_b} = \sum_{n=1}^{\infty} \frac{2L \cdot \cos\omega_n \cdot \exp(-\beta_n^2 \Theta)}{\cos(\beta_n[L(L+1) + \beta_n^2])} \tag{10}$$

and

$$q = \frac{k(T_i - T_b)}{\delta} \sum_{n=1}^{\infty} \frac{2L^2}{L(L+1) + \beta_n^2} \exp(-\beta_n^2 \Theta) \tag{11}$$

β_n are the roots of equation $L = \beta \tan\beta$

where

$$L = \frac{h\delta}{k}$$

$$\omega_n = [\beta_n(\delta - x)/\delta]$$

During the spill on land or ground, the finite depth assumption does not hold. Therefore, from the above formulations, Model 3 and 4 are not practical for spill on land. However, it may have some use in the consequence analysis of spill on the deck of a LNG carrier. Thus the most practical among the above four models is Model 2.

Model 2 requires use of heat transfer correlations in order to estimate the thermal resistance posed by the boiling liquid. Therefore, the accuracy of using model 2 will depend on the particular heat transfer correlation.

2.2.2 Briscoe and Shaw model, 1980

Following Reid's model, Briscoe and Shaw further modified Equation (5) based on the same assumption that the conductive heat transfer from the ground is the dominant heat transfer mechanism [23]. They also combined the vaporization rate with the radius of a spreading pool formation. Ignoring the fact that upon spill, a liquid pool will spread, and the cumulative vaporization rate will be dependent on the spread area; Briscoe and Shaw proposed the incorporation of a multiplicative correction factor (χ) due to the ground thermodynamic property change, and surface roughness of the substrate. They also commented that considering LNG as a single component (*i.e.*, methane) suffices for the source-term study. They proposed $\chi = 1$ for concrete and $\chi = 3$, considering previous spill experimental results on soil substrate by Burgess and Zabetakis [24] and AGA [25]. Therefore, by ignoring the pool spreading in the model development, Briscoe and Shaw model can mathematically be expressed as follows:

$$\frac{\dot{m}}{A} = \chi \cdot \mathrm{F} \cdot t^{-\frac{1}{2}} \tag{12}$$

The major limitations of this model are primarily, the generalization of different boiling regimes and therefore it deters proper selection of heat transfer correlation. Moreover, a proper use of such model requires the thermo-physical characteristics of the ground material [26]. Without experimental data, an accurate determination of χ, would be impossible and since ground composition varies from place to place, the use of χ needs a proper caution.

2.3 Combined source-term models

A combined source-term model consists of liquid release, the pool vaporization, pool spread models. As discussed earlier, the accuracy of a combined source-term model primary depends on the vaporization term. Therefore, appropriate selection can make a difference in the consequence assessment. Webber *et al.,* have presented summary of the commercially available combined source-term models which are in practice [27]. The key features of these models in terms of selecting the vaporization source-term are presented below.

2.3.1 Raj and Kalelkar, 1974

This integral model was originally developed for the U.S. Coast Guard, primarily predicts the spreading behavior of liquid pools on water[28] and later extended for using on land [29]. While estimating the vapor formation rate, Raj and Kalelkar used the Equation 5 and experimental values provided by Reid and Wang as presented in the previous sections.

2.3.2 Opschoor, 1977

This model addressed pool vaporization and spreading on open and closed water body based on the work of Raj and Kalelkar [22]. For estimating the vapor formation rate, Opschoor used the following formula based on the experimental results presented by Boyle and Kneebone [30]. Clearly, models 1 with different experimental values were used to estimate the vaporization source-term.

$$m_w^{"} = \begin{cases} 0.008 \; for \; 0 < t \leq 25 \\ \frac{0.517}{(t-20)^{1/2}} \; for \; t > 25 \end{cases} \tag{13}$$

2.3.3 SOURCE5, 1993

Developed by Gas Research Institute (GRI) this model can be used for instantaneous and continuous releases for both on-land and on-water [31]. In SOURCE5, the heat transfer from the ground to the liquid is taken as the proportional to the $1/\sqrt{t}$ as shown in the Model 1. The mass vaporization rate is combined with the pool area therefore the pool spreading and vaporization is modeled together. The combined mass vaporization and pool spreading was modeled as follows:

$$\dot{m}_P = \frac{2e}{\sqrt{t}} \times \left\{ \left[\frac{4C^{"} V_{10} t^2}{\pi} \right]^2 - \left[\frac{4}{3} C^{"} g \dot{\delta}_{l,min} t^2 \right] \right\} \tag{14}$$

In the above equation, all parameters inside the braces are related to pool spreading. Proportionality constant e is used to account for the vaporization source-term. Clearly, the vaporization model used here is also a form of Model 1. More limitations of this model were discussed by Havens and Spicer (2007) [2].

2.3.4 SPILL

Developed by Briscoe and Shaw [23], SPILL model combines vaporization and pool spreading for water and on-land events. For the vaporization, it uses the model described in section 2.1.2. The SPILL model has been suspended and withdrawn by GASP.

2.3.5 GASP

This model was developed at Safety and Reliability Directorate (SRD) for U.K. HSE by Webber and Jones [32]. The Gas Accumulation over Spreading Pools (GASP) model combines shallow-layer equations together with vaporization rate of a circular pool to computationally simultaneously determine spreading and vaporization rate [33], [34]. In this model, heat contributions from the substrate, the atmosphere, as well as solar radiations were addressed. This model used a detail treatment of heat transfer co-efficient, *i.e.*, Model 2 of section 2.1.2, and Klimenko Correlation [35] was used for the spill on water. For spill on land a constant heat transfer co-efficient was used.

2.3.6 SUPERCHEMS

It is a general QRA software package which uses release models to estimate the source-terms in case of liquid, vapor and two phase releases from tanks, vessels or pipes or jet releases. The underlying physics is described by Saraf and Melhem [36]. The pool spreading model is basically based on GASP and validated against lab-scale test by Drake and Reid [26]. The development of this software was overseen by AIChE.

2.3.7 SAFESITE3G

It is integrated software package developed by BakerRisk for modeling discharge, dispersion, fire and explosions. In this tool, vaporization source-term were not modeled, rather a constant rate based on the experimental findings were used [37]. However, the constant source-term was combined with the pool spreading models.

2.3.8 CANARY

This software was developed by Quest Consultants Inc. which includes both LNG pool evaporation and pool dispersions based on the SLAB model. SLAB uses a boiling rate of 0.085 kg/m^2s for the vaporization source-term based on Shell Maplin Sands LNG release experiments [38]. It has the capability of model pressurized release, VCE, fires and BLEVE. An investigation of LNG facility siting using this model has been conducted by Taylor [39].

2.3.9 PHAST

The Process Hazard Analysis Software Tool (PHAST) is one of the most used tool developed by Det Norske Veritas (DNV) [40]. This tool integrates models such as discharge, combined pool formation and evaporation, vapor dispersion, fires, VCE and BLEVE. For modeling vaporization source-term on land this tool uses Briscoe and Shaw model as presented in section 2.1.2.

2.3.10 Fay, 2003

Professor Fay of MIT has published a studies on hazard assessment of LNG release on water [41]–[46]. These models were reviewed by Hightower et al. [47] and ABS Consulting [48] and raises questions about the physical justifications. In Fay's model, heat transfer to the pool from the substrate water is handled by using a "*regression velocity, ω*". In his latest paper [46], a constant value is assigned for this parameter, *i.e.,* $\omega = 5 \times 10^{-4}\, m/s$.

2.3.11 ALOHA

For modeling consequences of chemical releases, US EPA and US National Oceanic and Atmospheric Administration (NOAA) have developed this software package named Areal Locations of Hazardous Atmospheres (ALOHA). Though ALOHA was not developed to use in the cryogenic consequence analysis, Vallejo [49] has used for impact assessment of an LNG terminal. Thoman *et al.,* has made a comparison of ALOHA's capability is the source term modeling and cryogenic liquids were not involved in that assessment [50].

2.3.12 LSM90/LPOOL

Cavanaugh et al., has developed LSM90 tool for Exxon to model spills of liquids on land and water [51]. Shell incorporated this model in their HGSYSTEM code and renamed as LPOOL model. For the vaporization source-term estimation this tools use the following formula:

$$q_{ground} = \sum_{i=0}^{N} \frac{2k\left(T_{ground} - T_{pool}\right)A_i}{\sqrt{\pi\alpha}\cdot\left(\sqrt{t} - \sqrt{t_i^*}\right)} \quad (15)$$

The main limitation of this model is that it uses uniform ground temperature throughout the simulations which does not comply with the real spill scenario.

2.3.13 LSMS

Liquid Spill Modeling System (LSMS) developed by Cambridge Environmental Research Consultants (CERC) with the support of US Gas Research Institute, British Gas, Gaz de France and UK HSE. It solves 1-D axisymmetric shallow-layer equations to calculate the spreading and vaporization rate. Thermodynamic equations were used for cryogenic liquids to calculate the vaporization rate; however, this model is not widely used.

2.3.14 ABS Consulting model, 2004

In 2004, U.S. Federal Energy Regulatory Commission (FERC) contracted ABS Consulting to develop a case, to identify appropriate methods for performing consequence analysis of LNG release in water to estimate vapor dispersion and radiation hazards distance [52]. The proposed methods have later become a "*de facto*" standard for consequence analysis of LNG release on water [53]. The detailed computational methods have considered only the film boiling regime in estimating the vapor generation source-term and used Klimenko correlations [35]. However, it did not adhere to using this this correlation and finally used a constant value of 85 kW/m^2. Though neither ABS

Consulting nor FERC has developed any software tool, based on the underlying principles Mary Kay O'Connor Process Safety Center has developed a windows-based model called WINFERC [54].

2.3.15 LNGMAP

Applied Science Associates developed this GIS-based model to predict the consequences of LNG marine spills. It used GASP for the source-term modeling and was verified by comparing results of ABS Consulting and Sandia Models. Sample calculations and results were publuished by Spaulding *et al.*, [55].

2.3.16 SANDIA

Basically, Sandia National Lab has reviewed existing models and provided no particular recommendation instead provided a generic guidance for selecting models [47]. One particular recommendation of this study was to employ more accurate approach based on computational fluid dynamics (CFD) modeling.

2.3.17 FLACS

FLACS is a pseudo-CFD software for modeling gas dispersion and explosions developed by Gexcon. Recently, it added LNG pool model to predict the spreading and vaporization characteristics with the intention of using the vaporization rate for the dispersion and explosion study. A shallow-layer equation is used for solving the pool

spread, however Model 1 as presented in section 2.2.1 is used for the vaporization source term [56].

$$q_s(x, y, t) = \frac{k\ (T_i - T_b)}{\sqrt{\pi \alpha_s \left(t - t_w(x, y\ )\right)}} \tag{16}$$

Here $t_w(x, y\ )$ is the time when spill on water starts. Putting $t_w(x, y\ ) = 0$, will give us the exact form of Model 1.

2.3.18 Brambilla and Manca, 2009

Brambilla and Manca has improved Webber's model (GASP) for evaluating the liquid pool dynamics on both land and water spreading. It devoted attention to friction terms while spreading and boiling in the film regime, friction velocity, wind profile etc. The integrated model used Model 1 of section 2.2.1 for evaluating the heat transfer from the substrate to the liquid pool [57].

2.3.19 Drivas, 1982

Drivas has formulated the vaporization rate of volatile multi-component pools by assuming an ideal solution. However, this model is not applicable for boiling liquids and therefore cannot model cryogenic vaporization [58].

2.3.20 Leonnelli et al, 1994

Leonelli et al. modeled multi-component pool spreading and vaporization of ideal and non-ideal mixtures [59]. It assumes the pool is well-mixed and uniform temperature throughout the pool. For the vaporization source-term modeling it follows Briscoe and Shaw model as presented in section 2.2.2.

2.3.21 CHEMMAP

Under the contract of Minerals Management Service (MMS) of US DOI, French and Isaji developed this model to predict the trajectory, fate, impacts and bio-logical effects of chemicals and product mixtures that are accidentally released on water. This model is primarily focused on the study of oil slick [60] and thus not applicable for cryogenic liquids.

2.4 Heat transfer correlations

From the discussion of vaporization source-term models, Model 2 has the best ability for accurate estimation. However, as shown in the section 2.3, this model has not been widely used because of the accuracy of heat transfer correlations. Therefore, this section reviews the available heat transfer correlations. NFPA 59A prescribes the analysis of first 10-minutes developing scenario to determine the worst-case condition [4]. Moreover, the assumption of perfect contact between the liquid and solid-substrate in 1-D ideal models is unrealistic [27] and does not address the presence of different boiling regimes in estimating the heat transfer rate. Therefore, this study is limited to the

film boiling correlations because of the fact that early spill corresponds to the film boiling regime first and the highest temperature gradient exists during this regime. This study is also limited to the heat transfer correlations on a flat surface in order to ensure its application in the modeling of source terms.

2.4.1 Zuber heat transfer correlations

Zuber [61] introduced the concept of Rayleigh-Taylor (R-T) hydrodynamic instability to model film boiling on a horizontal surface. In case of a stabilized film, without any disturbances, it is impossible for a vapor film to grow as a bubble. Thus, disturbances were introduced as sinusoidal wave. Zuber proposed that the nearest distance of two evolving vapor bubbles should be bounded by Taylor "*critical*" and "*most dangerous*" wavelengths as defined in the later section *i.e.,* Equation (32) and Equation (35) respectively. He developed series of expressions to predict the minimum heat flux of film boiling (Leidenfrost point) by assuming two bubbles evolve per cycle from a square cell where the base of the cell is the distance between the bubbles. No clear justifications were given to determine the applicability of these expressions. His expressions are as follows:

$$\min\left(\frac{Q}{A}\right)_1 = \frac{\pi L' \rho v}{24}\left[\frac{\sigma g_c g\,(\rho_L - \rho_v)}{(\rho_L + \rho_v)^2}\right]^{1/4} \tag{17}$$

$$\min\left(\frac{Q}{A}\right)_2 = \left(\frac{1}{3}\right)^{0.25}\left(\frac{Q}{A}\right)_1$$

$$\min\left(\frac{Q}{A}\right)_3 = \left[0.4\frac{\pi\sqrt{2}}{3^{0.25}}\right]\left(\frac{Q}{A}\right)_1$$

$$\min\left(\frac{Q}{A}\right)_4 = \left[\frac{\pi\sqrt{2}}{3}\right]\left(\frac{Q}{A}\right)_1$$

$$\min\left(\frac{Q}{A}\right)_5 = \left[3^{0.25}\pi\sqrt{2}\right]\left(\frac{Q}{A}\right)_1$$

The major limitation of Zuber's model arises from the fact which expressions should be used and lack of justifications. Beside his correlations does not give the heat fluxes over the range of wall super heats rather give the minimum heat flux, *i.e.* Liendenfrost point. Therefore, it is not suitable to apply for the estimation of cryogenic vaporization rate.

2.4.2 Berenson heat transfer correlation

Berenson [62] formulated an empirical expression (Equation (3)), to calculate heat transfer co-efficient, for saturated film boiling on horizontal surfaces, based on the same analysis. In deriving this expression, it was assumed that, bubbles are spaced on a square grid of thin vapor film by a distance of "*most dangerous*" wavelength. As a result, two bubbles can generate per λ_D^2 area of heated surface at any particular moment. This two-dimensional study was improved for three dimensions by Sernas *et al* [63]. They showed that the three dimensional Taylor wavelength, λ_{D3} is $\sqrt{2}$ times larger than λ_D and the release was four bubbles per cycle from an λ_{D3}^2 area.

$$Nu = 0.425\left[\frac{\rho_v(\rho_l-\rho_v)gh_{fg}}{k_v\mu_v\Delta T}\right]^{1/4}\left[\frac{\sigma}{g\,(\rho_l-\rho_v)}\right]^{3/8} \quad (18)$$

Holster and Westwater [64] experimentally confirmed that the film boiling from a horizontal surface follows R–T instability. Their experimental study found that the film

boiling heat fluxes for water and Freon -11 (CCl_3F) are in agreement with the prediction of the Berenson correlation (Equation (18)).

The major limitation of applying this correlation to study cryogenic vaporization rate is that this correlation was not validated with any cryogenic experiments. At atmospheric condition, it was validated against n-pentane and carbon tetra chloride.

2.4.3 Klimenko heat transfer correlation

Klimenko [35] attempted to generalize the film boiling correlations on horizontal flat plates for different liquids including cryogens, therefore extending the experimental database for film boiling [65]. His correlation predicts the Nusselt number during film boiling, in a geometric system consisting of an upward facing horizontal surface, as:

$$Nu = 3.02 \times 10^{-2} Ar^{1/3}\ \mathrm{Pr}^{\frac{1}{3}}\ \mathrm{f}_1(\beta); \quad \text{for} \quad \mathrm{Ar} < 10^8 \tag{19}$$

$$Nu = 1.37 \times 10^{-3} Ar^{1/2}\ \mathrm{Pr}^{\frac{1}{3}}\ \mathrm{f}_2(\beta); \quad \text{for} \quad \mathrm{Ar} > 10^8 \tag{20}$$

Where,

$$f_1 = 1 \ \text{for} \quad \beta > 0.71$$

$$= 0.89\,\beta^{-1/3} \ \text{for} \ \beta < 0.71$$

$$f_2 = 1 \ \text{for} \quad \beta > 0.5$$

$$= 0.71\,\beta^{-1/2} \ \text{for} \ \beta < 0.5$$

$\beta = \frac{C_{p,v}\Delta T}{h_{fg}}, Ar = \frac{g\,L_c^3 \rho_v(\rho_l - \rho_v)}{\mu_v^2}$, $\mathrm{Pr} = \frac{C_{p,v}\mu_v}{k_v}$, $Nu = \frac{\bar{h}\,L_c}{k_v}$ and characteristic length, $L_c = \sqrt{\frac{\sigma_l}{g(\rho_l - \rho_v)}}$

It is important to note that Klimenko Correlation was validated for Nitrogen, Hydrogen, Helium, Ethanol, Freon-113, Freon-11, Carbon tetrachloride, pentane and water. Because of the adaptation to many chemical systems, it can exhibit deviations of +120 % to -28% when compared with Berenson correlation [35]. However, this correlation was not validated against LNG or methane experiments.

2.5 Limitations of the existing heat transfer correlations

The fundamental limitations of the existing empirical expressions, *e.g.,* the Berenson and the Klimenko correlations, are unrealistic assumptions such as; a constant film thickness, proportional relationship between the bubbles diameter and height, periodic bubble generations, periodic and alternating nature of bubbles liberating from the node (bubble location) and anti-node (tough between two bubbles) points of the heated surface. Hence, such correlations cannot predict the temporal variation of the heat flux. Additionally, these expressions (*i.e.,* Equation (3-5)) do not use local physical properties of the liquid and vapor but instead replace by the mean properties.

2.6 Conclusions

In the context of consequence analysis, consideration of film boiling regime is very important because of the fact that it corresponds to the highest temperature gradient at the beginning of spill. However, reliable and validated correlations do not exist in the literature to model the vaporization source-term of LNG spills. Therefore, existing tools use a constant heat flux or a mass vaporization rate or a velocity depression rate in Model 1. To overcome these limitations, computational fluid dynamics (CFD) tool can be employed to further clarify the physics, and, to accurately estimate the dynamic nature of film boiling and reliable study of the associated heat flux. It was also recommended by the review of Hightower *et al.,* [47].

3. NUMERICAL STUDY OF CRYOGENIC FILM BOILING[1]

Based on the literature review, computational fluid dynamics (CFD) is a great tool to enable better estimation of cryogenic source-term estimations. As film boiling regime determines the boil-off rate during the early phase of the spill, this section focuses on the modeling and simulation of film boiling using CFD.

The section is organized as follows: Section 3.1 describes the fundamental aspect of Rayleigh-Taylor (R-T) instability based on which the CFD formulations has been done. Section 3.2 gives a state-of-the-art review of the CFD study of the film boiling systems and identifies the gaps that need to be filled particularly for enabling the cryogenic source-term modeling.

Section 3.3.1 describes the mathematical formulations of the CFD model that is used to simulate a two-dimensional film boiling system. Section 3.3.2 describes the details of simulation setup in ANSYS Fluent 14.0, a commercial CFD software, to solve the mathematical formulations presented in section 3.3.1. Grid and time step sensitivity analysis is also presented in this section. Film boiling of liquid nitrogen (LN_2), LNG (as 100% liquid methane) and liquid oxygen (LO_2) are simulated using this setup. Section 3.4 discusses the results of the film boiling simulations which mainly focuses on

[1] The work presented in this Section contains material that has been reproduced with permission from: Monir Ahammad, Yi Liu, Tomasz Olewski, Luc N. Véchot, and M. Sam Mannan. "Application of Computational Fluid Dynamics in Simulating Film Boiling of Cryogens. "*Industrial & Engineering Chemistry Research* 55, no. 27 (2016): 7548-7557. Copyright 2016 by American Chemical Society, and reprinted from *Journal of Loss Prevention in the Process Industries* Vol. 44, Monir Ahammad, Tomasz Olewski, Luc N. Véchot, and Sam Mannan "A CFD based model to predict film boiling heat transfer of cryogenic liquids" Pages No. 247-254. Copyright 2016 with permission from Elsevier

interface morphology, behavior of heat flux, effects of wall superheat and the assumptions of alternating bubble generations that were considered in other CFD studies [66]. In this section, the simulated film boiling heat flux for $LN_{2,}$ LNG and LO_2 are also compared with the estimated heat flux by using the Klimenko and the Berenson correlations.

3.1 Rayleigh-Taylor (R-T) instability approach and perturbation analysis

R-T approach is based on the fact that during film boiling on a flat upward facing plate a vapor film must exist under the dense liquid phase. Because of gravity the phases will tend to invert. Based on the bubble distances, size and generation frequency resulting from the film, the heat flux can be estimated.

In a horizontal co-current system where the dense phase lays over the less dense phase as shown in Figure 5, the interface will not rise at equilibrium of force. However, it may become unstable in the presence of a disturbance $\delta(x,t)$, expressed as a wave. This phenomenon is referred as R-T instability. On the other hand if gravity acts vertical to the flow such as sea wave the instability is referred as Kelvin-Helmholtz instability.

Chang was the first to point out that in order to calculate the hydrodynamics aspects of a bubble generating from the film, there might be a wavelength equal to a critical value of R-T phenomena to exhibit waves [67]. Bellman and Pennington showed that the surface tension will stabilize and dampen out irregularities smaller than the critical value and therefore no bubble can rise from the vapor liquid equilibrium [68]. However, the disturbance with wavelengths greater than the critical wavelength, the

disturbance will amplify and eventually becomes a bubble and finally rupture from the film. Therefore, it is crucial to determine the critical wavelength of the disturbance in order to simulate a film boiling.

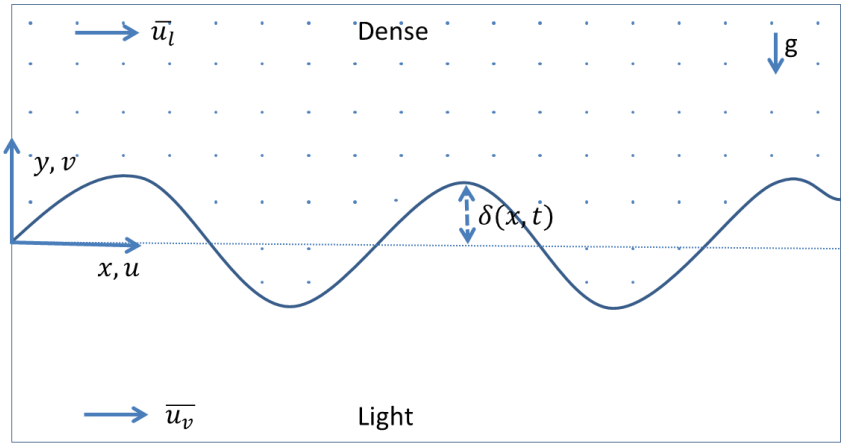

Figure 5: Rayleigh-Taylor (R-T) instability for liquid phase overlaying on vapor phase. Adapted from [69]

Carey [69] used perturbation analysis to determine the critical perturbation wavelength in order to simulate film boiling. Assuming a two-dimensional flow, the governing equations for the configurations shown in Figure 5 are:

$$\frac{\partial u}{\partial x}+\frac{\partial v}{\partial y}=0 \tag{21}$$

$$\rho\left[\frac{\partial u}{\partial t}+u\frac{\partial u}{\partial x}+v\frac{\partial u}{\partial y}\right]=-\frac{\partial p}{\partial x} \tag{22}$$

$$\rho\left[\frac{\partial v}{\partial t}+u\frac{\partial v}{\partial x}+v\frac{\partial v}{\partial y}\right]=-\frac{\partial p}{\partial x}-\rho g \tag{23}$$

Velocities and pressure can be decomposed to base flow and perturbed components:

$$u = \bar{u} + u', \qquad v = \bar{v} + v', \qquad p = \bar{p} + p'$$

Substituting in Equation (21) – (23):

$$\frac{\partial u'}{\partial x} + \frac{\partial v'}{\partial y} = 0 \tag{24}$$

$$\rho\left[\frac{\partial u'}{\partial t} + \bar{u}\frac{\partial u'}{\partial x}\right] = -\frac{\partial p'}{\partial x} \tag{25}$$

$$\rho\left[\frac{\partial v'}{\partial t} + \bar{u}\frac{\partial v'}{\partial x}\right] = -\frac{\partial p'}{\partial x} \tag{26}$$

Where the products of perturbation (primed) are neglected and

$$\frac{\partial \bar{u}}{\partial x} = \frac{\partial \bar{u}}{\partial y} = \bar{v} = 0$$

Substituting the summation of Equation (25) and (26) after differentiating with respect to x and y in continuity equation, Laplace equation for the pressure perturbation field can be found:

$$\frac{\partial^2 p'}{\partial x^2} + \frac{\partial^2 p'}{\partial y^2} = 0 \tag{27}$$

Let's assume the shape of the interface at time t as [70]:

$$\delta(x,t) = Ae^{i\alpha z + \beta t} \tag{28}$$

thus the perturbation quantities p' and v' can take the following forms:

$$v'(x,y,t) = \hat{v}e^{i\alpha x + \beta t} \tag{29}$$

$$p'(x,y,t) = \hat{p}e^{i\alpha x + \beta t} \tag{30}$$

Where $\hat{v}$ and $\hat{p}$ are the magnitude of perturbation.

Using Laplace equation and the equation for curvature of the liquid film, $p_v - p_l = \sigma/R$, Carey [69] used the perturbation analysis to obtain the condition for an unstable interface

$$|\overline{u_l} - \overline{u_v}|^2 = \frac{\left[\sigma\alpha + \frac{(\rho_l - \rho_v)g}{\alpha}\right](\rho_l + \rho_v)}{\rho_l \rho_v} \tag{31}$$

where $\alpha = 2\pi/\lambda$ is the wave number.

For this configuration, surface tension and gravity tend to stabilize the interface. The right hand side of the inequality has a minimum when the wave number is equal to the critical wave number. The corresponding "*critical wavelength"* is

$$\lambda_c = 2\pi \left[\frac{\sigma}{(\rho_l - \rho_v)g}\right]^{1/2} \tag{32}$$

This gives the critical instability

$$|\overline{u_l} - \overline{u_v}| = \left[\frac{2\,(\rho_l - \rho_v)}{\rho_l}\right]^{1/2} \left[\frac{\sigma(\rho_l - \rho_v)g}{\rho_v^2}\right]^{1/4} \tag{33}$$

During the critical condition, the system defined in Figure 5, becomes a motionless liquid over a motionless vapor ($\overline{u_l} = \overline{u_v} = 0$). If a perturbation has a wavelength greater than λ_c, it will grow and result in bubble generation from the film. In other words, if the length of interface in the x direction is less than λ_c , the interface is stable because a perturbation of wavelength less than λ_c cannot arise.

A specific value of α, exist where β in Equations (31) – (33) is at its maximum.

$$\alpha_{max} = \left[\frac{(\rho_l - \rho_v)g}{3\,\sigma}\right]^{1/2} \tag{34}$$

The disturbance wavelength corresponding to α_{max}, is referred as the "*most dangerous wavelength*" λ_D –

$$\lambda_D = 2\pi \left[\frac{3\sigma}{(\rho_l - \rho_v)g}\right]^{1/2} = \sqrt{3}\,\lambda_c \tag{35}$$

In order to simulate the fastest growing bubble, the disturbance wavelength is given by the most dangerous wavelength as shown in Equation (35).

3.2 CFD simulations of film boiling: state-of-the-art review

Numerical simulation of horizontal film boiling was pioneered by Son and Dhir [66]. The authors studied bubble and film dynamics for water boiling using moving-mesh method and also presented a combined scheme for nucleate and film boiling [71]. Further considerations for near critical conditions of water in an axisymmetric horizontal film boiling has been studied to provide steady-state bubble release pattern [72]. Panzarella *et al.* [73] modeled film boiling of water by using a lubrication approximation and thereby solving a strongly-nonlinear evolution equation. Banerjee [74] simulated sub-cooled film boiling of water on a horizontal disk. Juric [75] used added interfacial source-terms in the continuity equations on a Eulerian grid to simulate horizontal film boiling of low density ratio fluid to high density ratio fluid. This numerical method is further improved by Esmaeeli [76], [77] by elimination of iterative algorithm. Welch [78] used Youngs' [79] volume of fluid (VOF) method to simulate saturated horizontal film boiling and conjugate heat transfer. Using this method, Welch and Rachidi [80] simulated film boiling of water in contact with steel. Yuan *et al.,* [81] simulated the film boiling of water on a sphere on a non-orthogonal body fitted coordinates. Agarwal *et al.,* [82] simulated film boiling of water at 373^{o}C, 219 bar using a variant of VOF method to

study the unsteady bubble release patterns, transport coefficients and influence of fluid properties. Tomar *et al.*, [83], [84] and Hens *et al.*, [85] studied water and refrigerant R134a at near and far critical pressures using coupled level-set and Volume of Fluid (CLSVOF) method. Welch and Biswas [86] and Tomar *et al.*, [87] investigated the effect of electrical potential on heat transfer by performing direct simulation of film boiling. Liu *et al.*, [88] studied pool boiling of liquid nitrogen using commercial computational fluid dynamics package ANSYS-Fluent. Despites, many studies as mentioned above address film boiling numerical approaches, bubble generation dynamics and associated heat transfer, no notable attempts have been taken to simulate cryogenic fluid boiling particularly LNG for the application of vaporization source-term estimation. The most studied boiling systems are water and refrigerants at near-critical pressures. Hence, this study addresses film boiling of cryogenic systems (*i.e.* LNG, LN_2, and LO_2) at atmospheric conditions, is particularly useful for reliable estimation of cryogenic boiling, *e.g.*, LNG source-term modeling.

3.3 Film boiling of cryogenic liquids using CFD

The mathematical formulations of the film boiling modeling are as follows:

3.3.1 Mathematical formulations

Commercial CFD software ANSYS Fluent was used to implement and solve the formulation of the film boiling model as described in the following.

3.3.1.1 Interface tracking using VOF method and calculation of curvature

Volume of Fluid (VOF) method is used to capture the vapor-liquid interface in a fixed Eulerian mesh. A single set of momentum equation as shown in next sections is solved to determine the volume fraction (α) in each computational cell. In a control volume (*i.e.,* a single cell of the solution domain), the summation of the volume fractions of liquid and vapor phase is equal to unity. For example, boiling of one component two-phase system, each cell in the solution domain is either filled with liquid, vapor, or a mixture of liquid and vapor phases (say 50% liquid and 50% vapor); where in any case, the summation of volume fraction will be 1. Thus for a multiphase cell, the cell or node property value or field variable value represents the volume-averaged value. If q^{th} fluid's volume fraction in a cell is denoted by α_q, then

- If $\alpha_q = 0$; the cell is empty of q^{th} fluid
- If $\alpha_q = 1$; the cell is full of q^{th} fluid
- If $0 < \alpha_q < 1$; there is an interface in the cell between q^{th} fluid and at least one other fluid.

The VOF method is based on the conservation of α with respect to time and space as expressed in the following Equation. This fundamental idea was originated by Hirt and Nichols [89].

$$\frac{\partial \alpha}{\partial t} + \vec{v} \cdot \nabla \alpha = 0 \tag{36}$$

Several researchers applied this method for simulating film boiling. Hardt and Wondra [90] proposed a method for applying VOF to perform film boiling simulations

and droplet evaporation. Kunkelmann [91] implemented VOF solver in the open-source CFD package 'OpenFoam' to solve incompressible two-phase problems. Kunugi [92] performed a comprehensive review of the latest simulation pool and film boiling. Further information on VOF use can be referred to Kunugi [92].

In ANSYS-FLUENT, the tracking is accomplished by the solution of continuity equation for the volume fraction of one phase (page- 475 [93]). For q^{th} phase, this equation is:

$$\frac{1}{\rho_q}\left[\frac{\partial}{\partial t}\left(\alpha_q \rho_q\right) + \nabla \cdot \left(\alpha_q \rho_q \vec{v}_q\right)\right] = S_{\alpha_q} + \sum_{p=1}^{n}\left(\dot{m}_{pq} - \dot{m_{qp}}\right) \tag{37}$$

Where $\dot{m}_{qp}$the mass transfer rate from the phase q to the phase p, S_{α_q} is the mass source term. The primary fluid in this study is considered as gas phase. Thus the above-mentioned equation is solved for liquid phase only. Vapor phase volume of fraction is calculated using the constraint:

$$\sum_{q=1}^{n} \alpha_q = 1 \tag{38}$$

Based on the need of interface reconstruction, VOF methods are categorized into two categories, *i.e.*, those that require vapor/liquid interface reconstruction and those that do not. SOLA-VOF (based on Donor-Acceptor method) [94], FCT-VOF [95] and CICSAM (Compressive interface capturing scheme for arbitrary meshes) [96] do not require interface reconstruction. SLIC (Simple Line Interface Calculation) [97] and PLIC (Piecewise Linear Interface Calculation) [79] methods require reconstruction of interface. Because PLIC method provides more accurate solution than the other methods,

a more realistic representation of the actual interface is possible via this method (Figure 6). Thus, it was chosen to use as the interface reconstruction method in this study.

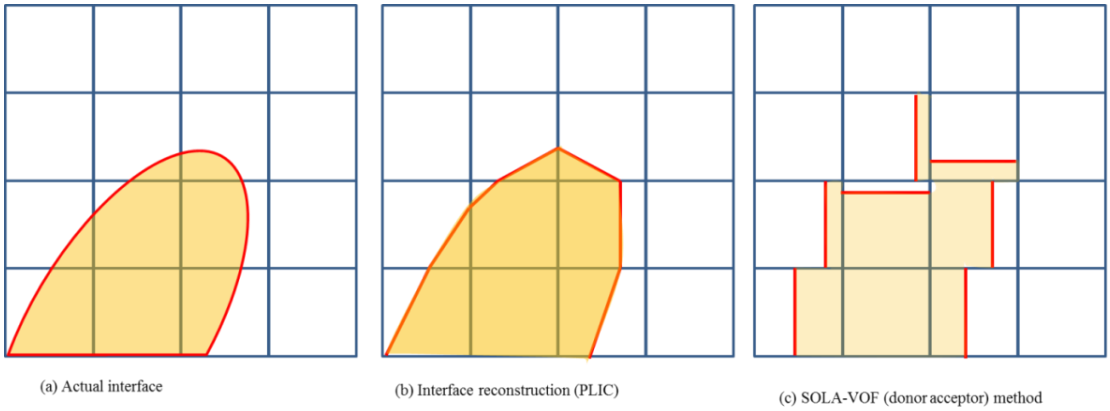

Figure 6: (a) Actual vapor-liquid-interface (b) Interface reconstructed using PLIC (c) Interface using donor-acceptor scheme.

3.3.1.2 Material properties

The material properties in the transport equations are computed as follows.

$$\rho = (1-\alpha)\rho_v + \alpha\rho_l \tag{39}$$

$$\mu = (1-\alpha)\mu_v + \alpha\mu_l \tag{40}$$

$$k = (1-\alpha)k_v + \alpha k_l \tag{41}$$

3.3.1.3 Governing equations

A single momentum equation is solved for the entire computational domain. The calculated velocity field is shared among the vapor and the liquid phases. The momentum equation shown in Equation (12) is dependent on the volume fractions of both phases via average material properties.

$$\frac{\partial(\rho\vec{v})}{\partial t} + \nabla\cdot(\rho\vec{v}\vec{v}) = -\nabla p + \nabla\cdot[\mu(\nabla\vec{v} + \nabla\vec{v}^{T})] + \rho\vec{g} + \vec{F} \tag{42}$$

For the incompressible flow, the mass conservation equation is

$$\nabla\cdot\vec{v} = 0 \tag{43}$$

The energy equation is also dependent on the volume fractions of both phases via the material properties, and, is shared among the phases within a computational cell.

$$\frac{\partial}{\partial t}(\rho E) + \nabla\cdot\left(\vec{v}(\rho E + p)\right) = \nabla\cdot(k\,\nabla T) \tag{44}$$

Enthalpy (E) and temperature (T) of each cell is considered as a mass-averaged quantity given by the following equation:

$$E = \frac{\sum_{q=1}^{n}\alpha_q\rho_q E_q}{\sum_{q=1}^{n}\alpha_q\rho_q} \tag{45}$$

Here, E_q is based on specific heat of q^{th} phase and the temperature of computational cell.

3.3.1.4 Continuum surface force model

Surface tension in the interface creates a jump in density and energy across the interface. The continuum surface force (CSF) model developed by Brackbill *et al.* [98] is used to capture this jump conditions via addition of surface force as source-term in the

momentum equation. It is expressed as the jump in pressure across the interface as shown by:

$$F_{vol} = \sigma_{qp} \frac{\rho \kappa_q \nabla \alpha_q}{\frac{1}{2}(\rho_p + \rho_q)} \tag{46}$$

3.3.1.5 Discretization

First order implicit discretization is used for transient formulation of time. PISO (Pressure implicit with splitting of operator) algorithm is used solving the governing equations. PRESTO, pressure discretization scheme is selected because of its effectiveness in multiphase system. For momentum and energy discretization, the QUICK algorithm is used [93].

3.3.1.6 Discretization of VOF equation

First order implicit scheme is used for time discretization, therefore, ANSYS Fluent's standard finite difference interpolation scheme; QUICK is used to obtain the face fluxes for all cells.

$$\frac{\alpha_q^{n+1}\rho_q^{n+1} - \alpha_q^n \rho_q^n}{\Delta t} V + \sum_f \left(\rho_q^{n+1} v_f^{n+1} \alpha_{q,f}^{n+1}\right) = \left[S_{\alpha_q} + \sum_{p=1}^{n} \left(\dot{m}_{pq} - \dot{m}_{qp}\right)\right] V \tag{47}$$

Iterative solution of a standard scalar transport equation for the secondary-phase volume fractions at each time step determines the volume fraction values at the current time step.

3.3.2 Simulation setup

During film boiling, a sustained film of vapor is always present between the solid substrate and boiling liquid. Phase change (liquid to vapor) occurs at the vapor-liquid interface. It is assumed that the surface roughness of the substrate is much smaller than the film thickness hence no significant effect on film boiling. It is also assumed that the bubble generation from the vapor film follows a regular pattern. Therefore, heat transfer from a large area can be estimated by repeating the simulated domain. From Figure 7, one bubble evolves in each cycle from a square cell of area λ_{d2}^2, where λ_{d2} is the *"most dangerous"* Taylor wavelength. The point at which bubbles are growing is referred to as *node* and the valley of two adjacent bubbles is named *antinode*. To consider the symmetry of the bubbles over the entire hot surface, a horizontal length of $\lambda_{d2}/2$ needs to be simulated as shown in Figure 8. To capture the bubble dynamics properly, the height of the two-dimensional simulation domain is considered as three times the width of the domain [99]. The bottom of the domain is considered as a heated wall at a constant temperature whereas the top of the domain is considered as vapor outlet.

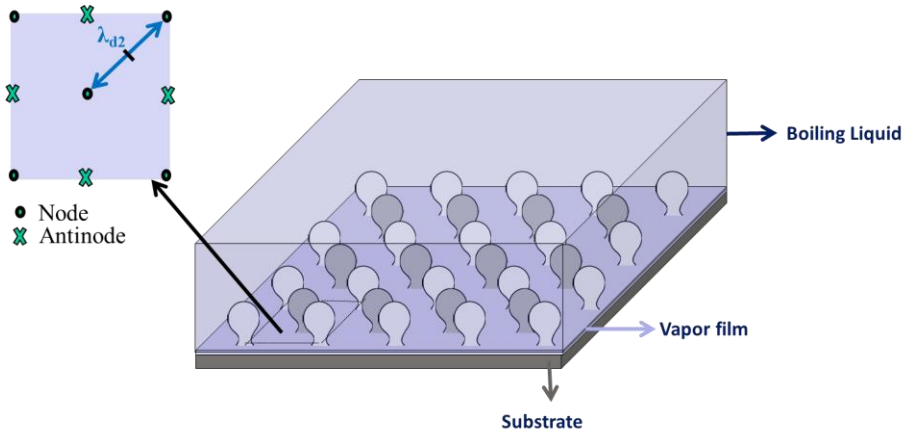

Figure 7: R-T instability approach for film boiling simulation using CFD

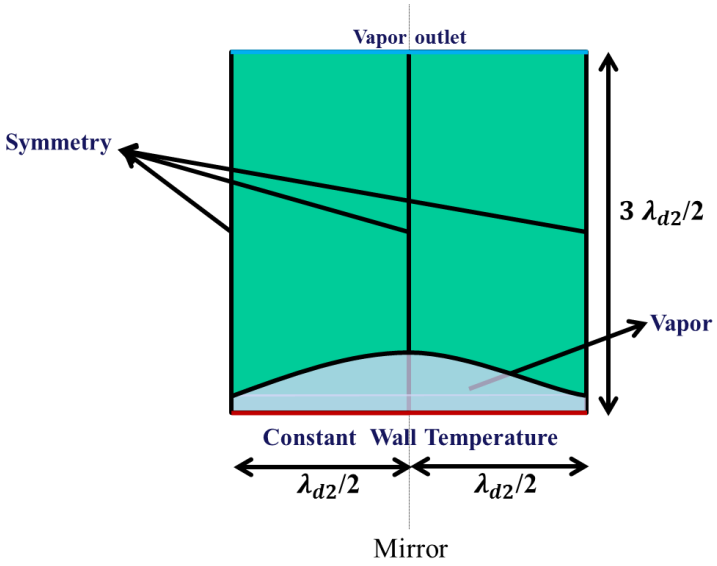

Figure 8: Setup of 2D film boiling simulations

The simulation is initialized with a linear temperature profile in the vapor film at the bottom of the computational domain as shown in the following equations. The initialized vapor film takes the form of a sinusoidal perturbation that induces R-T instability in the computational domain thus enabling the simulation of film boiling

phenomena. The simulation set-up is benchmarked by reproducing the film boiling case described in section 4.4 of Gibou *et al.* [100].

$$\delta = \frac{\lambda_{d2}}{64}\left(4 + \cos\left(\frac{2\pi x}{\lambda_{d2}}\right)\right) \tag{48}$$

$$T_y = \begin{cases} T_{wall} - \Delta T \cdot y/\delta \;\; for\; \alpha = 1 \\ T_{sat} \;\; for\; \alpha = 0 \end{cases} \tag{49}$$

3.3.2.1 Grid sensitivity analysis

Three mesh resolutions of size 32x96, 64x192 and 96x288 were used to assess sensitivity of film boiling model to the mesh resolution. Figure 9 shows the bubble interfaces for three different mesh resolutions at a time of 0.18 second which corresponds to 90,000 iterations for $\Delta T = 43\ K$. It is observed from the figure that the bubble evolution speed is greater for the denser grid. The difference between the height and diameter of the bubbles for the grid size of 32x96 with the grid size of 64x192 is not very significant. The bubble heights at 0.18 second of flow time for 32x96 grids and 64 x 192 grids are correspondingly 3.6 mm and 7.21 mm. Therefore the deviation in height for these two grids is about 100%. However, the height of the bubble for 96x288 grids is almost same as 64x192 grids 7.27 mm; therefore the deviation in height is less than 1%. From Figure 9, a deviation in the bubble radius is also observed. Usually higher mesh resolution results greater bubble radius. However, 32x96 mesh shows greater diameter because of the fact at this iteration level the bubble was still growing whereas for other grid resolutions, the bubbles were about to leave the film. Comparing the interface of

32x96 grid with 64x192 grid at the height of 1 mm indicates that the bubble radius 32x96 grid is 155% that of 64x192. Similarly, comparing the results of 64x192 grids with 96x288 grids at a height of 6 mm, it is found that the bubble radius of 96x288 is 18% greater than 64x192. Though there is a difference between the interfaces evolution for different grids, considering the benefits and the cost of computer runtime, 64x192 grid resolution is used as a working grid in this study.

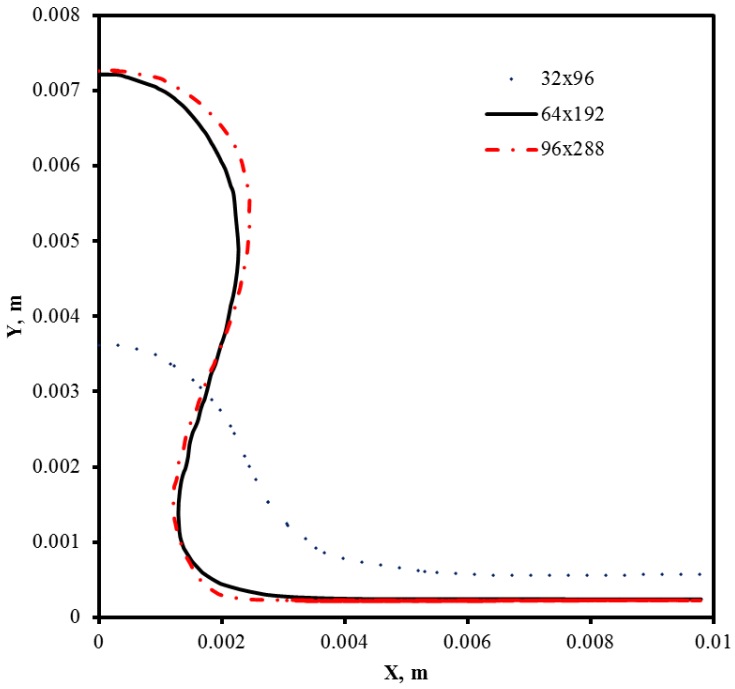

Figure 9: Grid sensitivity with respect to bubble growth during film boiling of LNG

3.3.2.2 Time step sensitivity analysis

Time step has been chosen to satisfy Courant-Friedrichs-Lewy (CFL) condition for the convergence of the simulations. Figure 10 depicts the difference between the bubble evolution for a time step of $\Delta t = 0.0001$second and $\Delta t = 0.00001$second. The maximum difference between the heights is less than 0.1%. Therefore, a working time step ($\Delta t = 0.0001$sec) is used for all the simulations. It takes about 800 minute to simulate 2 bubble generations in ANSYS-FLUENT package installed in a terminal server with Intel I Xeon I CPU, dual 3.33GHz processors and 32.0 GB of installed RAM.

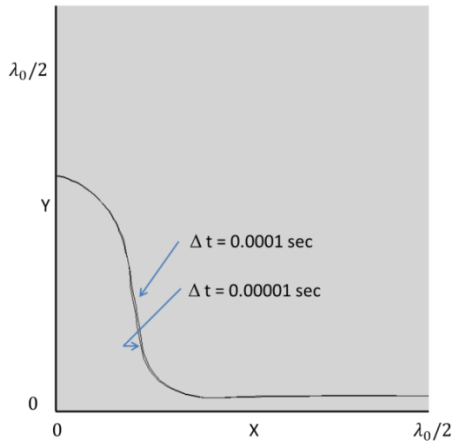

Figure 10: Time convergence study showing the bubble interface at 0.67 second using 64x192 meshes for different time steps.

Figure 11 displays the time step sensitivity in terms of the calculated wall heat flux for a wall superheat of 32K for LO_2. There is no significant difference between the

wall heat flux calculated for a larger time step, *i.e.*, 10^{-4}s and an order smaller time step, *i.e.*, 10^{-5}s. As a result 10^{-4}s time step is followed because it will decrease computational time for the subsequent calculations.

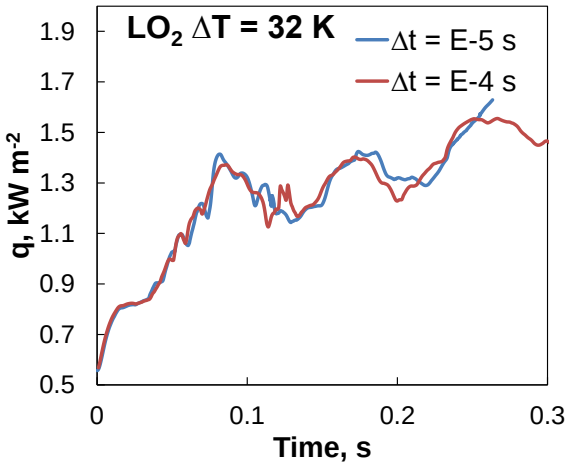

Figure 11: Time step sensitivity of the wall heat flux for liquid oxygen film boiling

3.4 Results and discussions

The temperature dependent physical properties of both liquid and vapor phases of nitrogen is estimated based on the correlations provided in DIPPR [101] database and the physical properties of LNG, as pure methane is collected from Barron [102].

3.4.1 LN_2 film boiling

Figure 12 presents the evolution of a bubble from the initial sustained film at a wall superheat of 32K. In the beginning, the node point has the highest thickness of the vapor film. The average film thickness is also highest. Therefore, the heat flux at the wall is the lowest. As the interface grows, the generated vapors move towards the node and therefore, it also draws the vapor from its sides resulting in decrease of the average film thickness. As shown in the Figure 6 (c), when the bubble is about to detach, the average vapor film thickness is the lowest, therefore, the wall heat flux reaches its peak which is shown in Figure 13. After the detachment of the bubble, some vapor from the vertical stem returns to the film in contact with the wall. The average film thickness therefore increases again, resulting in drop in the wall heat flux. This process is repeated in between node and antinode. Figure 13 depicts the wall heat flux for bubble generation over 7 cycles.

The time weighted average wall heat flux due to film boiling simulation is compared with the Berenson and Klimenko correlations as depicted in Figure 13. The Berenson correlation was validated for pentane and other high boiling point fluids[103] whereas the Klimenko correlation is validated against liquid nitrogen [35]. It is clear that the average heat flux from film boiling simulation is slightly higher than that derived by the Klimenko correlation.

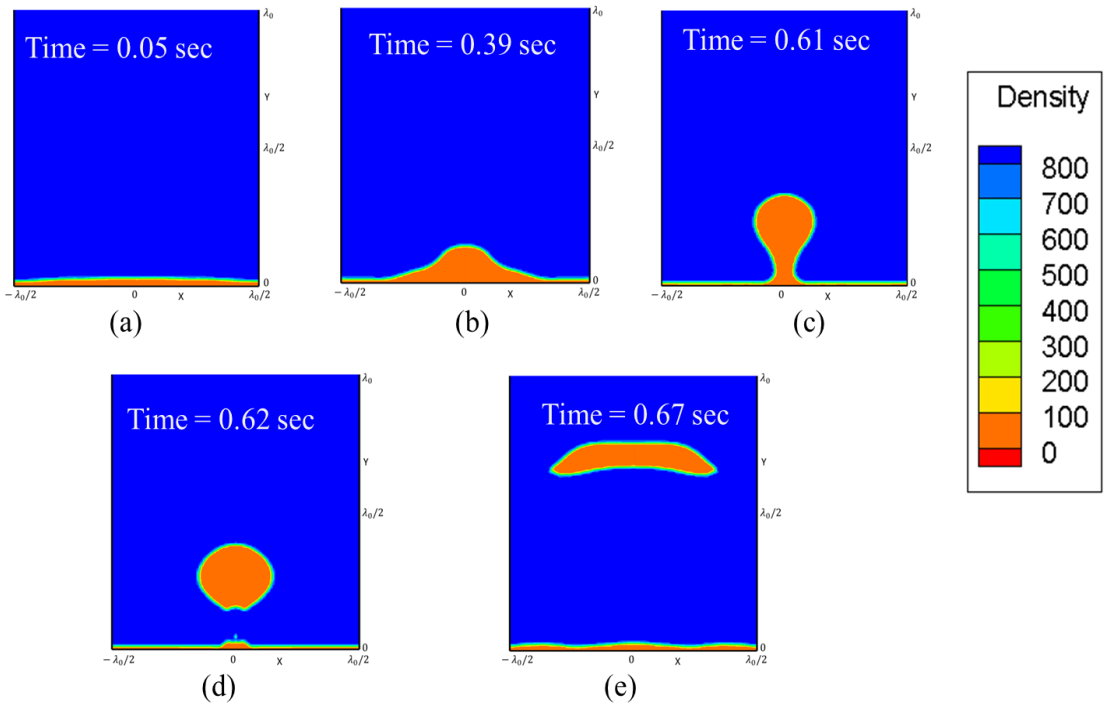

Figure 12: Evolution of bubbles during LN_2 film boiling at wall superheat of 32 K

Figure 13 shows the heat flux distribution of the simulation performed for 4 seconds. Seven bubbles were released in this period of time. It is clear from this figure that the heat flux varies dynamically with bubble release. The time weighted average heat flux for this case is about 1600 W/m^2. Whereas the Berenson correlation estimates about 6037 W/m^2 and Klimenko estimates about 1295 W/m^2. It is to be noted that the Klimenko correlation was validated for LN_2 and is more reliable than the Berenson correlation for simulating LN_2 film boiling.

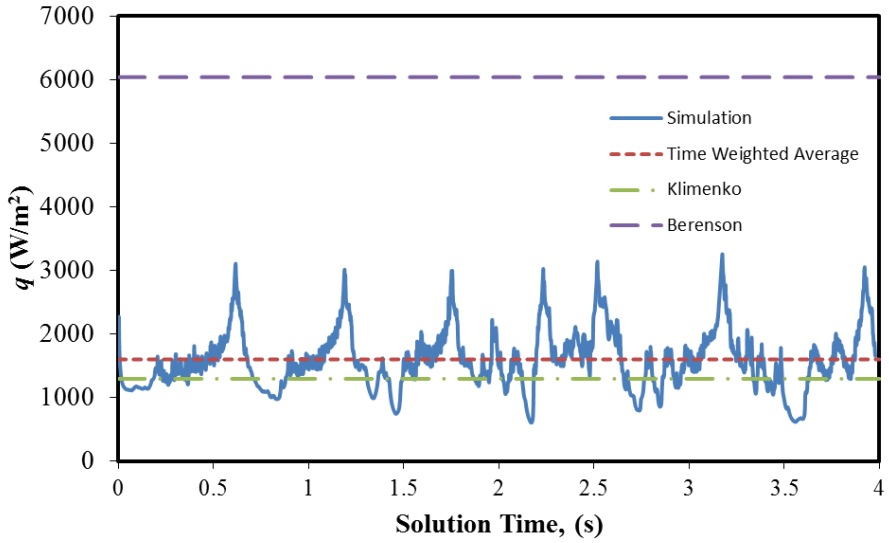

Figure 13: Simulated wall heat flux for film boiling of LN_2 at $\Delta T = 32\ K$

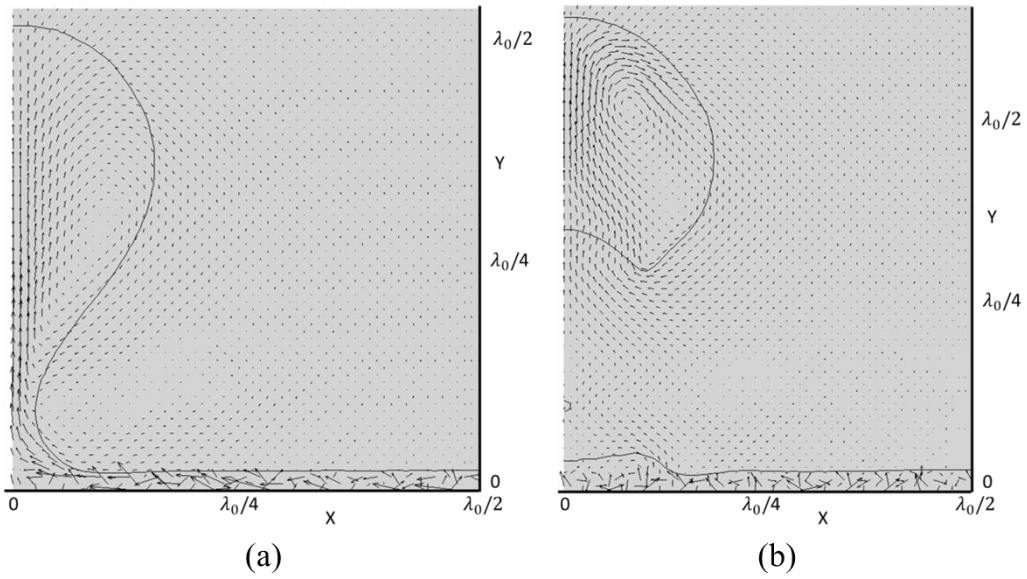

Figure 14: Velocity vectors for LN_2 a wall superheat of 73 K. (a) Before bubble release (b) After bubble release

Figure 14-(a), the velocity vector plot, shows that velocity is small in most part of the liquid phase away from the bubble. The highest velocity exists in the vapor film. Vapor is moving towards the center of the bubble, *i.e.,* towards the node. In the centerline of the bubble, close to the necking point, the velocity is higher. It is also observed that high velocity gradients exist near the necking point as the liquid moves in to fill the gap. The minimum wall film thickness is observed close to the necking point. Thus maximum amount of vapor is produced in that zone. After the bubble was released, as shown in Figure 14-(b), a portion of vapor from the bubble stem returned to the film due to the capillary forces. Vapor in the film travels towards the antinode. However, the vapor generated from the minimum thickness point is still moving towards the node. When the bubble is released, wake formation in the liquid below the bottom interface of the bubble pushes the bottom interface up forming an inverted cup formation. As the bubble rises, it tries to adjust spherical shape due to the surface tension. However, the inverted cup formation becomes ellipsoidal (or more like a cap shape) as it grows upward. Meanwhile, the disturbance travels towards the antinode as shown in Figure 14(b) and subsequently the bubble forms at the antinode.

From Figure 14, it is seen that vapor velocity is higher than the liquid velocity. This can also be correlated with the temperature distribution profile. The temperature distribution as shown in Figure 15 indicates that, the liquid is mostly uniform at its boiling point, whereas the vapor phase is superheated. Comparing both figures, it can be reasonably concluded that the velocity vector is directly related with the temperature. Furthermore, Figure 15 shows an interesting pattern on the wall. A wavy temperature

profile exists at the boundary condition. This might be connected with the movement of minimum thickness point. The local highest temperature gradient can be observed at the locations of local minimum thickness point. Furthermore, it is clear that the isotherm follows the shape of interface.

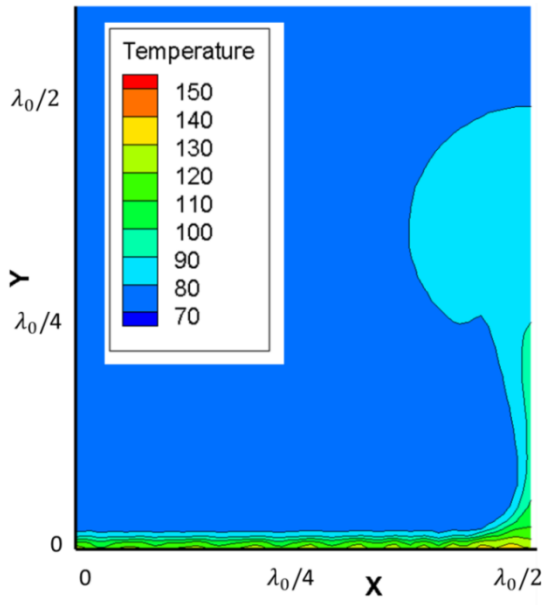

Figure 15: Temperature distribution during the film boiling for LN_2 at 73K wall superheat and solution time at 0.25 second.

3.4.2 LNG film boiling

Figure 16 - (a), (b) and (c) shows the bubble evolution and streamlines of vortex formation. Similar to LN_2 film boiling, LNG vapor in the film moves towards the node and forms the bubble. When the bubble leaves the film, due to wake formation in the liquid phase, the bottom interface of the bubble inverts to take the shape of cup. The

streamlines clearly depict the locations of heat transfer in the vapor liquid interface. The maximum amount of heat transfer occurs at the minimum thickness point. Generated vapor moves toward the bubble and therefore the bubble continuously pushes the liquid. As a result there is a wake formation in the liquid phase. It is clear from Figure 16 that the vortex forms at the location inside the bubble with a lowest curvature. After the bubble is released, formation of vortex is at the location of retracted film.

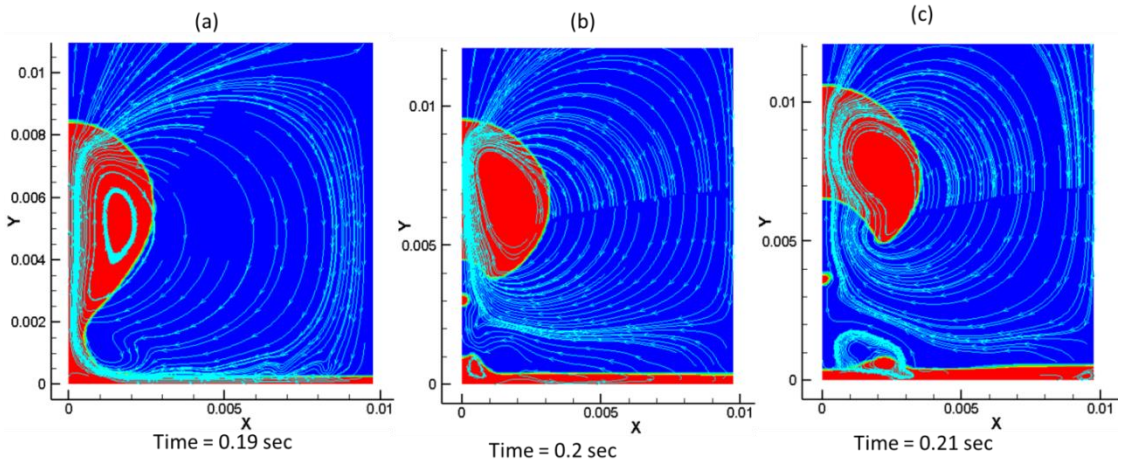

Figure 16: Streamlines showing the vortex formations for LNG at a wall superheat of ΔT = 43K.

Figure 17 depicts the area weighted average wall heat flux as a function of time. Due to the heat transfer, vapor is generated at the vapor liquid interface and thus the film thickness increases. Therefore the average heat flux decreases. As the vapor production continues, vapor from the film moves toward the node. As a result bubble starts growing at the node and because of the vapor deficiency in the film, the average film thickness decreases and the heat flux increases. When the bubble leaves the film, a portion of vapor retracts to the film causing an increase of average film thickness therefore heat flux at the wall suddenly drops. Each peak in Figure 17 represents the formation of one bubble. At the beginning of the simulation, the liquid was quiescent. However, after one or two bubble formations, there is a significant amount of wake or churning motion in the liquid phase, which further affects the film thickness. The complicated interactions of the liquid phase, film-thickness, and interface movements represent a realistic film boiling scenario. Therefore the heat flux peaks as shown in Figure 17 are not entirely periodic.

From Figure 17, the simulated average heat flux is 12691 W/m^2 whereas Berenson and Klimenko correlations predict 6970 W/m^2 and 1639 W/m^2 respectively. Therefore for LNG, the CFD simulations results is much higher estimations (factor of 8) of source-terms compared to Klimenko correlation. This finding is aligned with the experimental observation of the LNG spill experiments and will be discussed in Section 4.

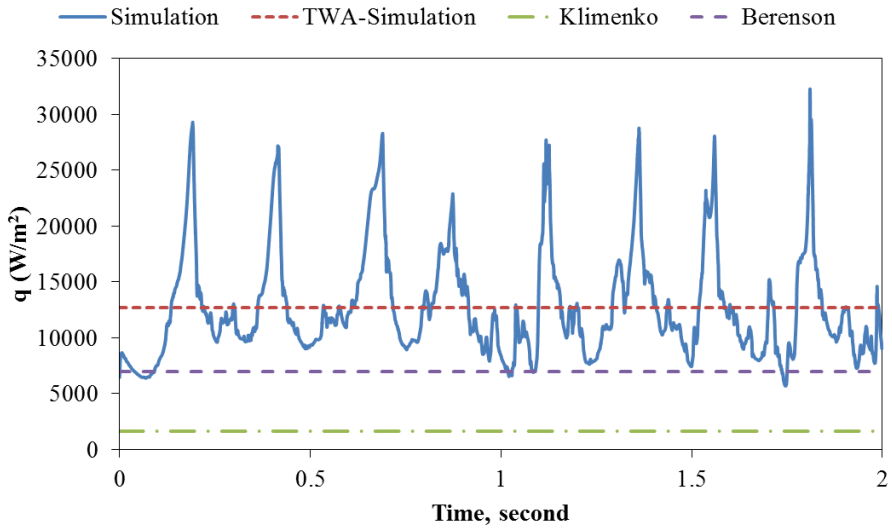

Figure 17: Surface heat flux for the film boiling of LNG at ΔT = 43 K.

3.4.3 Non – alternating bubble generation

Many previous studies assumed alternating bubble generations from the node and anti-node points [81], [62] , [65], [71]. However, from this study, it is found that the alternating character of bubble generations depends on the steadiness of the liquid pool and also the depth of the pool. Figure 18 shows the bubble generation from node and antinode points for different wall superheat during the film boiling of liquid nitrogen. In Figure 18, if the bubble is released from the right side of the contour, it is said to be released from the node point whereas if it is released from the left side of the contour it is said to be released from anti-node points. As depicted in the Figure 18, for a wall superheat of 32 K, the first five bubbles were released from the node point and the sixth bubble was released from the antinode point. Similarly, for $\Delta T = 73K$, the first and second bubbles were released from node points and subsequent three bubbles were

released from the antinode points. For $\Delta T = 103K$, the first bubble was released from the node point, the second and third bubbles were released from the antinode point and the subsequent three bubbles were released from node points. The dependency of the bubble release location depends on the motion of the vapor which is further influenced by force created at the vapor-liquid interface by the liquid velocity. When the depth of the pool is significantly small, the top surface movement also influences the motion of the liquid and therefore, the release location of the bubble generation. During the accidental spill of cryogenic liquid, *e.g.,* LNG, the film boiling will occur mainly in the spreading pool front where the depth of the pool is significantly low. Therefore, bubbles generating from the spreading front may not follow the switching nature of bubble release locations from node point to anti-node point. Thus, empirical expressions which assume alternating nature of bubble release locations may cause erroneous estimation of vapor generation.

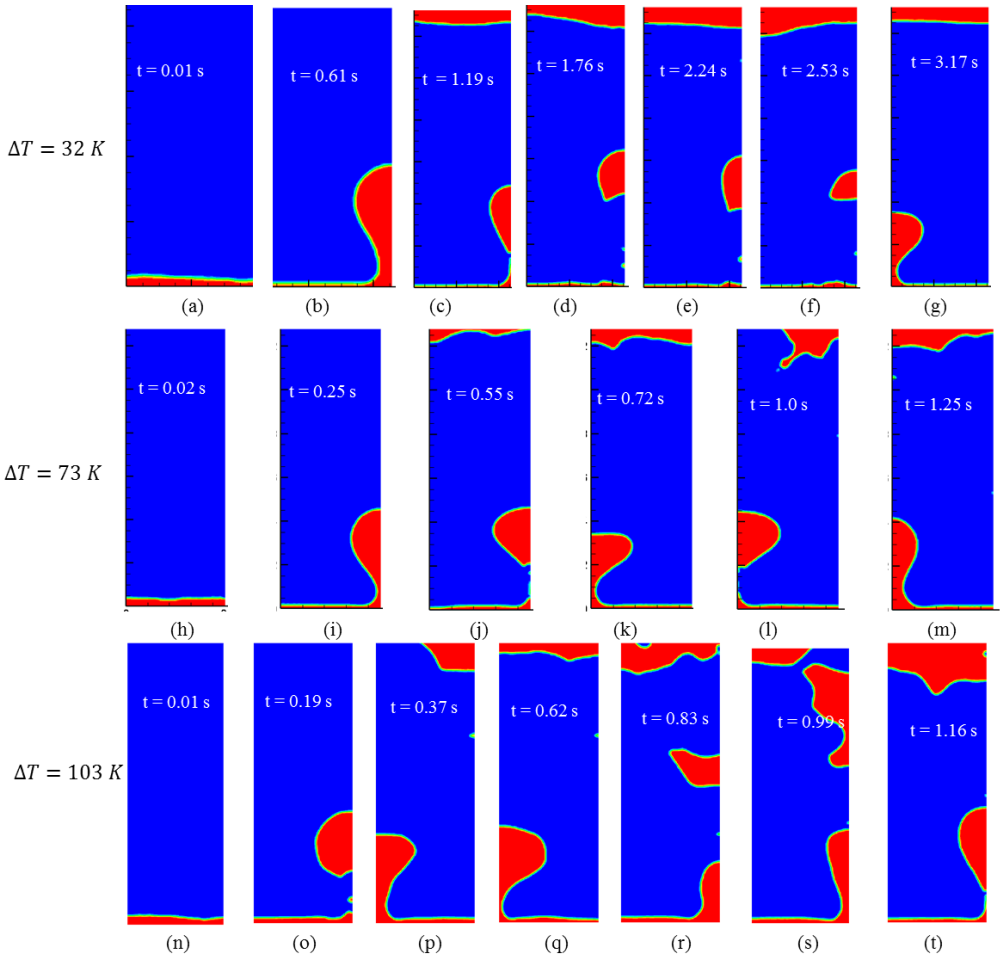

Figure 18: Effect of wall superheat on bubble generation frequency during LN_2 film boiling

3.4.4 LO_2 film boiling

The film boiling of liquid oxygen was studied by taking the same approach as discussed in the earlier sections. LO_2 film boiling was simulated for the wall superheats of 32K, 73K, 103K, 153K and 196K. Figure 19 shows the wall heat flux for a wall superheat of 32K. There are three large peaks and two small peaks in between the larger

peaks. The larger peaks resulted from bubbles which were less affected by the liquid motion whereas the bubbles which resulted from the liquid motion caused the smaller peaks.

From Figure 19, the average simulated wall heat flux is found 1.44 kW/m^2. Berenson and Klimenko correlations estimate the heat fluxes to be 2.3 kW/m^2 and 0.4 kW/m^2 respectively.

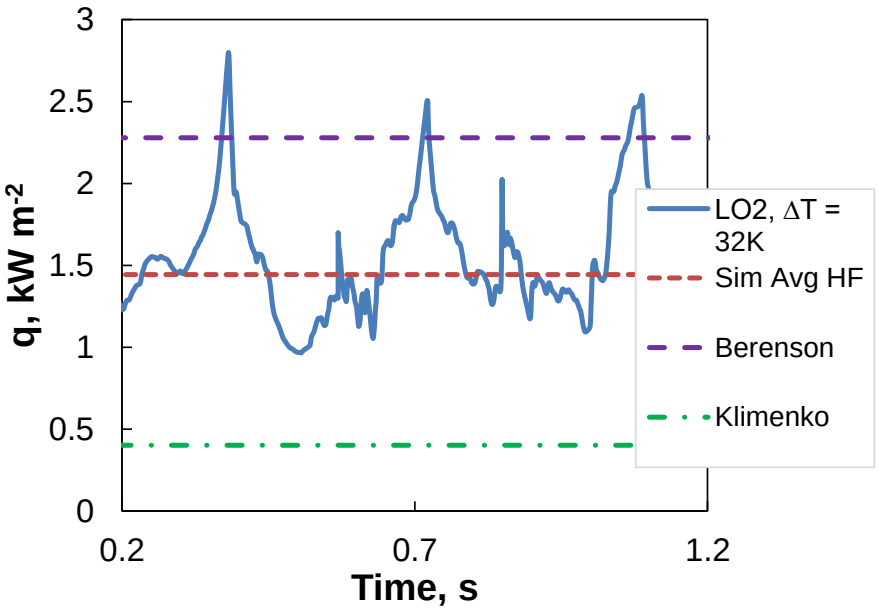

Figure 19: Wall heat flux for liquid oxygen at ΔT = 32K

Figure 20 presents the results of LO_2 film boiling simulations. It is clear that the simulated average wall heat flux increases linearly with the increase of wall superheats. The simulated average wall heat flux is compared against the estimations based on

Berenson and Klimenko correlations and it is found that the simulated results agree with Berenson correlation at higher wall superheats. However, gives a slight underestimation at the lower wall superheat conditions.

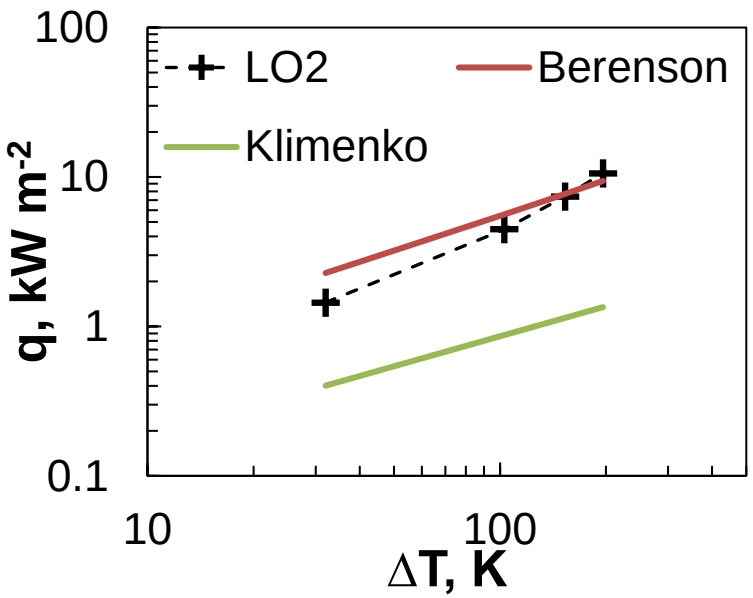

Figure 20: Simulated wall heat fluxes of liquid oxygen film boiling

3.4.5 Behavior of wall heat flux

The heat flux from the solid wall during the film boiling strongly dependent on the thickness of the film as also observed in other studies [82], [83]. The behavior of heat flux can be explained by the behavior of the sustained film thickness during the bubble evolution. As vapor phase presents greater thermal resistance than the liquid

phase; and thus these locations where the film thickness is smaller have higher heat flux than that of a thicker film. From Figure 21, the heat flux decreases as the film thickness increases steadily in the beginning of bubble generation. At 0.05 second the vapor reaches at the most stable uniformly distributed condition. Vapor start pushing the bubble at this time and slowly builds up the bubble. As vapor from the film moves towards the bubble, the thickness of the film decreases on the surface because of the vapor deficiency. As a result the area weighted average heat flux increases with time. At around 0.18s (see Figure 21 (a)) the bubble grows to its maximum size and is about to leave the film. At this point, the average film thickness on the surface is minimum, resulting in maximum heat flux. Immediately after bubble detachment, the retreated vapor from bubble stem takes some time to stabilize. Because of the presence of wake behind the bubble, the interface again necks slightly and generates a smaller peak as seen in the heat flux curve seen around time from 0.21s to 0.31s. This phenomenon repeats causing large peaks representing the bubble release and troughs as points of highest film thickness, (d) in Figure 21. The CFD simulated heat flux of this work is compared with corresponding estimations using Berenson and Klimenko correlations in Figure 21. It is found that the time weighted average (TWA) simulated wall heat flux is bounded by the correlations for the case of wall superheat of 103K.

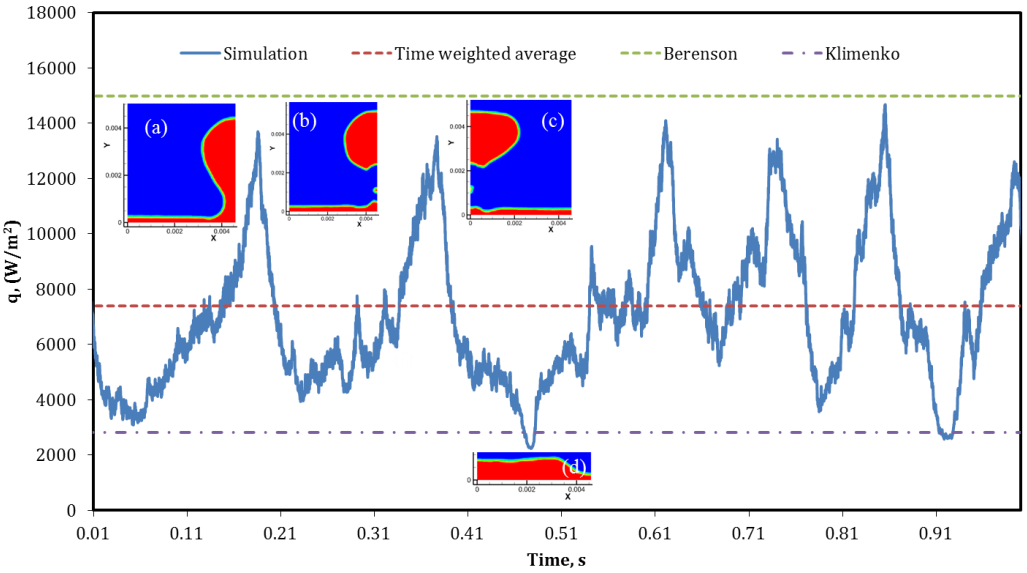

Figure 21: Trend of wall heat flux for LN_2 film boiling at ΔT = 103K.

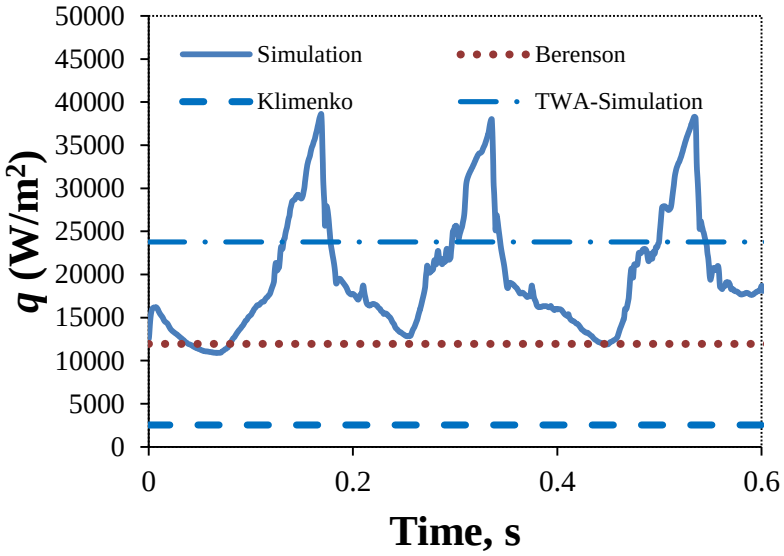

Figure 22: Surface heat flux for the film boiling of LNG at ΔT = 83 K.

Figure 22 depicts the trend of wall heat flux for LNG at a wall superheat of 83K. Similar to LN_2, the peaks represent the liberation of bubbles which follows a period of bubble growth. The average wall heat flux is obtained from the simulations is 23 kW/m^2 which is very high compared to the estimations of Klimenko and Berenson correlations.

3.4.6 Effect of wall superheats on bubble generation frequency and bubble diameter

Figure 18 depicts the effect of wall superheat on the bubble generation frequency during the film boiling of LN_2. For the wall superheat of 32K (Figure 18 (a-g)), the first bubble generates at 0.61 s and subsequent bubble generates at 1.19s, 1.76s, 2.24s, 2.53s and 3.17 s. As the wall superheat is increased to 73K (Figure 18 (h-m)), the bubble generation frequency increased. In this case, the first bubble was generated at 0.25 s and subsequent bubbles were generated at 0.55s, 0.72s, 1.0s, 1.25 s. Further increase of the wall superheat to 103K (Figure 18 (n-t)) depicts that the bubble generation frequency was also increased. In this case, the first bubbles were generated at 0.19s and subsequently the bubble generated at 0.37, 0.62, 0.83, 0.99 and 1.16s. Therefore, the increase of wall superheat increases the amount of vapor generation as the frequency of bubble generation is higher for greater wall superheat.

Fast Fourier Transform (FFT) is performed on 16384 data points of the simulated wall heat fluxes to determine the frequency of the bubble generation. Figure 23 depicts the results of the FFT analysis for the simulated case of LNG with a wall superheat of 43K. The dominant frequency of the bubble generation which corresponds to the x-axis

value (Figure 23) of the highest peak has been found to be 4.272 Hz. Similar analysis has been performed for LN_2, LNG, and LO_2 for all simulated wall superheat conditions.

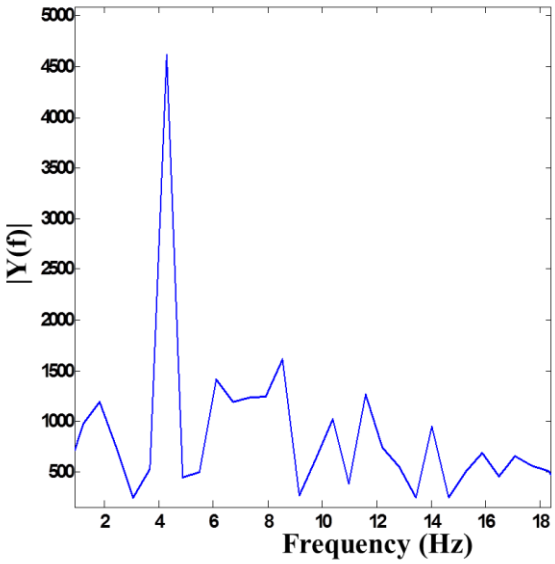

Figure 23: FFT of heat flux variation for LNG at a wall superheat of ΔT = 43 K.

Figure 24 shows bubble generation frequency for various simulated wall superheats. It is clear that the bubble formation rate is strongly dependent on the wall superheats. Within the simulated window, a model is fitted to predict the bubble generation frequency as a function of wall superheats, and it is found that, bubble frequency of LN_2 and LO_2 follow a power of 0.8, whereas LNG follows a power of 0.6. However, the co-efficient is higher for LNG as compared to LN_2 and LO_2 with an order of 3.4.

Figure 25 shows the dependency of bubble diameters, estimated at the time of departure from the vapor film. The behavior of LN_2 and LO_2 is similar. For a particular wall superheat, the bubble size is larger for LNG as compared to LN_2 and LO_2. A power model is fitted (shown on Figure 25) for LN_2, LO_2, and LNG to predict the bubble diameter as a function of wall superheats. For LNG the exponent of the model has found to be 0.25 and for LN_2, LO_2 its value are 0.28 and 0.23 respectively. The co-efficient for LNG is 2.5 times higher than that of LN_2.

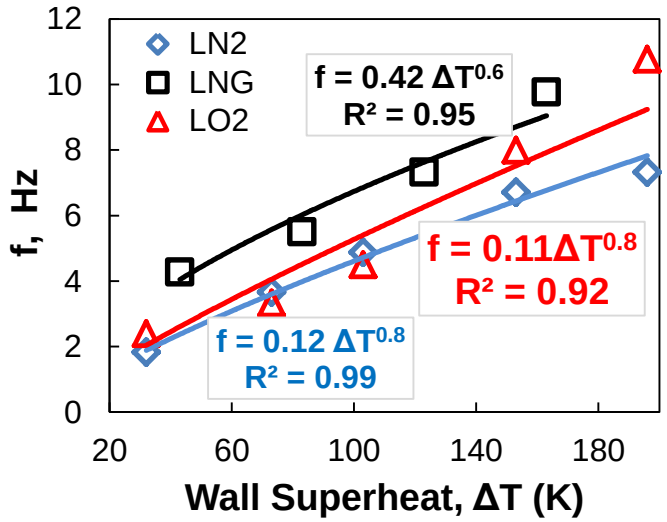

Figure 24: Bubble generation frequency of simulated film boiling cases at various wall superheats

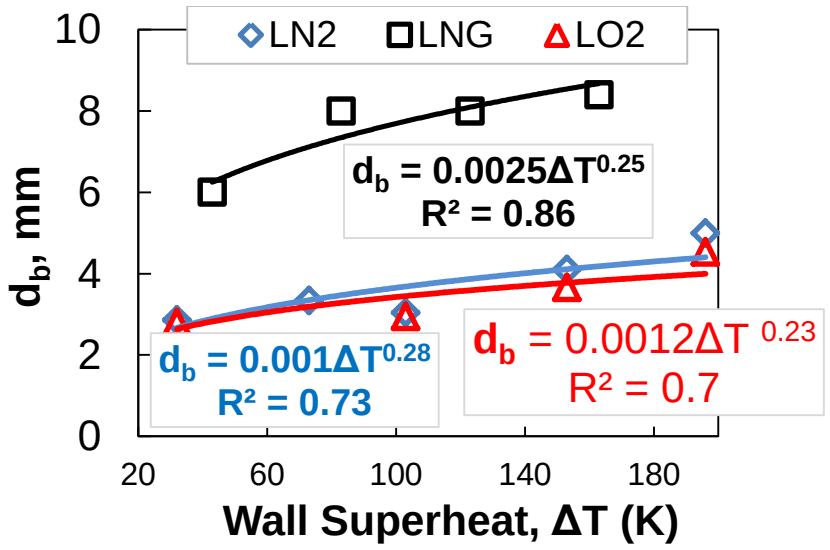

Figure 25: Bubble diameters of the simulated film boiling cases at various wall superheats

3.5 Proposed model to predict film boiling heat transfer

Figure 26 (a) compares the time weighted average (TWA) simulated heat fluxes with the heat fluxes estimated by using Berenson and Klimenko correlations, for a LN_2 film boiling system. Similarly, Figure 26 (b) compares that of for LNG film boiling system and Figure 26 (c) compares LO_2. For the case of LN_2, at a lower wall superheat, the simulated heat flux is closer to the estimation of Klimenko correlations and at higher wall superheat; the simulated heat flux is closer to estimation of Berenson correlations. The trend of the simulated results, depict that a logarithmic slope is much higher than the slope of both correlations. For the case of LNG, the TWA simulated heat fluxes are much higher than the estimations from Berenson and Klimenko correlations. It is important to mention that, the simulated results are not subjected to the assumptions such as constant film thickness, constant bubble diameters, absence of dynamic

movement of vapor and liquid, and usage of mean fluid properties. Thus, the simulated heat fluxes are more realistic than the aforementioned correlations.

Film boiling simulation for a single wall superheat takes approximately 800 minutes of computer time (Processor: 3.33GHz; RAM: 32 GB) to simulate two consecutive bubble detachments. Therefore, performing simulations for a large range of wall superheats might not be always possible when the time does not allow. Therefore, a first principle model based on simple heat balance is used to predict the wall heat flux for non-simulated wall superheats.

The proposed model is based on the heat balance as the amount of heat transferred from the wall is approximately equal or proportional to the heat taken by the bubbles that were formed in the film boiling regime. This can be mathematically expressed as Equation (7).

$$q \propto V_b \cdot f \cdot m \cdot \rho_v \cdot h_{fg} \tag{50}$$

For a two-dimensional CFD simulation, the above equation can be modified as follows:

$$q = C \cdot \frac{\pi d_b^2}{4} \cdot f \cdot m \cdot \rho_v \cdot h_{fg} \tag{51}$$

Where, it is assumed that C is a dimensionless constant equals to 1.0. For some cases *C* might not be 1.0. For an example, if the local physical property data such as ρ, μ and h_{fg} strongly varies with the temperature field, C = 1.0 may not be the proper representation. Furthermore, the bubble diameter d_b will also vary with the time of simulation and wall superheats, etc. The departure diameter of the first bubble for a

particular wall superheat might not be equal to that of the second bubble. The shape of the bubble can be different from spherical shape. Wake formation in the liquid and liquid depth may also affect the size and shape of the bubbles. Therefore, adjustment of the constant C might be needed to accurately predict the heat flux of the non-simulated cases.

The parameters in Equation (8) can be estimated using the simulation results. Fourier transformation is employed to determine the bubble generation frequency f from the transient wall heat flux for different wall superheat as depicted in Figure 23 and Figure 24. The departure diameter of the simulated bubble is considered to estimate the volume of the bubble (for 3D simulation) or area of the bubble (for 2D simulation). Therefore, by replacing the term, f and d_b using the fitted model as shown in Figure 24 and Figure 25 and replacing the parameter m, *i.e.,* number of nodes per unit area, with $1/L_c^2$, the proposed model for LN_2 and LNG are as follows:

$$q = 8.02 \times 10^{-9} \left(\frac{\rho_l - \rho_v}{\sigma}\right) \rho_v L_v \cdot \Delta T^{1.34} \qquad (\text{for } LN_2) \tag{52}$$

$$q = 1.7 \times 10^{-7} \left(\frac{\rho_l - \rho_v}{\sigma}\right) \rho_v L_v \cdot \Delta T^{1.1} \qquad (\text{for LNG}) \tag{53}$$

$$q = 6.73 \times 10^{-9} \left(\frac{\rho_l - \rho_v}{\sigma}\right) \rho_v L_v \cdot \Delta T^{1.26} \qquad (\text{for } LO_2) \tag{54}$$

Figure 26 depicts the fitness of the correlation for the proposed correlation for the two-dimensional simulations performed in this study. It is shown that first principle based correlation predicts the simulated heat fluxes to an excellent agreement.

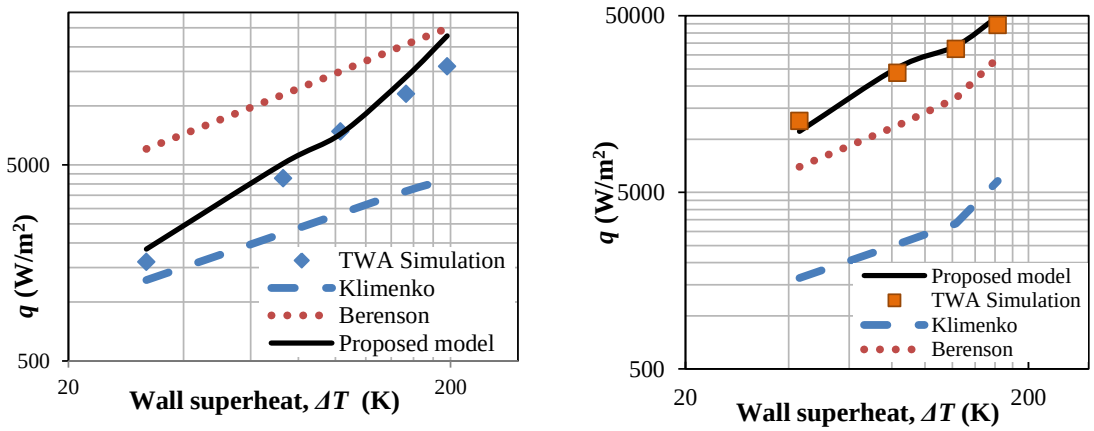

(a) LN_2 (b) LNG

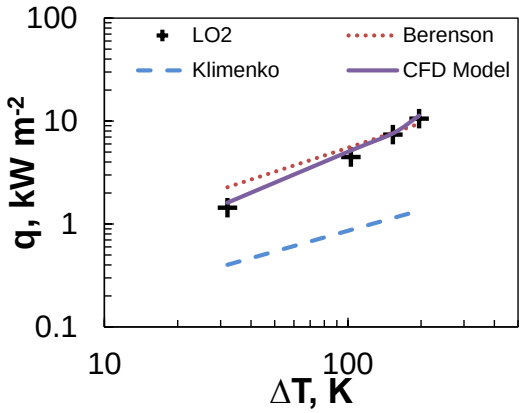

(c) LO_2

Figure 26: CFD-based model to predict heat flux of (a) LN_2 and (b) LNG (c) LO_2 film boiling

3.6 Conclusions

Inaccurate estimations of LNG vapor generations due to accidental spill may cause under estimation of consequence severity during the risk assessment of the facility. To provide more realistic estimation of the vapor dispersion source-term, *e.g.*, the vapor generation rate from a LNG pool, CFD simulations of cryogenic film boiling using volume of fluid (VOF) method in ANSYS Fluent have been studied. The simulations

provide insights into the physical processes of vapor formation that are useful for estimating the LNG vapor generation. The key conclusions of this study are:

(A) Film boiling of cryogenic liquids, *i.e.*, LN_2 LO_2, and LNG, are simulated by using Rayleigh-Taylor (R-T) approach in a commercial CFD environment (ANSYS Fluent). It is found that the dynamics of film thickness affects the wall heat flux and therefore the frequency of bubbles evolution and bubbles diameter. The bubble generation frequency is estimated from the transient wall heat flux by decomposing via FFT and the most dominant frequency is considered as the average bubble frequency for that particular wall superheat.

(B) At lower wall superheat conditions, the simulated heat flux of LN_2 is slightly greater than that estimated by using the Klimenko correlation and it is much lower than the estimates of Berenson correlation. It is important to note that the Klimenko correlation was validated for liquid nitrogen and while the Berenson correlation were validated using non-cryogenic liquid. At higher wall superheat, the simulated heat flux approach towards the estimation of Berenson. For the case of LO_2, the simulated wall heat flux is very close to the estimates of Berenson correlation.

(C) The simulated wall heat fluxes for LNG, as pure methane, were found to be significantly higher than the estimates of both the Klimenko and the Berenson correlations. As a result, the vapor generation estimation during the risk assessment would be under-predicted if such correlations were used. A

conservative approach to determine consequence severity of an accidental spill would be using the estimated heat flux via CFD simulations.

(D) The frequency of bubble generation is dependent on the degree of wall superheats. Increase of wall superheats increases the bubble generation rate, *i.e.*, bubbles form faster. It also enhances the instabilities in the vapor film. Thus, during the early stage an accidental spill of LNG, the vapor generation rate will be higher in comparison to the later stages of spill.

(E) It is observed that the bubble release locations depend on the dynamics of the vapor film movement, the motion of the liquid and the movement of the liquid surface when the pool depth is not significant. As a result, alternating nature of bubble release locations, from the node point to the anti-node point in the consecutive bubble cycles, will be an unrealistic assumption. Thus, use of empirical expressions, which assume alternating nature of bubble generation from the node and anti-node point, might be unsuitable for cryogenic vaporization source-term estimation.

(F) Finally, based on the trends of bubble generation frequency and bubble diameters, a first principle model is applied for modeling heat flux during the film boiling regime. The proposed model can be used along with in 1-D standard heat transfer model to determine the liquid phase resistance, and thus, enabling more accurate estimation of vapor formation source-term.

4. EXPERIMENTAL VALIDATION OF THE CFD BASED FILM BOILING STUDY[2]

Section 3 described a CFD-based film boiling model to simulate heat flux in the film boiling regime. Despite of the fact that, the boiling model is considering all aspects of the physical processes, NFPA 59A [4] requires validation of the model using experimental data. This section presents the validation of the CFD-based model proposed in section 3.

Industrial standards (NFPA 59A [4]) specifies the use of dikes or impoundment area around the LNG containers to prevent uncontrolled dispersion of LNG and its vapor. The most common dikes floor material is concrete.

Experimental study suggests that conductive heat transfer from the solid substrate to the liquid pool is the main mode of heat transfer during pool vaporization. Some argue whether conductive heat transfer is the dominant mode throughout the pool vaporization period [18]. Other studies suggest, convection and solar radiation can be accounted for less 5% of the total mass vaporization [10], [104], [105]. Despite, it is well accepted that conduction heat transfer from the substrate is the major heat transfer source in cryogenic pool vaporization, at least in the beginning of the spill, if not during entire vaporization period [24].

---

[2] This Section contains material that has been published in the proceedings of the following symposium. Monir Ahammad, Syed Quraishy, Tomasz Olewski, and Luc Vechot, "Experimental and theoretical study of vaporization source-term due to conduction heat transfer from concrete substrate.", in the proceedings of *May Kay O'Connor Process Safety Center International Symposium, College Station, Texas, 2016.* No permission is needed as the author holds the copyright of the presented material.

4.1 Introduction to the spill experiments: A literature review

A laboratory scale analysis of LN_2 vaporization due to different heat transfer mechanisms were conducted by Vechot *et al* [18] in a Dewar flask. They have reported that convective and radiative heat transfer plays a significant role in the vaporization of LN_2 particularly in the later stages of pool boiling. However, the limitation of their experiment is that in an actual spill scenario, the cryogenic liquid (*e.g.*, LNG) may not be contained within insulated walls and floor. Rather the pool of liquid will boil due to the conductive heat transfer from the dike walls and floor along with other sources of heat such as convective and radiative heats. Another limitation of this study was a small amount of cryogenic liquid (~2 kg) was allowed to vaporize. Therefore, the results of this study may not be accurate, when extrapolated for a full-scale industrial spill. Nevertheless it is worth mentioning that an industrial scale spill experiment is very expensive. Other small-scale studies of LN_2 vaporization on water and ice substrates were addressed by Gopalaswami *et al.*[106], [107].

An early review of cryogenic spill data were conducted by Prince [108] and a recent one by Thyer [109]. Thyer has reviewed 39 cryogenic spill experiments reported in the literature. His analysis showed that seven of these experiments were too lacking in capturing detailed information to be usable. A concrete substrate was used in 7 among the 32 hazardous material spill studies. Three among these seven studies were focused on hazardous materials such as chlorine, hydrogen, oxygen, and water. A deeper analysis of the remaining 4 studies revealed the type of material hazardous material used was pure methane but referred to as LNG. This might result in some prediction error as

literature suggests that multicomponent mixtures may have a significant influence in vaporization [110]. Apart from that, three studied vaporization on insulated concrete floors. The remaining one study did not characterize the substrate concrete. Thus, it can be concluded that the vaporization characteristics of pure and mixture cryogens (*e.g.*, LN_2, LO_2, LNG) on actual dike floor material (*i.e.*, concrete) is lacking in the literature.

Luketa-Hanlin [111] reviewed large-scale LNG spill experiments over all substrates until 2006. Despite a large number of LNG spill tests performed, few of them address the importance of vaporization rate. Most of the studies focused on the heat flux from LNG fire, dispersion of the LNG vapor cloud and parameters affecting the dispersion, rapid phase transition (RPT). Table 3 summarizes the key spill experiments that address the pool boiling aspects of the LNG spill. It is clear from the Table 3 that experimental data on the vaporization source-term of LNG spills on concrete substrate is non-existent.

4.2 Experimental study of vaporization source-term on concrete substrate

A series of experiments were performed in a wind tunnel of Qatar Petroleum's fire station -2 at Ras Laffan Industrial City, Qatar. Experiments were performed by Syed Quraishy of Texas A&M University at Qatar, in the period of April to May 2014. First day included the spill of liquid nitrogen (LN_2) only and was performed on April 22, 2014. Second experiment included the spill of liquid nitrogen and liquid oxygen mixture (LN_2-LO_2) and was performed on April 28, 2014 and the third experiment included the spill of liquid oxygen (LO_2) only and was performed on May 13, 2014. The raw

experimental data was provided to the author to analyze and validate the CFD modeling predictions described in the previous section.

Table 3: LNG spill experiments and its key aspects

Experiment	Substrate type	Spilled volume (m^3)	Pool radius, m	Heat/ Mass flux, Kg $m^{-2}s^{-1}$
Boe (Lab) [112]	water	6 x 10^{-4}	0.1	0.086 (film boiling)
Drake et al (Lab) [113]	Insulated concrete/ water	-	-	Time varying
Boyle and Kneebone [30]	water	0.023 - 0.093 (pond)	1.97 – 3.63	0.029
Burgess et al (Bureau of Mines) [114]	water	0.0055-0.36 (pond)	0.75 – 6.06	0.181
Feldbauer et al (ESSO) [115]	water	0.73 – 10.2 (Matagorda bay)	7-14	0.195
Maplin sands [116]	Water/sand	5 – 20 (inlet surrounded by 300 m dike)	~ 10	0.085
Koopman et al (Avonet LLNL) [117]	water	4.2 – 4.52 (pond)	6.82 – 7.22	0.12

This study focuses on a medium-scale field experiment (5-50 kg) on concrete substrate. The investigation findings are expected to improve the understanding of an actual spill scenario. Literature suggests that influence of multi-component mixtures can be significant for other cryogenic liquids such as LNG and LPG [110]. Therefore, to understand the influence of multi-component, a mixture of initial composition of 80% LN_2 and 20% LO_2 is also studied to capture the effect of preferential boiling during vaporization of mixtures. Thus, this study is expected to contribute to generating

experimental knowledge of cryogenic vaporization source-term and will help the existing models in validating their assumptions. In this study, the liquid mass vaporization, temperature and heat flux profiles inside the substrates were investigated. Thermo-physical characteristics of concrete substrate were determined at different temperatures.

4.2.1 Schematic diagram of the experimental setup

Figure 27 presents a schematic diagram of the experimental setup. Cryogenic liquid (*i.e.*, LN_2, LO_2 and an initial mixture of 80% LN_2 and 20% LO_2) were poured in a box of concrete substrate. A 30-feet long connecting hose with a vapor and liquid separator at the open end is used to transfer the liquid from the cryogenic liquid tank to the experimental setup. To subside the vaporization of cryogens inside the liquid hose, it was insulated and was protected from the solar radiation. Steel plates were used to construct the liquid holding box of (500 mm x 500 mm x 300 mm) on the top of the concrete substrate. The dimension of the concrete substrate was 500 mm x 500 mm x 650 mm. The area of the substrate face in contact with the liquid was 500 mm x 500 mm. The set-up was insulated at the outside using 6-inch polystyrene foams to reduce the heat transfer due to convective heating. The top of the liquid holding tank was also covered with insulating polystyrene to reduce the atmospheric convective heat transfer. Eleven thermocouples of type N with sensitivity of ±0.01°C and two heat flux measuring sensor plates of Hukseflux, HF-01 type, with a sensitivity of ± 1084 $\mu V/W/m^2$, were placed in 4 layers inside the concrete substrate. The exact locations of the thermocouples

(TC) and heat flux sensors (HF) were given in Table 4. TC-110, TC-111, TC-113, TC-115 thermocouples and HF-284 heat flux sensor were placed in the 1st layer beneath the boiling liquid at an approximate depth of 25 mm. In the 2nd layer, TC-108, TC-114, TC-106 thermocouples and HF-285 heat flux sensor were placed at an approximate depth of 110 mm. In the 3rd layer, at a depth of 220 mm, TC-107, and TC-109 thermocouples were placed. Finally, in the 4th layer, at the depth of 620 mm, TC-112, TC-116 thermocouples were placed. It should be noted that the heat flux plate sensors measures both the temperature and the heat flux at its location. The overall setup was placed on a balance with a sensitivity of ±60gm. This whole instrumented set-up was connected to a data acquisition system.

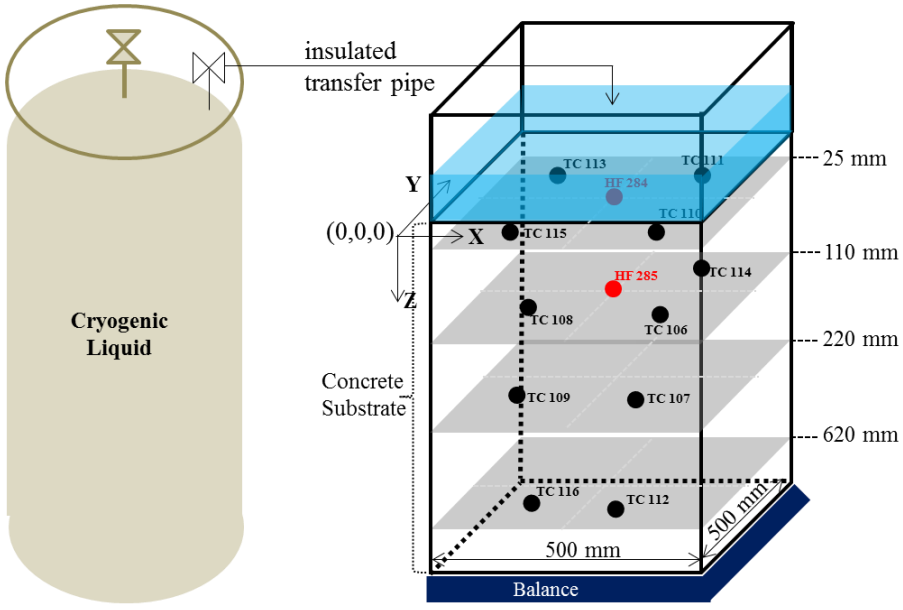

Figure 27: Schematic diagram of the experimental setup. Black dots represent the location of thermocouples inside concrete substrates and heat flux sensors location was indicated by the red dots.

Table 4: Coordinates of the thermocouple and heat flux sensors' locations inside the concrete substrate

Layer 1				Layer 2			
	X (mm)	Y(mm)	Z(mm)		X (mm)	Y(mm)	Z(mm)
TC-110	248.8	117.5	28.5	**TC-106**	264	120.5	111
TC-111	320.5	273.5	24	**TC-108**	132.5	122.5	111
TC-113	72.3	278.8	33	**TC-114**	312.3	274	110.5
TC-115	132.8	121.8	25	**HF-T-285**	193	168.5	96.5
HF-T-285	197.5	168.5	28.5	**HF-X-285**	193	168.5	96.5
HF-X-284	197.5	168.5	28.5				
Layer 3				**Layer 4**			
	X (mm)	Y(mm)	Z(mm)		X (mm)	Y(mm)	Z(mm)
TC-107	265	115.3	226.5	**TC-112**	258.8	119.3	622
TC-109	128.8	119.5	220	**TC-116**	120	122	621.5

Figure 28 shows the photographs of the experimental setup. Cryogenic liquids were transferred from the liquid tank (Figure 28 (a)) by opening air circulation to the heating coil. Pressure increased inside the tank due to the vaporization of the cryogenic liquids which eventually drove the liquid to flow through a liquid transfer valve via the 30 feet insulated hose. The vapor liquid separator (Figure 28 (b)) at the end of the hose pipe slowed down the speed of two phase flow. Thus results in the vapor to flow upward direction without touching the concrete substrate. The whole set-up was placed on a balance as shown in (Figure 28 (d)).

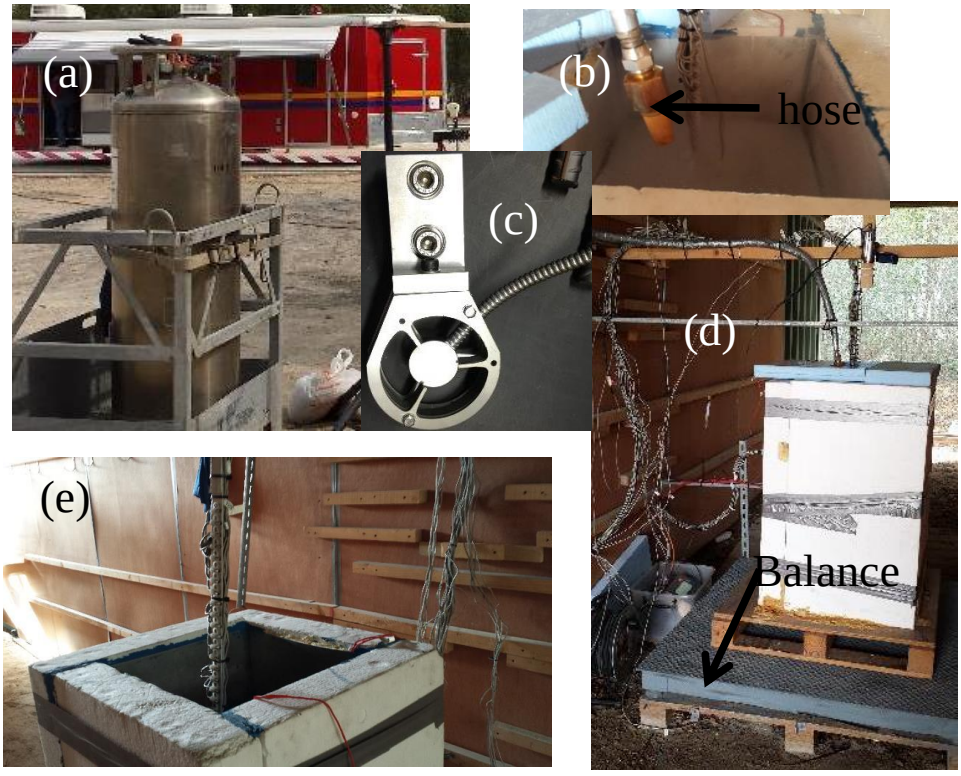

Figure 28: Experimental set-up. (a) Cryogenic liquid tank (b) Vapor – liquid separator (c) Heat flux sensor (d) insulated set-up (e) insulation thickness and level measuring thermocouples bar

4.2.2 Thermo-physical properties of the concrete substrate

The substrate material of this experimental set-up was same to the industrial grade concrete that was used in the construction of Testing Prop-5 at Ras Laffan Emergency Safety College in Qatar. The thermo-physical properties of the concrete composites were experimentally determined at NETZSCH Instruments Testing Laboratory, Burlington, MA, for various temperatures. Standard procedures (ASTM C 177-10, steady-state heat flux measurements and thermal transmission properties by

means of guarded hot plate apparatus, utilizing a Holometrix Model) were followed to measure the thermal conductivity. Two concrete slabs, of same composition as the experimental setup of dimensions 305 mm by 305 mm square with a thickness of 43 mm were used to test for thermal conductivity. The densities of the used samples were determined as 2335 kg/m^3. Figure 29 shows the dependency of thermal conductivity on the mean temperature between the top and bottom surfaces. The reported results have uncertainty of lower than 7%. It is observed that conductivity increases linearly between -161°C to -66°C. At higher temperature range, from -41°C to 50°C, the rate of increase is smaller than the lower temperature range. Between -66°C and -41°C, it was found that the rate of change of conductivity with mean temperature is negative.

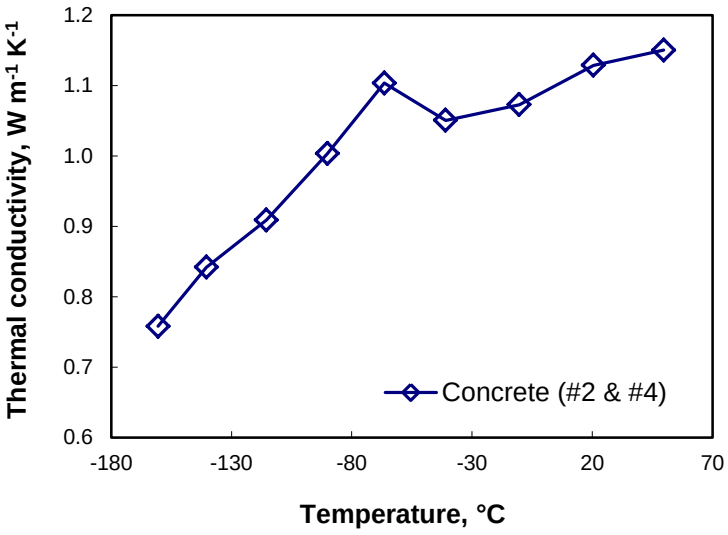

Figure 29: Thermal conductivity of the concrete as function of mean temperature

Furthermore, four small concrete samples, (*i.e.*, sample 1 to 4), of 12.61 mg, 10.02 mg, 10.02 mg, and 10.54 mg were tested using a Differential Scanning Calorimeter (DSC) to determine the specific heat capacity (*Cp*). Figure 30 depicts the *Cp* as a function of temperature in the range of -160°C to 50°C. It is clear that the specific heat increases linearly with the increase of temperature. However, a variability of 0.046 J/gK among the four samples was observed at -160°C. At higher temperature, *Cp* has varied more comparing to lower temperatures. At 50°C, the *Cp* variability among the four tested samples was reported as 0.122 J/g.K.

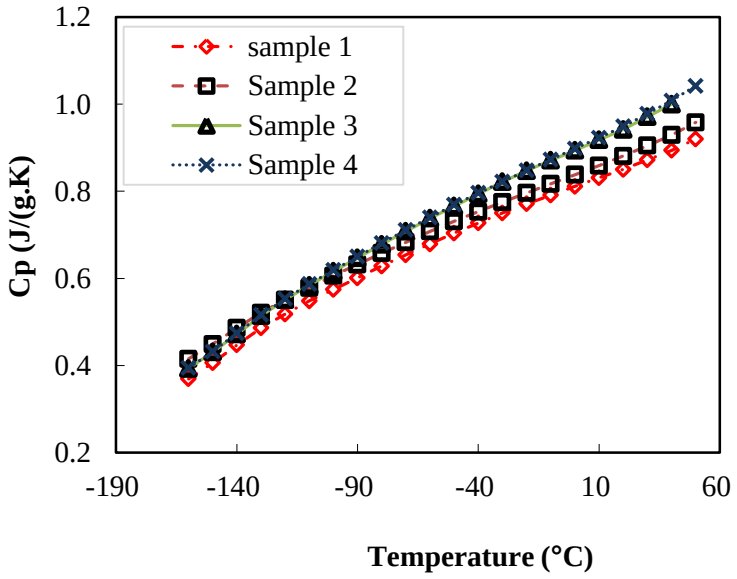

Figure 30: Specific heat capacity of powdered concrete samples using DSC

4.2.3 Experimental procedure

Before starting the filling up of liquid into the concrete vaporization chamber, liquid cylinder tank is connected to a hose and the data acquisition system for the instrumented box and balance were started. The pressure build-up valve was opened to build pressure inside the liquid cylinder. Once the desired pressure was reached in the liquid tank, the liquid transfer valve was opened to transfer the liquid from the liquid tank to the vaporization chamber. In the beginning, cryogenic vapor comes out of the liquid carrying hose due to the vaporization inside the hose. After some time, liquid started coming out of the hose. Once the liquid touched the surface of the concrete, the reading in the balance started changing. The liquid flow to the vaporization chamber was stopped well before the overflow. Relatively long time was allowed to vaporize the liquid by taking conductive heat from the concrete substrate before refilling the vaporization chamber. After a significant mass of the liquid vaporized, the chamber was replenished. The procedure was repeated 4 times for LN_2, 2 times for LO_2 and 6 times for mixtures.

4.2.4 Results and discussions

4.2.4.1 Liquid mass vaporization

Figure 31 shows the mass of liquid in the vaporization chamber during the course of experiments. From Figure 31, at the beginning all three curves for LN_2, LO_2 and

mixture filling curve show a concave vaporization curve due to the mass loss due to conductive heat transfer from the concrete. For the LN_2 experiment, the second refilling of the vaporization chamber was started at 1421 second when the chamber was holding about 5 kg of liquid and the refilling ended at 1627 second at a final liquid mass of 10.2 kg. The third re-filling started at 2655 second while the chamber was holding 3.2 kg of liquid and ended at 2909 second at 11.2 kg of liquid mass. Finally, the fourth re-filling started at 4911 second while it was holding 2.6 kg of liquid pool and ended at 5123 second at the liquid mass of 11.4 kg.

For LO_2, the second re-filling started at 1781 seconds while the chamber was holding 1.2 kg of liquid and ended at 1890 second while there were 14.6 kg of liquids. The third re-filling started at 4900 seconds while the chamber was holding 1.8 kg of LO_2 and ended at 5000 second and 13.9 kg of liquid. For the mixture of LN_2 and LO_2 of an initial composition of 80% LN_2 and 20% LO_2 in the liquid cylinder tank, the second re-filling started at 1810 second while the tank were holding 2.6 kg of liquid and ended at 1870 second with 12.5 kg of liquid. The third re-filling was started 3688 second with 2.9 kg of liquid mass and ended at 3805 second with 13.4 kg of liquid. The balance used to measure the mass of the liquid has an uncertainty of ±60gm. Therefore, the maximum amount of measurement uncertainty in the data presented in Figure 31 is less than 4%.

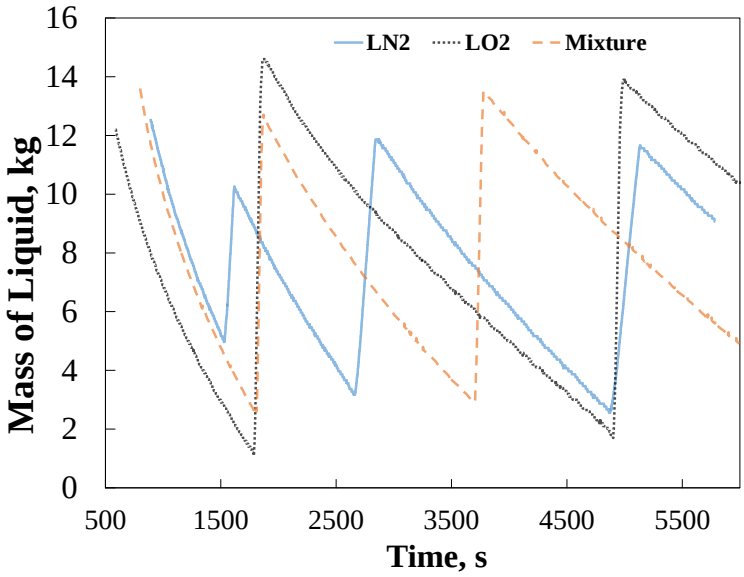

Figure 31: Mass of the liquid pool

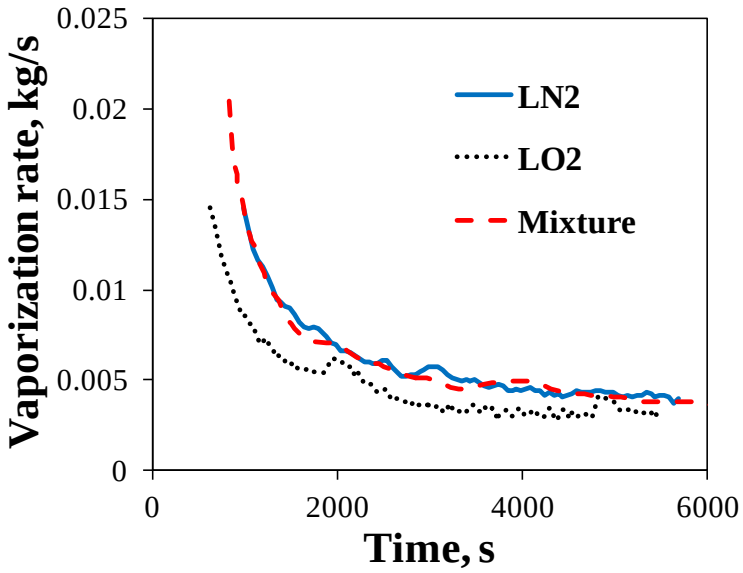

Figure 32: Mass vaporization rate of cryogenic liquids after a spill on a concrete surface

Figure 32 presents the rate of mass vaporization when cryogens were spilled in the vaporization chamber for the spill cycles presented in Figure 31. To calculate the vaporization rate, the balance data during the re-filling periods were discarded due to the fact that the estimated vaporization rate will not represent vaporization due to heat conduction only. It is clear from the Figure, the vaporization rate decreases rapidly at the beginning of the spill and tends to cease at the end of the spill. At time beginning, the rate of vaporization of LN_2, LO_2 and mixture were 0.016±4%, 0.015±4% and 0.022±4% kg/s respectively. However, it would be inaccurate to draw any conclusions from this observation due to the fact that LN_2, LO_2 and mixture undergone different duration of first filling time.

From Figure 32, the vaporization rate of LN_2 at the beginning is 0.016 kg/s. Though the vaporization rate of mixture is higher (0.022 kg/s) than that of LN_2, with time the mixture appears to follow the trend of the LN_2. Therefore, it can be concluded that the effect of mixture on the mass vaporization rate is very significant.

4.2.4.2 Temperature and heat flux profiles inside concrete substrate during LN_2 vaporization

Figure 33 depicts the transient temperature profiles inside the concrete substrate at 4 different depth layers. The initial temperature of the concrete substrate was 27.8°C before the start of spill. From Figure 33(a), it is clear that the temperature started changing almost immediately at the thermocouples in the first layer of depth. However, from Figure 33(b), the readings of thermocouples started changing after 720 seconds of the first layer. Similarly, after 2200 seconds of spill, the temperatures of the fourth layer started changing. And for the fourth layer, it is clear from Figure 33(d) that the temperature remained same as the initial temperature of the concrete substrate. From layer 1, the rate of temperature decreases in the thermocouples which are closer to the liquid-substrate interface (*i.e.* TC-111, TC-115) are higher than the thermocouples lies in deeper locations. Similar observations were found for the layer 2 thermocouples. Comparing the rate of change of temperatures at 5000s, layer 1 thermocouples reached to an almost steady-state condition whereas layer 2 thermocouples were changing. These observations were consistent with the 1-D heat transfer model of semi-infinite solid materials and also indicate that the experimental results have a good reproducibility.

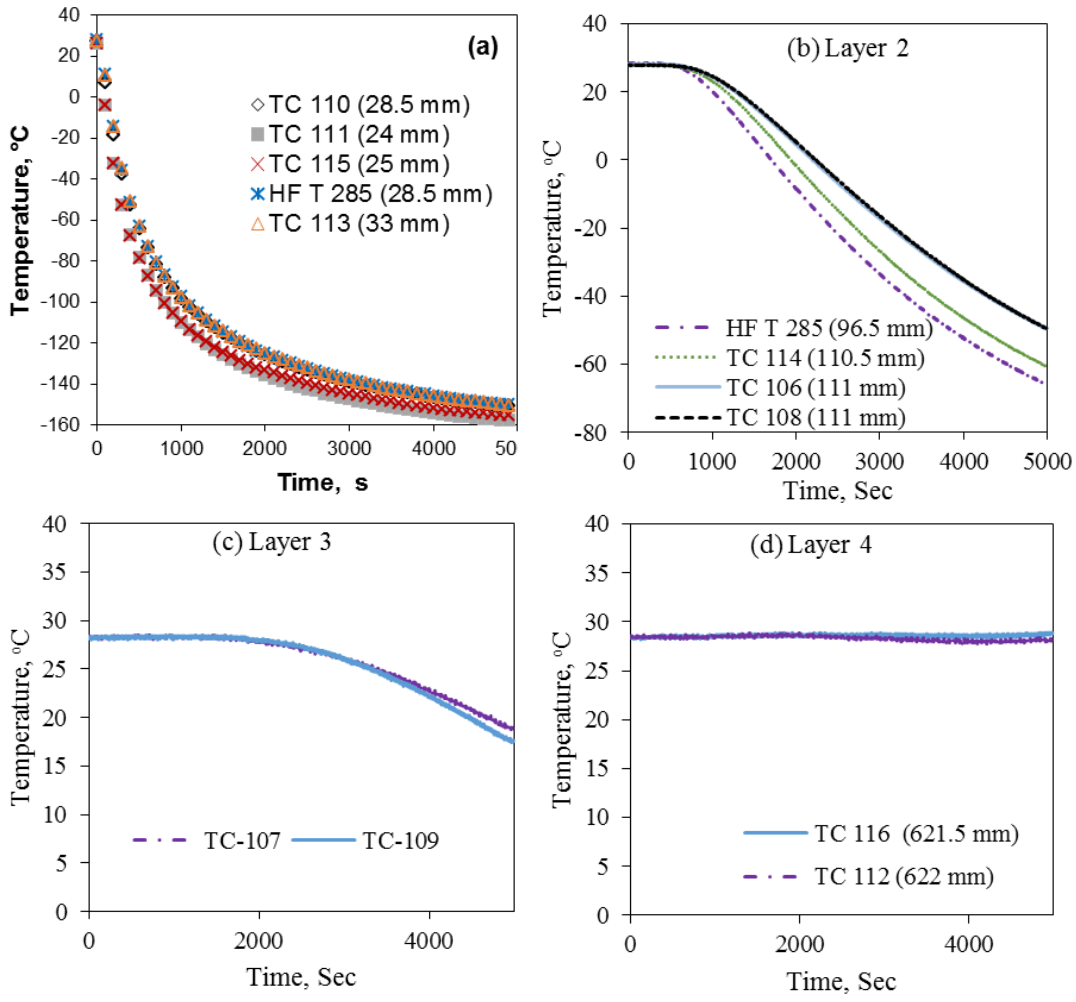

Figure 33: Temperature profile inside the concrete slab during the spill of liquid nitrogen

Figure 34 depicts the heat flux monitored at the depths of 28.5 mm (HF-X-284) and 96.5 mm (HF-X-285) inside the concrete substrate. For HF-X-284, the heat flux increased sharply and reached a maximum point and then decreases monotonically. The physical explanation of this trend is as follows. If you consider a thin slice of concrete

material at the depth of the heat flux sensors, the temperature above the slice and bottom of the slice were same initially. Therefore, no heat flux was observed at the beginning. As the temperature at the top of the slice decreases due to vaporization of LN_2, a temperature gradient was created within the thin slice. The temperature gradient increases sharply causing sharp increase of heat flux. While draining sensible heat stored within the thin slice, to vaporize the boiling liquid, results in decreasing the temperature gradient. Therefore, the heat flux decreases monotonically as the temperature gradient within the slice is decreasing. For the case HF-X-285, similar explanation can be given. However, the temperature gradient of a thin slice at the depth of heat flux sensor location was 0 for duration of 480 seconds. It took about 4,000 seconds to increase the temperature gradient. Therefore, an increasing heat flux was observed at this sensor. At the end of 4,000 seconds, the rate of heat flux for HF-X-285 is the same as the rate of heat flux for HF-X-284, indicating that the heat transfer rate is reaching steady-state condition. Change in the observed heat fluxes from HF-X-284 and HF-X-285 sensors were compared with the estimates due to the mass vaporization as shown in Figure 32. The HF-X-284 data is not comparable to the heat flux estimation from mass vaporization because HF-X-284 does not lie at the liquid-solid interface. In addition, convective heat transfer might have small contribution in the heat flux estimates from mass vaporization. Despite that heat flux from HF-X-284 agrees well with the heat flux estimation from mass vaporization data; indicating the main contributor of heat of vaporization is conduction from the substrate. Finally, the highest heat flux observed during early and steady-state conditions of LN_2 spill were 12.4 kW/m^2 and 3.7 kW/m^2.

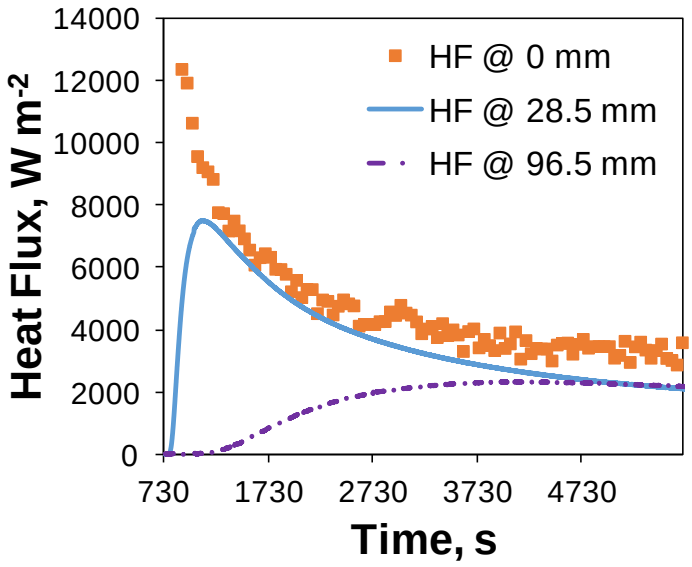

Figure 34: Heat flux to the liquid nitrogen pool

4.2.4.3 Temperature and heat flux profiles inside concrete substrate during LO_2 vaporization

Figure 35 illustrates the temperature and heat flux profiles during the LO_2 vaporization test on the concrete substrate. The initial temperature of the concrete substrate was 32°C. It was observed that the temperature profile of the layer 3 and 4 remained constant. However, compared to LN_2 data, no temperature change was observed in layer 3 sensors. It can be accounted to higher initial temperature (32°C) than LN_2 (27.8°C). Thus more sensible heat was stored per unit volume of concrete during the LO_2 test. Layer 1 temperature profiles show that thermocouples closer to the liquid-solid interface underwent larger temperature change than those were deeper in the concrete. From Figure 35(b), the temperature of the layer 2 thermocouples started

changing at 436 seconds. Also, it validates the fact that the change in temperature is higher for thermocouples closer to the surface than the thermocouples placed deeper.

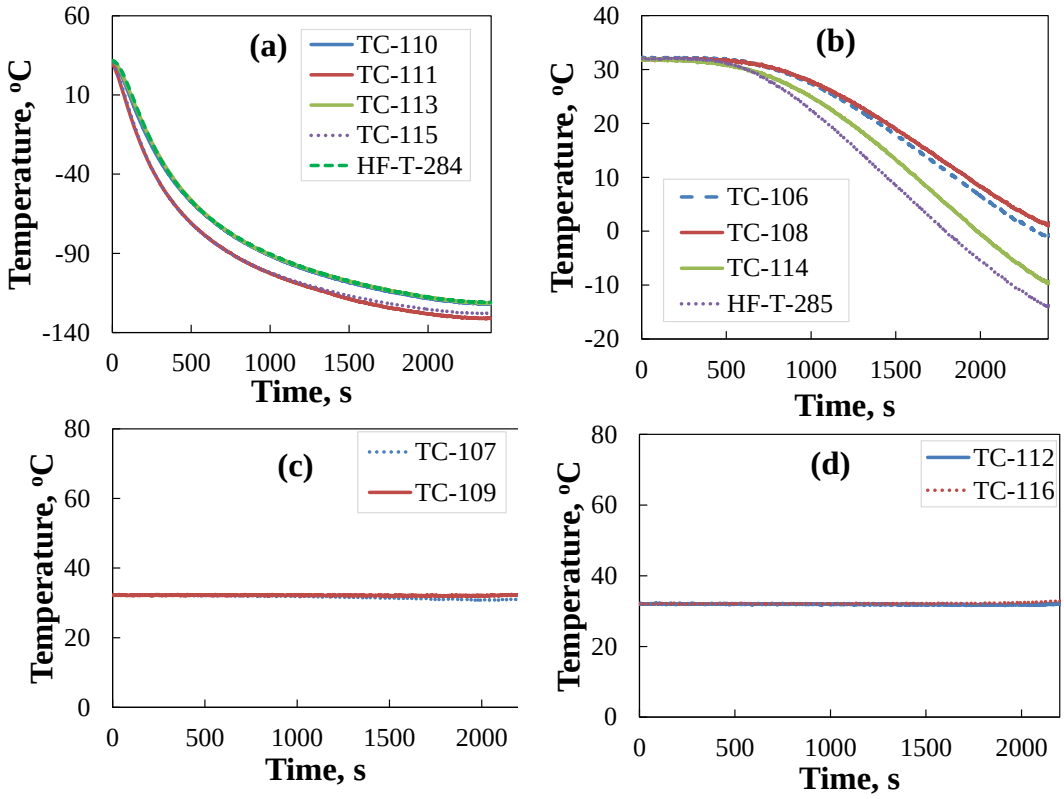

Figure 35: Temperature profile inside concrete slab during the spill of liquid oxygen.

Figure 36 shows the measured heat flux using heat flux sensors and estimates based on Figure 32 mass vaporization rates. Unlike the observations of LN_2, after the sensor data reaches the estimates, it decreases monotonically, while the estimate decreases at a higher rate. However, about time 1480 seconds, the estimated heat flux

jumps over the HF-X-284 and thereafter both the sensor and estimates were in very good agreement. The phenomena of HF-X-284 sensor readings and estimates discrepancy can be explained by the mode of boiling phase change. Once the liquid boils in the film boiling regime, the rate of heat flux decreases rapidly as the vapor film between the boiling liquid and the solid substrates has low thermal conductivity. However, when the film breaks, liquid come in contact with the solid, thus the thermal resistance drops significantly and this causes an increase of heat flux. Finally, the highest heat fluxes observed during the LO_2 vaporization during early and steady-state conditions were 12.9 kW/m^2 and 2.96 kW/m^2.

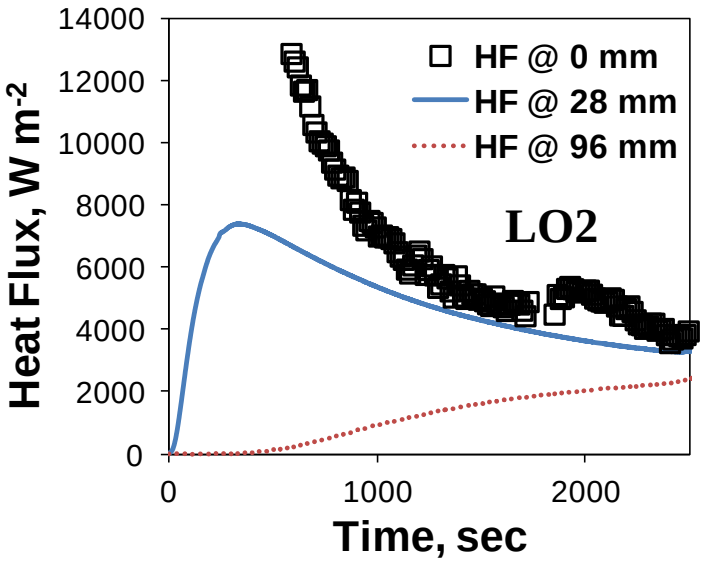

Figure 36: Conductive heat flux provided to liquid oxygen pool

4.2.4.4 Temperature and heat flux profiles inside concrete substrate during mixture vaporization

An initial mixture of 80% liquid nitrogen (LN_2) and 20% liquid oxygen (LO_2) was poured in the concrete vaporization chamber. Figure 37 presents the temperature profiles inside concrete substrate at 4 different layers. The duration of the test for mixture spill was 5.7 hours, whereas LN_2 and LO_2 were much shorter in comparison. Therefore changes in temperatures were observed in all layers of thermocouples. The initial temperature of the concrete substrate was 30.3°C. At 1140 seconds, the temperature of layer 2 thermocouples started changing from the initial point. In layer 3, temperature started changing at about 2180 seconds. The temperature of the layer 4 remained almost constant throughout the test. In Figure 37(a), a wavy pattern of temperature profiles were observed for the first layer of thermocouples at 3339, 6000, 9922 and14397 seconds. The rate of temperature change in the first layer of thermocouples suddenly increased and then started following the decreasing trend at these time instants. This phenomenon is noticeable after the 3^{rd}, 4^{th}, 5^{th} and the 6^{th} refill of the mixture liquid in the vaporization chamber. However, the 5^{th} and the 6^{th} refills were not shown in Figure 31. A sudden rise in heat transfer rate at these time instants were also observed in Figure 38. This observation can be accounted due to preferential boiling of LN_2 over LO_2 during mixture vaporization. When mixture was allowed to boil in the vaporization chamber, initially LN_2 was boiling at a higher rate than the LO_2 due to its lower boiling point. As a result, just before the refill of the mixture, the concentration of LO_2 in the remaining liquid were believed to much higher than 20% of

initial concentration. Once the tank was refilled with another batch of mixture liquid, the concentration of LN_2 increased. As a result, a sudden increase of heat flux which was reflected across the temperature gradient across the layer 1. At the beginning of the test, the rates of temperature and heat flux decrease were much higher to capture the subtle change due to preferential boiling. Therefore, no change in the temperature and HF-X-284 heat flux sensors data were captured in the first layer of instruments.

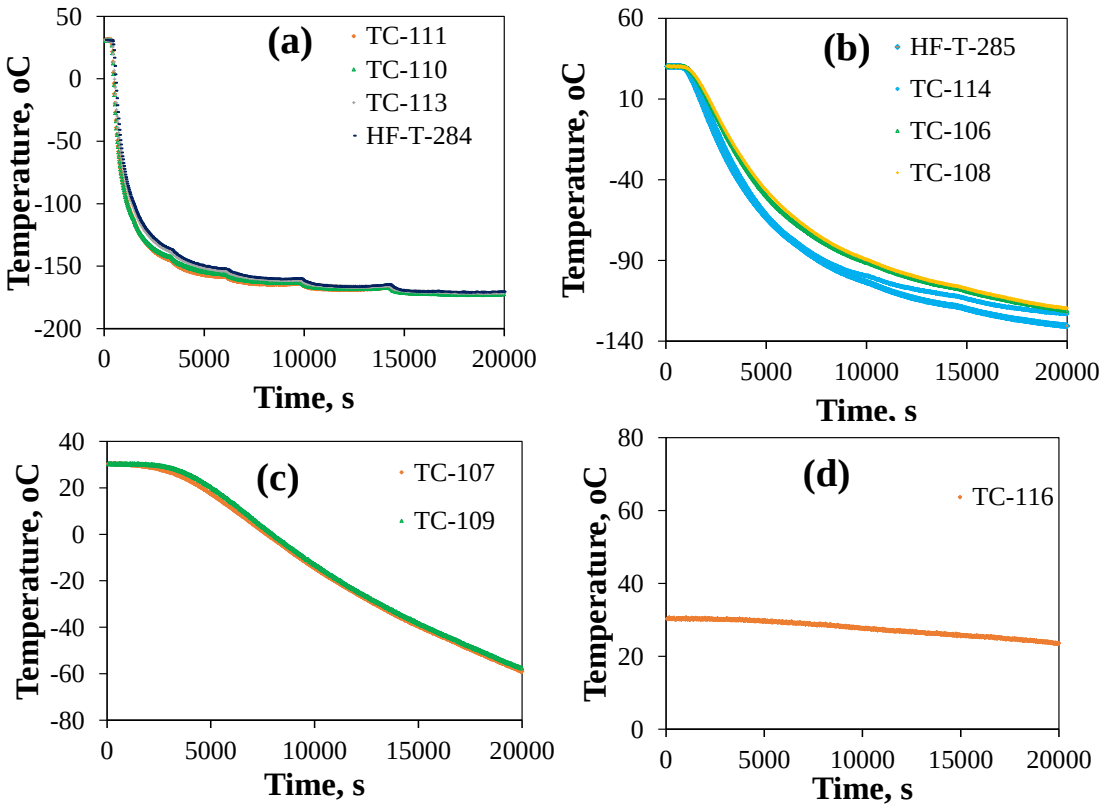

Figure 37: Temperature profile inside concrete slab during the spill of liquid nitrogen (80%) and liquid oxygen (20%) mixture.

From Figure 38, at 1100 second, there is a change in the trend of HF-X-284 reading. At the time instants of 3,339 second, the change in heat flux due to preferential boiling is much prominent and caused a 3% increase in heat flux after the refill. Subsequent observations at 6095, 9785 and 14258 seconds, the heat flux has increased by 6%, 11% and 15% after the refill of the mixture liquid to the vaporization tank. It is also shown in Figure 38 that heat fluxes from HF-X-285 overshoot that of HF-X-284 at 4294 seconds. At that instant, the temperature gradient across a thin slice of layer 1 has dropped lower than the temperature gradient across another thin slice of layer 2.

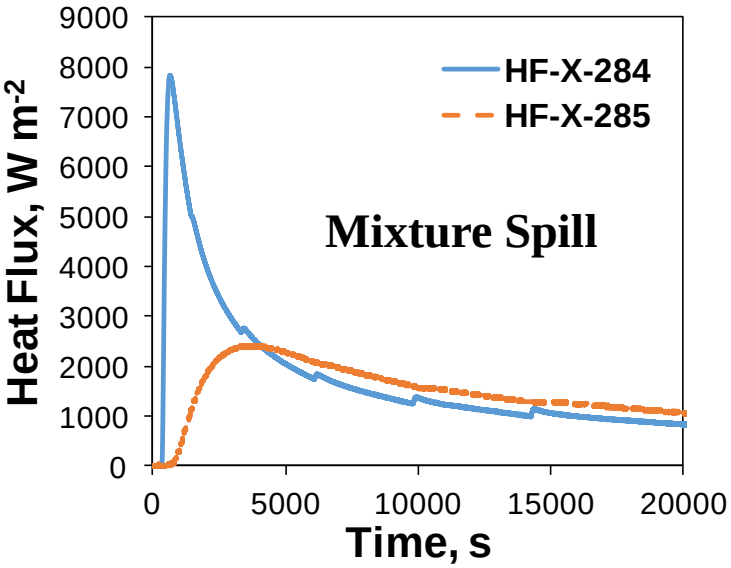

Figure 38: Heat flux inside the concrete at the depth of 28.5 mm and 96.5 mm.

4.2.4.5 Effect of mixture properties on the vaporization of cryogenic liquids

Figure 39 illustrates the temperature profiles of a first layer thermocouple (TC-111), a second layer thermocouple (HF-T-285). It is observed from the slopes of Figure 39(a) and (b), for mixture, in the beginning, the rate of temperature change follows that of LN_2 and at the later stage it follows the trend of LO_2. For the layer 2, though the mixture heat flux is slightly higher at the beginning, it starts following the LN_2 trend after 1000 seconds.

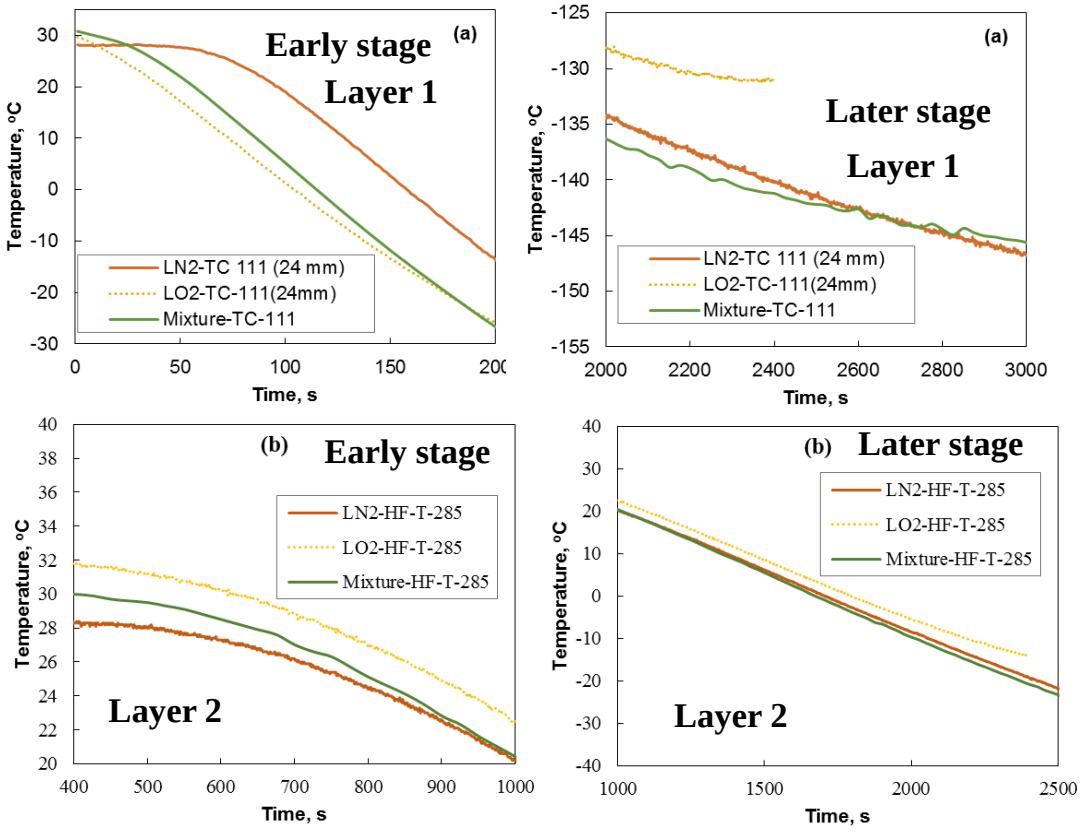

Figure 39: Effect of mixture on the temperature profiles in layer 1 and layer 2

From Figure 40 the variation among the heat flux profiles is due to the 13K wall superheat, the difference in LN_2 and LO_2 boiling points. Different rise time was observed for different material in HF-X-284 heat flux profiles. It is also seen that the slope of mixture heat flux varied from the slope of LN_2 and LO_2. In the early stage, the slope follows the trend of LN_2 and in the later stage that of LO_2.

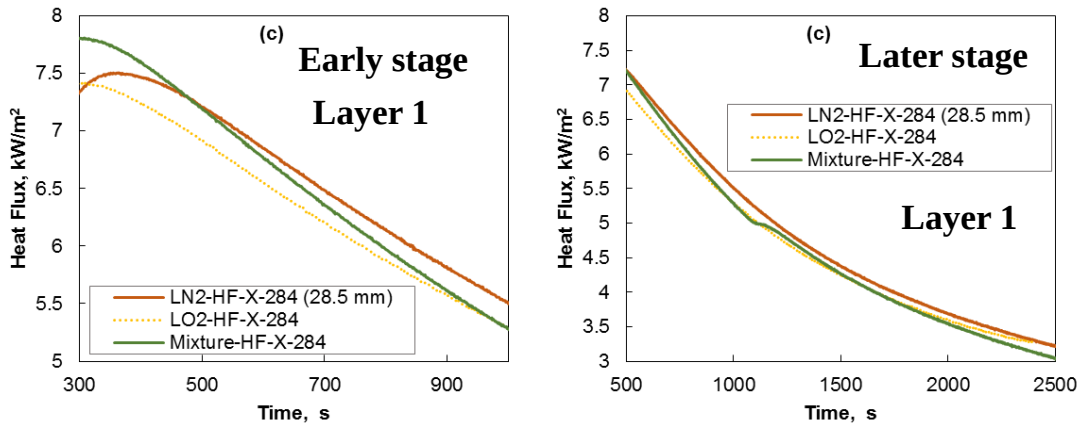

Figure 40: Effect of mixture on the heat flux profiles in layer 1 during the early and the later stage of the spill

4.2.5 Concluding remarks on the medium-scale experiments

The concluding remarks of this study can be described as follows:

- The thermal conductivity of concrete increases linearly over the temperature range of -160°C to 50°C. Within the investigated temperature range, at lower

temperatures the rate of change is higher than the higher temperatures. Between -66°C to -41°C, the rate of change were found negative.

- The specific heat capacity (*Cp*) of concrete increases linearly with the increase of temperature within a range of -160°C to 50°C.
- The surface of the concrete substrate were cooled due to the vapor commence in the beginning of the each experiment. Therefore, the rate of vaporization at the very beginning of the experiment could not be estimated.
- The observations of heat flux sensors plates agree very well with the estimated heat fluxes from mass vaporization. Thus it can be concluded that the major heat transfer mechanism in the vaporization of cryogenic liquids is due to the conductive heat transfer from the concrete substrate.
- In the early stage of the spill, the highest heat flux was observed. At the later stage, the heat flux approached to a steady-state condition. The highest and the steady-state heat fluxes for LN_2 spill over a concrete substrate were recorded as 12.4 kW/m^2 and 3.7 kW/m^2. Similarly, in case of LO_2, the recorded heat fluxes were 12.9 kW/m^2 and 2.96 kW/m^2. For mixture, this could not be estimated due to the lack of knowledge of the mixture concentration at that particular moments since the mixture concentration were continuously changing due to the preferential boiling.
- The boiling phase change from film boiling to nucleate boiling has been observed during the test of LO_2. Whereas, for the LN_2 and mixture experiments,

the phase change evidence was not conclusive. This can be attributed to a short film boiling period for the later and/or effect of surface roughness.

- Preferential boiling of LN_2 over LO_2 was observed during the vaporization of mixture. The heat flux variations due to preferential boiling were varied from 3% to 15%. It was observed that the effect of preferential boiling is more noticeable during the later stage of pool vaporization than the earlier stage.
- The rate of temperature change during mixture vaporization follows the trend of LN_2 at the beginning and the trend of LO_2 at the later stage of the pool vaporization.

4.3 Validation of CFD-based LN_2 film boiling model

The result of medium-scale cryogenic spill experiments discussed in the previous section can be used to validate the CFD based film boiling model of LN_2. However, the experimental data is limited due to the fact no sensors were used to capture concrete surface temperature. The nearest thermocouple close to the surface was at 24 mm deep (TC-111). Figure 41 compares the simulated heat fluxes with the experimental data assuming that the surface temperature is equal to the thermocouple readings of TC-111. It shows an excellent agreement with the simulated heat fluxes. However, it is to be noted that this is a very crude assumption and the true surface temperature will be an asymptotic profile of 1-D heat conduction equation (1). Therefore, the surface

temperature is extrapolated based on the asymptotic solution of 1-D heat conduction equation.

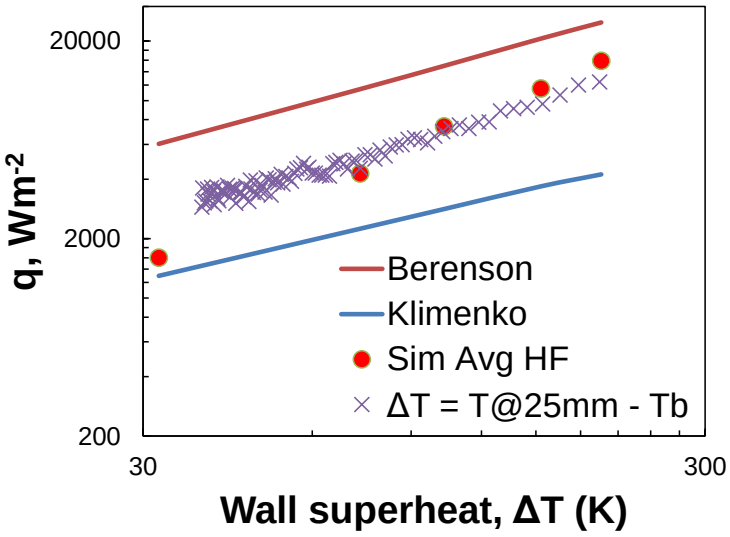

Figure 41: Simulated wall heat flux compared with the thermocouple at 24 mm depth (TC-111)

Figure 42 compares the CFD model predictions of LN_2 film boiling with the estimated wall superheat and experimental heat flux for LN_2 spill tests. The experimental data are also limited because no measures were taken to confirm the boiling regimes. In addition, the surface temperature is assumed to be asymptotic extrapolation of 1-D heat conduction equation estimated based on the heat flux and temperature profiles of layer 1 thermocouples and heat flux sensors. From Figure 42, at a wall superheat of 120K, the

model prediction and experimental observation is in very good agreement. In general, at higher superheat, the CFD model gives better prediction than the lower heat wall superheat. One explanation of this behavior might be the boiling regime change from film to nucleate boiling resulting in a large deviation from the CFD predictions.

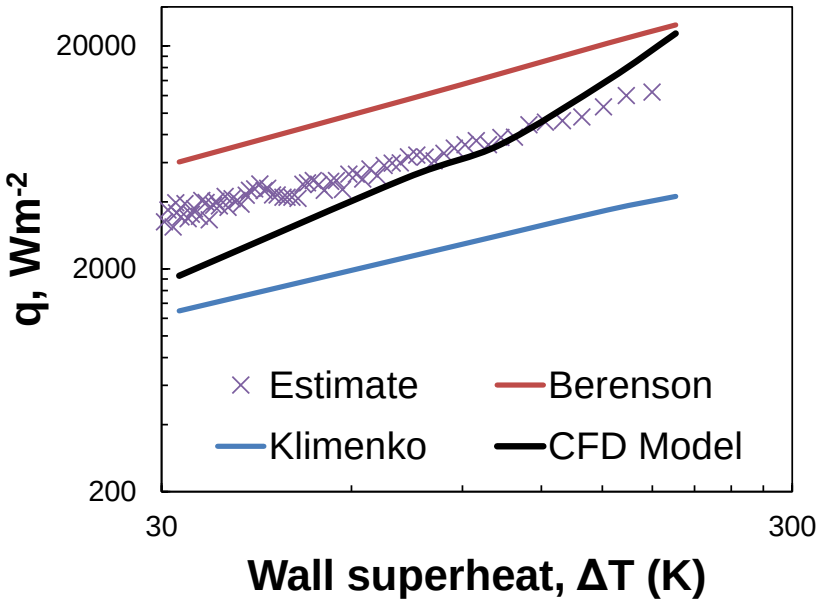

Figure 42: Validation of heat flux using estimated wall superheat for LN_2 film boiling

Figure 43 compares the predictions of CFD-based model, Klimenko correlations and Model 1 with the experimental data of LN_2 spill experiment. Despite the fact that there is not a significant improvement in terms of temperature profiles predictions, the CFD model is the best performer. About 500 seconds, the prediction of CFD model is

quite accurate and then it starts deviating. Information of boiling regime changes would have been a useful resource for more accurate explanation of this phenomenon. Unfortunately, this information is not available due to limitation of the experiment. Nevertheless, boiling regime change to nucleate boiling will increase the heat flux of therefore the CFD estimation is expect get closer to the experimental observation. Another important aspect that might have contributed in the observed deviation at the later stage of spill is the presence of surface roughness. Concrete has large grain size which results in unsmooth surface roughness. Thus the effective distance to the thermocouples might be smaller than the actual measured distance due to porous nature at the surface of concrete. Confirmatory experimental observations are needed to give an accurate account of the observed deviations.

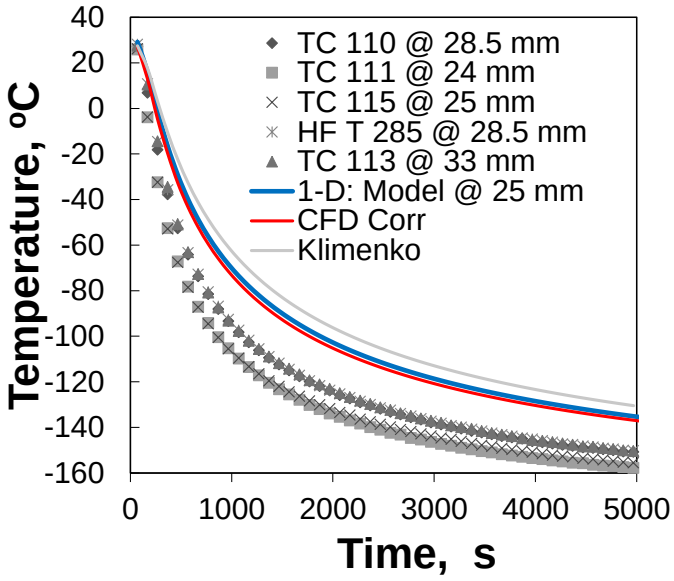

Figure 43: Comparison of temperature profiles predictions

4.4 Validation of CFD-based LNG film boiling model

Unfortunately, during the medium spill experiments, LNG was not available. Therefore literature data is used in this section to validate the LNG film boiling model. Figure 44 depicts the heat flux from the CFD model as well as its comparison with heat transfer correlations, and experimental results from Boe [118], Maplin Sands [116] and Boyle and Kneebone [30]. Boe's laboratory scale experiments reported that for film boiling regime the average boiling heat flux was 44kW/m^2. Maplin Sands experimental result is also used in the Canary software for estimation of vaporization source-term.

From Figure 44, the CFD model can capture all the experimental average heat fluxes (i.e., the black line cuts the constant horizontal lines) however, the correlations failed to do so. Klimenko correlation can capture the Boyle and Kneebone predictions whereas Klimenko correlations failed to capture any.

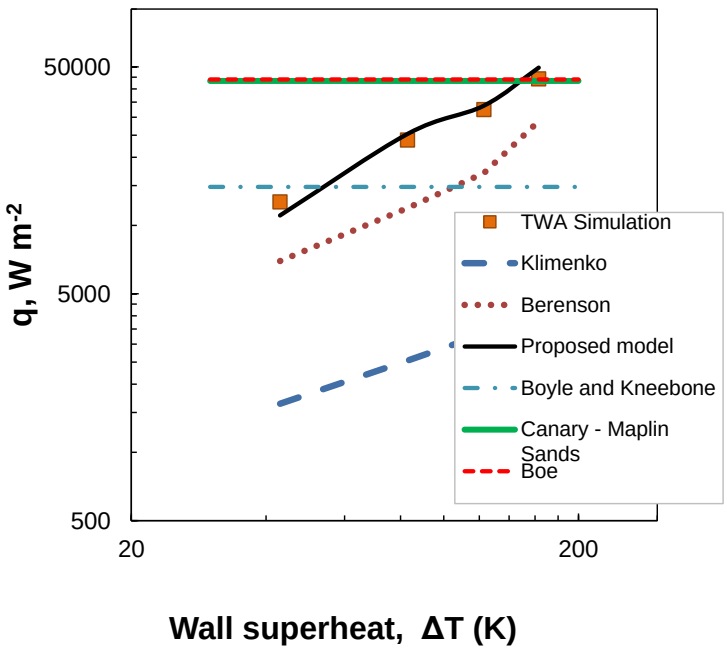

Figure 44: Validation of CFD based LNG film boiling model

4.5 Validation of CFD-based LO_2 film boiling model

Based on the experiments discussed in section 4.2, the surface temperature at the solid-liquid interface is estimated using 1-D heat conduction equation. The estimated wall superheat and corresponding mass vaporization rate of LO_2 is compared against the CFD-based model, Klimenko and Berenson correlations in Figure 45. It is clear that at higher wall superheat, the CFD-based model performs best in predicting the wall heat fluxes. Klimenko correlation significantly under predicts whereas Berenson correlations shows much better prediction.

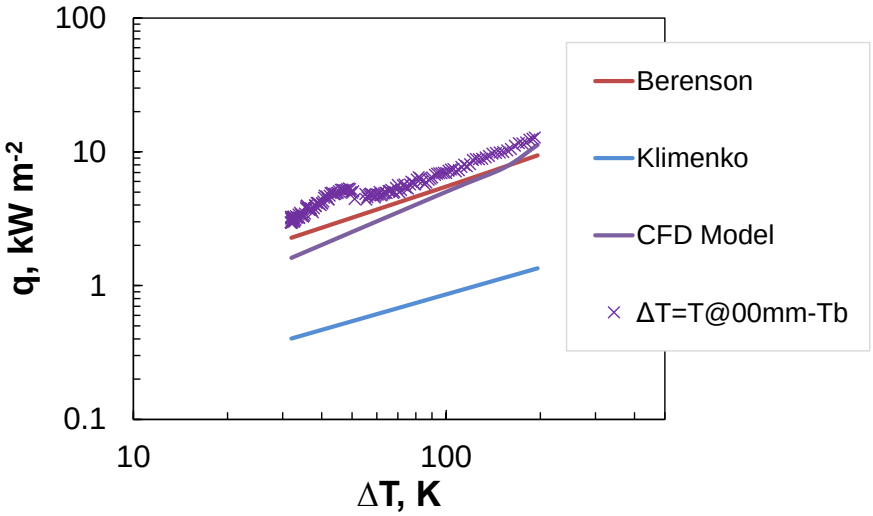

Figure 45: Simulated wall heat flux compared against the estimated wall superheat

4.6 Conclusions

This section presented a medium-scale spill experiment of LN_2, LO_2 and mixture. Two major conclusions of the experiments are (1) the overall vaporization rate of the mixture was not significantly affected for mixing LN_2 with 20% LO_2, (2) Unidirectional heat conduction inside the solid substrate can assumed to model heat transfer from the ground, however the heat transferred resistance imposed due to the phase changes should be modeled properly. The experimental results were used to validate the CFD model of LN_2 and LO_2 film boiling. Despite the fact that the experimental observations were limited, it can be stated that the CFD model gives a better estimation of heat fluxes compared to the existing heat transfer correlations. For the case of LNG, the CFD model

is validated using literature spill experimental data. The CFD model can capture the experimental data of Maplin sands and Laboratory scale experiments.

While validating for LN_2 and LO_2, the CFD-based model fits perfectly when the wall superheat is estimated by using the temperature readings from TC-111 (24mm depth). However when compared with the estimated temperature at the surface, it shows the CFD-based model agrees quite well during the high wall superheat and deviates from the lower wall superheat. This can be accounted to the fact that at lower wall superheat vapor film may break and the boiling regime may transition to the nucleate boiling regime. Moreover, concrete has larger grain size the metals. Hypothesis such as the effective depth of the sensors might not be equal to measured depth in the nucleate boiling regime when the liquid touches the pores of the surface. Despite, it can be concluded that a good agreement was found between the experiments and the simulation.

5. CONCLUSIONS AND FUTURE RESEARCH

This study has addressed cryogenic hazards and issues associated with the consequence severity estimation during the loss of primary containment of cryogenic liquids. Existing consequence estimation models are very sensitive to the input terms *i.e.,* the source-terms. Overestimation of the source-term may not be a conservative approach due to the fact that it will give a smaller pool area and other factors such as time of ignition also determines the consequence for certain scenarios. Therefore an accurate estimation of the vaporization source-term is critical to conduct better risk assessment and consequence analysis.

Existing source-term models are limited due to the fact that the heat transfer resistance from the liquid phase is difficult to estimate. In addition, change in pool boiling regimes also effect the heat transfer rate to the liquid pool. Correlations from literatures are not effective in predicting the heat transfer for LNG vaporization. Thus, this study provides answers to find the key limitations of the existing correlations also overcome those limitations using CFD. The major conclusion are future research needs are discussed below.

5.1 Conclusions

The key conclusions of this study are bulleted as follows:

- A CFD-based approach has been demonstrated to simulate film boiling of cryogenic liquids. Raleigh-Taylor instability has been implemented in CFD environment to

simulate film boiling. Where, the instability is a sinusoidal disturbance function. Taylor dangerous wavelength which causes fastest bubble growth from the vapor film is used to model the distance between two adjacent bubbles (*i.e.*, nodes).

- Existing correlations assume that the bubble formation from the vapor film follow an alternative cycle. In other words, the location of bubble release alternates between the node and anti-node. However, this study finds that the alternating nature is dependent on the depth of the liquid, the characteristics of the flow pattern in the liquid phase and therefore would an oversimplification of the film boiling model. In addition, film boiling simulations presented in section 3 showed that CFD-based film boiling model can overcome this limitation.
- The behavior of the wall heat flux to the liquid pool depends on the behavior of the vapor film thickness. The vaporization source-term can be estimated from the wall heat flux to the liquid pool. It was found the heat flux depends on the wall superheat and also is material specific property.
- A film boiling heat transfer model based on the film boiling CFD simulations and energy balance is proposed. From the CFD based model, it is found that the wall heat fluxes are specific to the material. Thus, heat transfer correlations from the literature which were validated for multiple materials may not be applicable for accurate source-term estimation. Bubble frequency, bubble size, bubble density are also material specific and depends on the degree of wall superheat. CFD-based film model can be employed to get more accurate source-term predictions.

- The CFD-based model is validated using medium-scale experiments for LN_2, LO_2 and mixture. It was found that the mixture effect was not significant for 20% LO_2 and 80% LN_2 spill. Heat conduction inside the solid was found to be unidirectional. The experiments were limited in the context that there were no sensors that can capture the surface temperature. Therefore estimated surface temperature was used to validate the CFD based model for LN_2 and LO_2. It was shown that the experimental results were in good agreement with the CFD based model. LNG film boiling simulations were validated using experiments reported in the literatures. It is shown that the CFD-based model for LNG agrees very well with the experimental data reported in the literature.

5.2 Future research

This research has successfully addressed issues of the vaporization source-term estimations; however, also generated more questions that need to be answered. Research is needed to address these issues. For example,

- Nucleate boiling is an important aspect of the vaporization source-term determination in the later stage of boiling. Therefore, to get the complete picture of the release model, a validated nucleate boiling model which also depends on the surface type needs to be established for concrete substrate. Transition from film boiling to nucleate boiling is another critical factor that requires further study to enable appropriate heat transfer calculation.

- Vaporization source-term estimation during release on the water body is much more complicated due to the fact that advection and conduction heat transfer may occur in this situation. Vapor film between hot water and cold cryogenic liquids will form much more complex shape and would greatly affect the heat transfer from water to cryogens. Despite being a complex problem, film boiling model for the spill on water which considers both advection and conduction heat transfer from water would significantly improve the vaporization source-term estimation.
- Combining this study with the consequence release models will enable better consequence severity estimation. A systematic study of different consequence scenarios (*e.g.,* dispersion, fire, VCE) by varying vaporization source-term would lead a better understanding of catastrophic scenarios and risk level of a plant. Thus, it would help in better land-use planning and rational decision making to distribute resources for private and public safety.

REFERENCES

[1] Federal Energy Regulatory Commission, “Approved North American LNG Import and Export Terminals,” 2016. [Online]. Available: http://www.ferc.gov /industries/gas/indus-act/lng/lng-approved.pdf. [Accessed: 21-Apr-2016].

[2] J. Havens and T. Spicer, “United states regulations for siting LNG terminals: problems and potential,” *J. Hazard. Mater.*, vol. 140, no. 3, pp. 439–443, 2007.

[3] United States Government Accountability Office, “Report GAO-07-316 - Maritime Security: public safety consequences of a terrorist attack on a tanker carrying liquefied natural gas need clarification highlights,” 2007.

[4] NFPA, “NFPA 59A: Standard for the production, storage, and handling of liquefied natural gas (LNG),” National Fire Protection Association, 2013.

[5] Air Products, “Safe handling of cryogenic liquids,” 2014. [Online]. Available: http://www.airproducts.com/~/media/files/pdf/company/safetygram-16.pdf. [Accessed: 13-Mar-2017].

[6] R. E. Bilstein, “Stages to Saturn: A technological history of the Apollo/Saturn launch vehicles (NASA SO-4205),” pp. 89–91, 1996.

[7] R. Radebaugh, “About cryogenics,” in *Macmillan Encyclopedia of Chemistry*, J. J. Laqowski, Ed. New York: Macmillam Reference USA, 2002.

[8] Canadian Center for Occupational Health and Safety, “Cryogenic liquids hazards.” [Online]. Available: https://www.ccohs.ca/oshanswers /chemicals /cryogenic/cryogen1.html. [Accessed: 10-Apr-2016].

[9] CH-IV International, “Safety history of international LNG operations,” *CHIV International Document: TD - 02109,* 2003. [Online]. Available: http://www.ch-iv.com/assets/documents/safety-history.pdf. [Accessed: 13-Mar-2017].

[10] J. L. Woodward and R. M. Pitblado, *LNG Risk Based Safety: Modeling and Consequence Analysis*. NJ, USA; AIChE, John Wiley & Sons, Inc., 2010.

[11] R. Bubbico and E. Salzano, “Acoustic analysis of blast waves produced by rapid phase transition of LNG released on water,” *Saf. Sci.*, vol. 47, no. 4, pp. 515–521, 2009.

[12] International Association of Oil and Gas Producers, “Risk assessment data directory: major accidents,” Report No. 434-17, 2010.

[13] E. Planas-Cuchi, N. Gasulla, A. Ventosa, and J. Casal, “Explosion of a road tanker containing liquified natural gas,” *J. Loss Prev. Process Ind.*, vol. 17, no. 4, pp. 315–321, Jul. 2004.

[14] M. M. Foss, “Introduction to LNG: an overview on liquefied natural gas (LNG), its properties, organization of the LNG industry and safety,” The University of Texas at Austin, 2007. [Online]. Available: http://www.beg.utexas.edu /energyecon /INTRODUCTION TO LNG Update 2012.pdf. [Accessed: 13-Mar-2017].

[15] A. Luketa-Hanlin, “A review of large-scale LNG spills: Experiments and modeling,” *J. Hazard. Mater.*, vol. 132, no. 2–3, pp. 119–140, May 2006.

[16] United States Government Accountability Office, “Maritime Security: public safety consequences of a liquefied natural gas spill need clarification,”

Washington, DC 20548, GAO-07-633T2007, Mar. 2007.

[17] D. M. Webber, “A model for pool spreading and vaporization and its implementation in computer code GASP,” Safety and Reliability Directorate, UK Atomic Energy Authority SRD/HSE/R 507, 1990.

[18] L. Véchot, T. Olewski, C. Osorio, O. Basha, Y. Liu, and M. S. Mannan, “Laboratory scale analysis of the influence of different heat transfer mechanisms on liquid nitrogen vaporization rate,” *J. Loss Prev. Process Ind.*, vol. 26, no. 3, pp. 398–409, May 2013.

[19] G. Opschoor, “Methods for the calculation of the physical effects of the escape of dangerous material (liquids and gases) Part II,” in *TNO Yellow Book*, Voorburg: Directorate-General of Labour, Ministry of Social Affairs, Netherlands, 1979, pp. 3–61.

[20] M. Ahammad, T. Olewski, L. N. Véchot, and S. Mannan, “A CFD based model to predict film boiling heat transfer of cryogenic liquids,” *J. Loss Prev. Process Ind.*, vol. 44, pp. 247–254, 2016.

[21] R. C. Reid and R. Wang, “The boiling rates of LNG on typical dike floor materials,” *Cryogenics.*, vol. 18, no. 7, pp. 401–404, 1978.

[22] G. Opschoor, “Investigations into spreading and evaporation of LNG spilled on water,” *Cryogenics.*, vol. 17, no. 11, pp. 629–633, 1977.

[23] F. Briscoe and P. Shaw, “Spread and evaporation of liquid,” *Prog. Energy Combust. Sci.*, vol. 6, no. 2, pp. 127–140, Jan. 1980.

[24] D. Burgess and M. G. Zabetakis, “Fire and explosion hazards associated with

liquefied natural gas," U.S. Dept. of Interior, Bureau of Mines, Report of Investigation 6099, 1962.

[25] American Gas Association, "LNG safety program: Interim report on phase II work," American Gas Association, Columbus, Ohio, USA, Project IS-3-1, Jul. 1974.

[26] E. M. Drake and R. C. Reid, "How LNG boils on soils," *Hydrocarb. Process,* vol. 54, no. 5, 1975.

[27] D. M. Webber, S. E. Gant, M. J. Ivings, and S. F. Jagger, "LNG source term models for hazard analysis: A review of the state-of-the-art and an approach to model assessment," Buxton, Derbyshire, UK, Research Report: RR789, 2010.

[28] P. K. Raj and A. Kalelkar, "Assessment models in support of the Hazard Assessment Handbook," U.S. Coast Guard Report No. CG-446-3, 1974.

[29] P. K. Raj, "Models for cryogenic liquid spill behavior on land and water," *J. Hazard. Mater.*, vol. 5, no. 1–2, pp. 111–130, Oct. 1981.

[30] G. J. Boyle and A. Kneebone, "Laboratory investigations into the characteristics of LNG spills on water: Evaporation, Spreading and Vapour Dispersion," Chester, England, Shell Research Limited Report 6Z 32, 1973.

[31] S. Atallah, M. Sirdesai, and D. M. Jennings, "Source1: A model for creating a DEGADIS input file," Gas Research Institute Report GRI-92/0543, 1993.

[32] D. M. Webber and S. J. Jones, "A model for spreading, vaporizing pools derived from shallow-layer equations," in *International Conference on Vapor Cloud Modelling*, Boston, Massachussetts, 1987.

[33] D. M. Webber, “Model for pool spreading and vaporization and its implementation in computer code GASP,” SRD/HSE/R 507, 1990.

[34] D. M. Webber, “Evaporation and boiling of liquid pools - A unified treatment,” *Math. Major Risk Assesment*, pp. 131–44, 1989.

[35] V. V. Klimenko, “Film boiling on a horizontal plate - new correlation,” *Int. J. Heat Mass Transf.*, vol. 24, no. 1, pp. 69–79, Jan. 1981.

[36] S. R. Saraf and G. A. Melhem, “Modelling LNG pool spreading and vaporisation,” in *AICHE Spring Meeting*, 2005.

[37] J. L. Woodward, “Coupling dynamic blow down and pool evaporation model for LNG,” *J. Hazard. Mater.*, vol. 140, no. 3, pp. 478–487, 2007.

[38] R. Pitblado, J. Baik, and V. Raghunathan, “LNG decision making approaches compared.,” *J. Hazard. Mater.*, vol. 130, no. 1–2, pp. 148–54, Mar. 2006.

[39] D. W. Taylor, “The role of consequence modeling in LNG facility siting,” *J. Hazard. Mater.*, vol. 142, no. 3, pp. 776–785, 2007.

[40] H. W. M. Witlox, *PHAST Technical Reeference: PVAP Theory, Version 6.7*. Det Norske Veritas, 2006.

[41] J. A. Fay, “Physical processes in the spread of oil on a watersurface.,” in *Proceedings of the joint conference on prevention and controlof oil spills*, 1971, pp. 463–467.

[42] J. A. Fay, *The spread of oil slick on calm sea*. Cambridge, MA: Plenum Press, 1969.

[43] J. Fay, “Risks of LNG and LPG,” *Annu. Rev. Energy*, pp. 89–105, 1980.

[44] H. R. Chang and R. C. Reid, “Spreading-Boiling model for instantaneous spills of liquefied petroleum gas (LPG) on water,” *J. Hazard. Mater.*, vol. 7, pp. 19–35, 1982.

[45] J. A. Fay, “Spills and fires from LNG and oil tankers in Boston harbor,” 2003. [Online]. Available: http://quoddyloop.com/savepassamaquoddybay/documents/safety_reports/Fay_LNG_Fire_Impact.pdf. [Accessed: 13-Mar-2017].

[46] J. A. Fay, “Spread of large LNG pools on the sea,” *J. Hazard. Mater.*, vol. 140, no. 3, pp. 541–551, Feb. 2007.

[47] M. Hightower, L. Gritzo, A. Luketa-Hanlin, J. Covan, S. Tieszen, G. Wellman, M. Irwin, M. Kaneshige, B. Melof, C. Morrow, and D. Ragland, “Guidance on risk analysis and safety implications of a large liquified natural gas (LNG) spill over water,” Albuquerque, New Mexico, Sandia National Laboratories Report SAND2004-6258, 2004.

[48] ABS Consulting, “Consequence assessment methods for incidents involving releases from liquefied natural gas carriers,” Report GEMS 1288209, 2004.

[49] M. Marks, “Liquefied natural gas in California: History, risks, and siting,” California Energy Commission 700-03-005, 2003.

[50] D. C. Thoman, K. R. O’Kula, J. C. Laul, M. W. Davis, and K. D. Knecht, “Comparison of ALOHA and EPIcode for safety analysis applications,” *J. Chem. Heal. Saf.*, vol. 13, no. 6, pp. 20–33, 2006.

[51] T. A. Cavanaugh, J. H. Siegell, and K. W. Steinberg, “Simulation of vapor emissions from liquid spills,” *J. Hazard. Mater.*, vol. 38, no. 1, pp. 41–63, Jul.

1994.

[52] FERC, “Notice of availability of detailed computations for the consequence assessment methods for incidents involving releases from liquefied natural gas carriers,” U.S. Federal Energy Regulatory Commission Docket AD04-6-000, 2004.

[53] D. W. Johnson and J. B. Cornwell, “Modeling the release, spreading, and burning of LNG, LPG, and gasoline on water,” *J. Hazard. Mater.*, vol. 140, no. 3, pp. 535–540, Feb. 2007.

[54] Y. H. Qiao, H. H. West, M. S. Mannan, D. W. Johnson, and J. B. Cornwell, “Assessment of the effects of release variables on the consequences of LNG spillage onto water using FERC models,” *J. Hazard. Mater.*, vol. 130, no. 1–2, SI, pp. 155–162, Mar. 2006.

[55] J. C. Swans and M. Spaulding, “A new approach to simulation of LNG spills in the ocean,” *Ocean. 2006 IEEE*, 2006.

[56] O. R. Hansen, F. Gavelli, M. Ichard, and S. G. Davis, “Validation of FLACS against experimental data sets from the model evaluation database for LNG vapor dispersion,” *J. Loss Prev. Process Ind.*, vol. 23, no. 6, pp. 857–877, Nov. 2010.

[57] S. Brambilla and D. Manca, “Accidents involving liquids: A step ahead in modeling pool spreading, evaporation and burning,” *J. Hazard. Mater.*, vol. 161, no. 2–3, pp. 1265–1280, Jan. 2009.

[58] P. Drivas, “Calculation of evaporative emissions from multicomponent liquid spills.,” *Environ. Sci. Technol.*, vol. 10, no. 16, p. 726–728., 1982.

[59] P. Leonelli, C. Stramigioli, and G. Spadoni, “The modelling of pool vaporization,” *J. Loss Prev. Process Ind.*, vol. 7, no. 6, pp. 443–450, Nov. 1994.

[60] D. P. French and T. Isaji, “Evaluation of the consequences of chemical spills using modelling: chemicals used in deepwater oil and gas operations.,” *Environ. Model. Softw.*, vol. 19, pp. 629–644, 2004.

[61] N. Zuber, “Hydrodynamic aspects of boiling heat transfer,” University of California, Los Angeles, 1959.

[62] P. J. Berenson, “Film-boiling heat transfer from a horizontal surface,” *J. Heat Transfer*, pp. 351–356, 1961.

[63] V. Sernas, J. H. Lienhard, and V. K. Dhir, “The Taylor wave configuration during boiling from a flat plate,” *Int. J. Heat Mass Transf.*, vol. 16, pp. 1820–1821, 1973.

[64] E. R. Holster and J. W. Westwater, “Film boiling on a horizontal plate,” *Am. Rocket Soc. J.*, pp. 553–558, 1962.

[65] V. V. Klimenko and A. G. Shelepen, “Film boiling on horizontal plate - a supplementary communication,” *Int. J. Heat Mass Transf.*, vol. 25, no. 10, pp. 1611–1613, 1982.

[66] G. Son and V. K. Dhir, “Numerical simulation of saturated film boiling on a horizontal surface,” *J. Heat Transfer*, vol. 119, no. August 1997, pp. 525–533, 1997.

[67] Y. P. Chang, “A theoretical analysis of heat transfer in natural convection and in boiling.,” *ASME Trans.*, vol. 79, pp. 1501–1513, 1957.

[68] R. Bellman and R. H. Pennington, “Effects of surface tensions and viscosity on

Taylor instability," *Q. Appl. Math.*, vol. 12, pp. 151–162, 1954.

[69] V. P. Carey, *Liquid-Vapor phase change phenomena: An introduction to the thermophysics of vaporization and condensation process in heat transfer equipment*. Washington ,D.C.: Hemisphere Publishing Corp, 1992.

[70] A. Faghri and Y. Zhang, *Transport phenomena in multiphase systems*. London: Academic Press, Elsevier Inc, 2006.

[71] V. K. Dhir, "Numerical simulations of pool-boiling heat transfer," *AIChE J.*, vol. 47, no. 4, pp. 813–834, Apr. 2001.

[72] G. Son and V. K. Dhir, "Numerical simulation of film boiling near critical pressures with a level set method," *J. Heat Transfer*, vol. 120, no. February, pp. 183–192, 1998.

[73] C. H. Panzarella, S. H. Davis, and S. G. Bankoff, "Nonlinear dynamics in horizontal film boiling," *J. Fluid Mech.*, vol. 402, pp. 163–194, 2000.

[74] D. Banerjee and V. K. Dhir, "Study of subcooled film boiling on a horizontal disc: Part I—Analysis," *J. Heat Transfer*, vol. 123, no. 2, pp. 271–284, 2001.

[75] D. Juric and G. Tryggvason, "Computations of boiling flows," *Int. J. Multiph. Flow*, vol. 24, no. 3, pp. 387–410, 1998.

[76] A. Esmaeeli and G. Tryggvason, "Computations of film boiling. Part I: numerical method," *Int. J. Heat Mass Transf.*, vol. 47, no. 25, pp. 5451–5461, Dec. 2004.

[77] A. Esmaeeli and G. Tryggvason, "Computations of film boiling. Part II: multi-mode film boiling," *Int. J. Heat Mass Transf.*, vol. 47, no. 25, pp. 5463–5476, Dec. 2004.

[78] S. W. J. Welch and J. Wilson, “A Volume of Fluid based method for fluid flows with phase change,” *J. Comput. Phys.*, vol. 160, no. 2, pp. 662–682, May 2000.

[79] D. L. Youngs, “Time dependent multi-material flow with large fluid distortion,” in *Numerical Methods in Fluid Dynamics*, K. W. Morton and M. J. Baines, Eds. Academic Press, 1982, pp. 273–285.

[80] S. W. J. Welch and T. Rachidi, “Numerical computation of film boiling including conjugate heat transfer,” *Numer. Heat Transf. Part B*, vol. 42, pp. 35–53, 2002.

[81] M. H. Yuan, Y. H. Yang, T. S. Li, and Z. H. Hu, “Numerical simulation of film boiling on a sphere with a volume of fluid interface tracking method,” *Int. J. Heat Mass Transf.*, vol. 51, no. 7–8, pp. 1646–1657, Apr. 2008.

[82] D. K. Agarwal, S. W. J. Welch, G. Biswas, and F. Durst, “Planar simulation of bubble growth in film boiling in near-critical water using a variant of the VOF method,” *J. Heat Transfer*, vol. 126, no. 3, p. 329, 2004.

[83] G. Tomar, G. Biswas, A. Sharma, and A. Agrawal, “Numerical simulation of bubble growth in film boiling using a coupled level-set and volume-of-fluid method,” *Phys. Fluids*, vol. 17, no. 112103, 2005.

[84] G. Tomar, G. Biswas, A. Sharma, and S. W. J. Welch, “Multimode analysis of bubble growth in saturated film boiling,” *Phys. Fluids*, vol. 20, no. 92101, pp. 1–8, 2008.

[85] A. Hens, G. Biswas, and S. De, “Analysis of interfacial instability and multimode bubble formation in saturated boiling using coupled level set and volume-of-fluid approach,” *Phys. Fluids*, vol. 26, no. 12105, 2014.

[86] S. W. J. Welch and G. Biswas, “Direct simulation of film boiling including electrohydrodynamic forces,” *Phys. Fluids*, vol. 19, no. 1, p. 12106, 2007.

[87] G. Tomar, D. Gerlach, G. Biswas, N. Alleborn, A. Sharma, F. Durst, S. W. J. Welch, and A. Delgado, “Two-phase electrohydrodynamic simulations using a volume-of-fluid approach,” *J. Comput. Phys.*, vol. 227, pp. 1267–1285, 2007.

[88] Y. Liu, T. Olewski, and L. N. Véchot, “Modeling of a cryogenic liquid pool boiling by CFD simulation,” *J. Loss Prev. Process Ind.*, vol. 35, pp. 125–134, May 2015.

[89] C. W. Hirt and B. D. Nichols, “Volume of fluid (VOF) method for the dynamics of free boundaries,” *J. Comput. Phys.*, vol. 39, no. 1, pp. 201–225, Jan. 1981.

[90] S. Hardt and F. Wondra, “Evaporation model for interfacial flows based on a continuum-field representation of the source terms,” *J. Comput. Phys.*, vol. 227, no. 11, pp. 5871–5895, May 2008.

[91] C. Kunkelmann and P. Stephan, “CFD simulation of boiling flows using the Volume-of-Fluid method within OpenFOAM,” *Numer. Heat Transf. Part A Appl.*, vol. 56, no. 8, pp. 631–646, Nov. 2009.

[92] T. Kunugi, “Brief review of latest direct numerical simulation on pool and film Boiling,” *Nucl. Eng. Technol.*, vol. 44, no. 8, pp. 847–854, Dec. 2012.

[93] Ansys Inc., “ANSYS Fluent theory guide,” p. 591, 2013.

[94] B. D. Nichols, C. W. Hirt, and R. . Hotchkiss, “SOLA-VOF: A solution algorithm of transient flow flow with multiple free boundaries,” Los Alamos Scientific Lab, NM(USA), Los Alamos Scientific Lab LA 8355, 1980.

[95] M. Rudman, “Volume-tracking methods for interfacial flow calculations,” *Int. J. Numer. Methods Fluids*, vol. 24, no. January 1996, pp. 671–691, 1997.

[96] O. Ubbink and R. I. Issa, “A method for capturing sharp fluid interfaces on arbitrary meshes,” *J. Colloid Sci.*, vol. 50, pp. 26–50, 1999.

[97] W. F. Noh and P. Woodward, “SLIC (Simple line interface calculation),” in *The fifth internatioal conference on Numerical Methods in Fluid Dynamics, Enschede*, 1976.

[98] J. U. Brackbill, D. B. Kothe, and C. Zemach, “A continuum method for modeling surface tension,” *J. Comput. Phys.*, vol. 100, pp. 335–354, 1992.

[99] Ansys Inc., “Horizontal film boiling (tutorial),” pp. 1–20, 2011.

[100] F. Gibou, L. Chen, D. Nguyen, and S. Banerjee, “A level set based sharp interface method for the multiphase incompressible Navier--Stokes equations with phase change,” *J. Comput. Phys.*, vol. 222, no. 2, pp. 536–555, 2007.

[101] R. L. Rowley, W. V. Wilding, J. L. Oscarson, J. L. Zundel, N. A. Marshall, T. L. Daubert, and R. P. Danner, *DIPPR Data Compilation of Pure Compund Properties*. Design Institute for Physical Property Data/AIChE, 2003.

[102] R. F. Barron, *Cryogenic Heat Transfer*. Philadelphia, PA, USA; London, UK: Taylor & Francis, 1999.

[103] P. J. Berenson, “Experiments on pool-boiling heat transfer,” *Int. J. Heat Mass Transf.*, vol. 5, no. 10, pp. 985–999, 1962.

[104] T. A. Cavanaugh, J. H. Siegell, and K. W. Steinberg, “Simulation of Vapor Emissions From Liquid Spills,” *J. Hazard. Mater.*, vol. 38, no. 1, pp. 41–63, Jul.

1994.

[105] D. M. Webber and M. J. Ivings, “Modelling bund overtopping using Shallow Water Theory,” *J. Loss Prev. Process Ind.*, vol. 23, no. 5, pp. 662–667, Sep. 2010.

[106] N. Gopalaswami, T. Olewski, L. N. Véchot, and M. S. Mannan, “Small-scale experimental study of vaporization flux of liquid nitrogen released on water,” *J. Hazard. Mater.*, vol. 297, pp. 8–16, 2015.

[107] N. Gopalaswami, L. Vechot, T. Olewski, and M. S. Mannan, “Small-scale experimental study of vaporization flux of liquid nitrogen released on ice,” *J. Loss Prev. Process Ind.*, vol. 37, pp. 124–131, 2015.

[108] A. J. Prince, “Details and results of spill experiments of cryogenic liquids onto land and water,” 1983.

[109] A. M. Thyer, “A review of data on spreading and vaporisation of cryogenic liquid spills,” *J. Hazard. Mater.*, vol. 99, no. 1, pp. 31–40, Apr. 2003.

[110] C. Conrado and V. Vesovic, “The influence of chemical composition on vaporisation of LNG and LPG on unconfined water surfaces,” *Chem. Eng. Sci.*, vol. 55, no. 20, pp. 4549–4562, Oct. 2000.

[111] A. Luketa-Hanlin, “A review of large-scale LNG spills: experiments and modeling,” *J. Hazard. Mater.*, vol. 132, no. 2–3, pp. 119–140, May 2006.

[112] R. Boe, “Pool boiling of hydrocarbon mixtures on water,” *Int. J. Heat Mass Transf.*, vol. 41, pp. 1003–1011, 1998.

[113] E. M. Drake, A. A. Jeje, and R. C. Reid, “Transient boiling of liquefied cryogens on a water surface: I. Nitrogen, Methane and Ethane,” *Int. J. Heat Mass Transf.*,

vol. 18, no. 12, pp. 1361–1368, Dec. 1975.

[114] D. S. Burgess, J. Biordi, and J. Murphy, “Hazards associated with the spillage of LNG on water,” Pittsburgh, PA, Bureau of Mines Report 7448, 1970.

[115] W. May, W. McQueen, and R. H. Whipp, “Spills of LNG on water,” in *Operating Section proceedings*, 1973, p. D-141-D-150.

[116] J. Puttock, D. Blackmore, and G. Colenbrander, “Field experiments on dense gas dispersion,” *J. Hazard. Mater.*, vol. 6, pp. 13–41, 1982.

[117] R. Koopman and R. Cederwall, “Analysis of Burro series 40-m3 LNG spill experiments,” *J. Hazard. Mater.*, vol. 6, 1982.

[118] R. Boe, “Pool boiling of hydrocarbon mixtures on water,” Norwegian University of Science and Technology, 1996.